九州大学学術情報リポジトリ
Kyushu University Institutional Repository

Metal-organic frameworks as a platform for controlling triplet exciton dynamics

三重野, 寛之

https://doi.org/10.15017/1931877

出版情報：九州大学, 2017, 博士（工学）, 課程博士
バージョン：
権利関係：

2017

Doctor thesis

Metal-organic frameworks as a platform for controlling triplet exciton dynamics

Hiroyuki Mieno

Department of Chemistry and Biochemistry

Graduate School of Engineering

Kyushu University

Chapter 1

Introduction

1-1. Luminescence in organic materials

Luminescence in organic materials is a radiative process in which an excited state relaxes to the ground state. Luminescent organic materials used in fluorescent imaging probes,[1,2] optical switches,[3,4] organic light-emitting diodes (OLEDs),[5–8] and other applications[9–12] have been extensively developed by taking full advantage of the unlimited chemical design with the robust bonding capabilities of carbon.

Luminescence from organic molecules is classified as either fluorescence or phosphorescence based on the spin states of the radiative transition (Fig. 1-1). Fluorescence is defined as a spin-allowed radiative transition from the lowest singlet excited state (S_1) to the singlet ground state (S_0), and phosphorescence is defined as a spin-forbidden transition from the lowest triplet excited state (T_1) to S_0. A transition from S_1 to T_1—called intersystem crossing (ISC)—is spin forbidden, but it can be partially allowed by spin-orbit coupling. Reverse ISC (RISC), a transition from T_1 to S_1, can also occur in some cases, leading to delayed fluorescence. Delayed fluorescence via RISC is called thermally activated delayed fluorescence (TADF) because the population of singlets produced from triplets that undergo RISC increases with temperature. Singlets produced from the collision of triplets, a process well known as triplet-triplet annihilation (TTA), can also lead to delayed fluorescence.

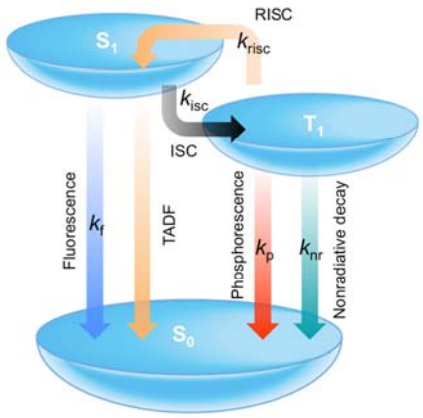

Figure 1-1. Jablonski diagram of organic molecules.

In OLEDs, recombination of injected electrons and holes generates excitons in a ratio of 25% singlets to 75% triplets based on the laws of spin statistics. Thus, the development of luminescent materials that can harvest triplets is important. However, if a large number of triplet excitons accumulates, which is prone to happen because of the generally long lifetimes of triplets, external quantum efficiency (η_{EQE}) tends to decrease because of TTA and singlet-triplet annihilation at high current densities. Therefore, it is necessary to develop luminescent materials that can efficiently and rapidly convert triplet excitons into emission to achieve a high photoluminescence quantum yield (Φ_{PL}) and short triplet lifetime.

Phosphorescent materials, which are able to utilize triplet excitons for emission, have been the focus of intense development since 2000, when Adachi et al. demonstrated an η_{EQE} of nearly 20% in the OLED using the phosphorescent emitter $Ir(ppy)_3$.[13] Although phosphorescent materials can achieve Φ_{PL} of nearly 100% with relatively short triplet lifetimes, they require the inclusion of a rare metal in the chemical structure to obtain a high rate constant of radiative decay from T_1 to S_0 (k_p). Anthracene derivatives can be used as emitters to harvest triplets via TTA for emission without the need for rare metals, but the theoretical maximum internal quantum efficiency (η_{IQE}) based on such a strategy is limited to 62.5%. In 2009, the potential to use TADF, which up-converts T_1 to S_1 through RISC, in an OLED under electrical excitation was first demonstrated, but these initial devices had a low efficiency.[14] Uoyama et al. then reported a series of highly efficient TADF emitters that are based on carbazolyl dicyanobenzene and exhibit Φ_{PL} of over 90%, allowing high η_{EQE} of 20% comparable to phosphorescence OLEDs.[15] Thus, TADF materials eliminate the need for rare metals while also achieving η_{IQE} of nearly 100% and short triplet lifetimes.

These triplet-harvesting emitters have also been adapted for use in other applications,

such as sensors,[16] optical storage,[4,12] photocatalysts, photon up-conversion,[17] bio-imaging,[18,19] and reverse saturable absorption.[20] In these applications, a long triplet lifetime is often more desirable than a short one. In the case of bio-applications, long-lived triplet excitons are useful because the emission by phosphorescence can be temporally separated from the excitation of the emitters by light, leading to lower-cost detectors such as charge-coupled devices (CCDs).[18] To obtain reverse saturable absorption upon exposure to weak continuous incoherent light, the accumulation of a population of singlet or triplet excitons is important, so the long lifetimes of triplet excitons make triplets the superior candidate.[20] In photon up-conversion, the probability of triplet-triplet fusion increases with the collision frequency of triplet excitons.[17] Therefore, approaches to control triplet dynamics in molecules are important for these and new applications.

The dynamics of triplet excitons are primarily determined by processes falling into four main categories: (1) ISC and (2) RISC between singlet and triplet states, (3) radiative decay from T_1 to S_0, and (4) nonradiative decay, which can be further divided into each processes such as thermal deactivation, concentration quenching, and energy transfer to other molecules. To rapidly harvest triplets for emission with a short lifetime, either the radiative decay of triplets (3) or the RISC of singlets to triplets (2) must be accelerated. The former is most commonly achieved through inclusion of heavy atoms in the chemical structure of an emitter or the environment surrounding the emitters, because heavy atoms can accelerate both the rate constant of ISC from singlets to triplets (k_{isc}) and of radiative decay from T_1 to S_0 (k_p) (1 and 3). On the other hand, minimization of the energy gap between S_1 and T_1 is essential to accelerate RISC (2) and attain emission through thermally activated delayed fluorescence, which has a shorter lifetime than phosphorescence from metal-free aromatic compounds.

If long-lived room-temperature phosphorescence is desired, nonradiative decay processes must be minimized because they generally far outpace the radiative decay of triplets. Two methods to reduce nonradiative decay and increase Φ_{PL}, without increasing k_p, are the introduction of emitters into rigid host matrices such as steroids[21,22] and polymers[23,24] and the encapsulation of emitters in clathrate compounds like cyclodextrin[25,26] and cucurbituril.[27] Although these host matrices can be easily fabricated without necessitating the synthesis of new emitters, they have some serious problems. For example, the use of cyclodextrin or cucurbituril limits the available guest emitters to those that are small enough to fit in the encapsulating molecule, and steroids and polymers are thermally instable because of phase transitions and thermal decomposition. Therefore, I have considered metal-organic frameworks (MOFs) as an alternative option for suppressing nonradiative decay processes while solving some of the previously mentioned problems.

1-2. Metal-organic frameworks (MOFs)

Metal-organic frameworks (also referred as porous coordination polymers (PCPs)) were first explored in the late 1990s as a new class of porous materials by O. M. Yaghi et al. and S. Kitagawa et al. almost at the same time.[28,29] MOFs are composed of a network of metal clusters and organic linkers held together by coordination bonds formed at ambient conditions between the metal cations and the functional groups of the linkers. The structural properties of MOFs, including the size and shape of the pores and windows, can be controlled based on the choice of components (Fig. 1-2).[30–34] Furthermore, the photophysical and electronic properties of MOFs can be tuned by functionalizing the organic linkers or changing the selection of metal ions.[35–38]

MOFs with a high selectivity and extremely large surface area have commercial applications such as in gas separationand storage.[39–41] Such MOFs have been developed by designing organic linkers and secondary building units (SBUs),[36] tuning synthetic conditions, and modifying their surfaces. During the past decade, a wide variety of MOFs have been synthesized and studied with the aim of opening new applications, such as in chemical sensors,[42] photovoltaic cells,[43,44] thermoelectric devices,[45] hydrogen storage,[41] and catalysis.[46]

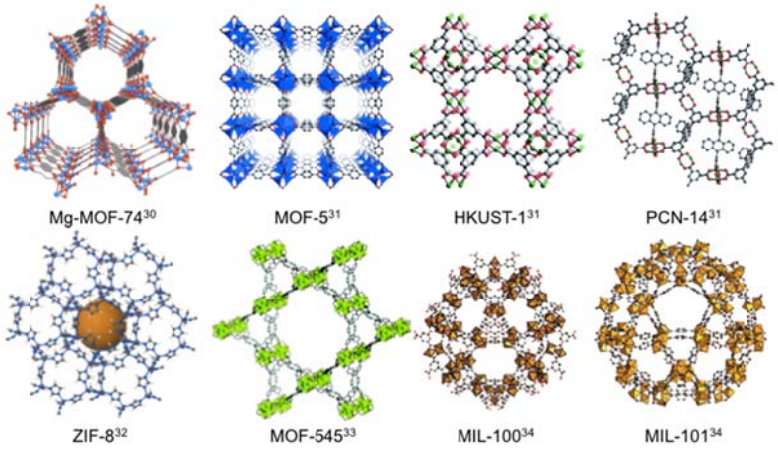

Figure 1-2. Examples of metal-organic frameworks (MOFs) using different metal cations and organic linkers.

1-3. Synthesis of MOFs

A wide variety of synthetic methods are possible because MOFs can be constructed by coordination bonds between metal ions or clusters and carboxylate, phosphonate,[47] and amino groups. Although MOFs can be synthesized through self-assembly at ambient condition without heating, single crystals and high crystalline samples are commonly formed using solvothermal reactions, which are defined as reactions taking place in closed vessels above the boiling point of the reaction solvents.[48] Using the SBUs which were reported by O. M. Yaghi et al. systematized in 2008,[49] a vast number of MOFs have been synthesized. Several other synthetic methods, such as microwave,[50] electrochemical,[51] and mechanochemical syntheses[52] have been demonstrated with the aim of developing solvent-free, low-cost, environmentally friendly, and time-saving procedures. Developing ways to fabricate MOF thin films is also for application of MOFs to electronic devices such as photovoltaic cells[43,44]and thermoelectric devices. In 2007, a step-by-step fabrication method for MOF thin films, which is called the layer-by-layer method, was developed by C. Wöll et al.[53] The MOFs are grown by soaking a substrate functionalized with amine- or carboxyl-terminated self-assembled monolayers in alternating solutions of metal or organic ligand. Using this method, highly oriented MOF films and a tunable thickness can be obtained by altering the temperature or the number of immersion cycles.

Once MOFs are synthesized, an activation step of MOFs, which eliminates the residual organic linkers and reaction solvents within the pores of MOFs, must be performed. The residual organic compounds often cause undesired influence on their photophysical properties. Therefore, the activation step generally consists of the following steps: (1) washing with organic solvents such as dimethylformamide (DMF) several times, (2) soaking

in organic solvents for one day to exchange DMF with other organic solvents, which is easily evaporated, (3) repeating these steps for at least three times, and (4) heating above 100 ˚C under vacuum.

1-4. Luminescent MOFs

Luminescent MOFs have been reported as potential materials for various applications such as chemical sensors,[54–57] scintillators,[58] bioimaging,[59–61] photocatalysts,[62] and electronics.[63] Of the 30,000 MOF-related publications to date, one-tenth (almost 4,000) focus on the luminescent properties of MOF, according to the ISI Web of Science (retrieved September 2017). The origins of luminescence in MOFs are diverse because MOFs are composed of metal ions and organic linkers, allowing for interactions between organic linkers and metal clusters. MOFs can also have cavities that can encapsulate guest molecules. Thus, emission from luminescent MOFs can be classified into three groups: (1) metal-based emission, (2) ligand-based emission, and (3) guest-related emission (Fig. 1-3).

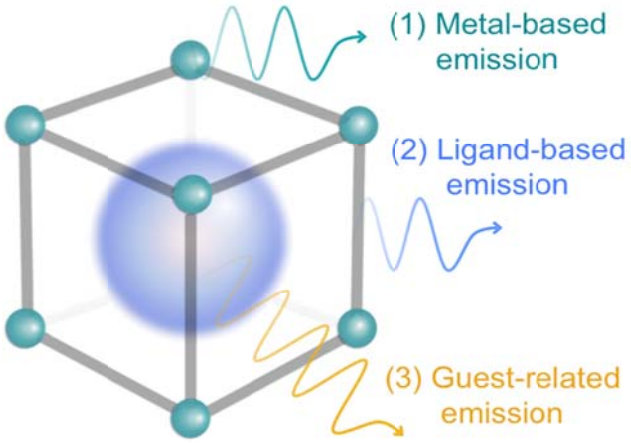

Figure 1-3. The origins of luminescence in MOFs

1-4-1. Metal-based emission

There are many MOFs that have metal-based emission originating from luminescence of lanthanide ions.[64,65] In such MOFs, organic linkers absorb the excitation light and transfer their energy to the lanthanide ions. The emission spectra and lifetime of these MOFs are determined by the properties of the metal. Therefore, the MOFs having metal-based emission often exhibit narrow emission spectra and long luminescence lifetimes, making them promising for sensing applications.[65] After Reineke et al. firstly reported a MOF based on terbium ions in 1999,[66] lanthanide-based MOFs have been well developed with a focus on potential applications such as luminescence and chemical sensing.

1-4-2. Ligand-based emission

Ligand-based emission includes metal-to-ligand and ligand-to-metal charge transfer (MLCT and LMCT, respectively) and luminescence directly from the organic ligands themselves, such as anthracene[67] and pyrene derivatives.[68] The design and synthesis of organic molecules with specific functional groups for linking, such as carboxyl or amine, are needed to construct new MOFs with ligand-based luminescence. This restriction of chemical functionality makes it difficult to develop their photophysical properties and applications. There are also many reports describing aggregation,[69] excimer formation,[70] or self-quenching of organic ligands,[70] which lead to low Φ_{PL}, shifted emission colors, and decreased exciton lifetimes. In 2014, H.-C. Zhou et al. reported **PCN-94** (a Zr-based MOF), which uses the fluorescent linker 4′,4‴,4⁗ ″,4⁗ ‴ ⁗ ″-(ethene-1,1,2,2-tetrayl)tetrakis(([1,1′-biphenyl]-3-carboxylic acid)) (**H_4ETTC**). The aromatic core tetraphenylethylene in **H_4ETTC** is well-known for its aggregation-induced emission (AIE) characteristics.[71] Because the formation of MOFs

rigidifies AIE emitters, the nonradiative decay process caused by molecular motion is suppressed. As a result, **PCN-94** exhibited a Φ_{PL} of almost 100% compared to 30% for **H_4ETTC** at the solid state. Therefore, if we carefully consider predicted MOF structures based on new luminescent organic linkers and SBUs, it is possible to avoid undesired photophysical effects such as self-quenching.

1-4-3. Guest-related emission

Guest-related emission is also divided into emission from the guest itself [57,72–75] and emission from charge transfer or interaction between the guest and the organic linkers or metal clusters.[56,76,77] Introduction or encapsulation of guest molecules into MOFs is an attractive strategy to acquire novel optical properties. The rigid frameworks of MOFs can immobilize organic ligands or encapsulate emitters, leading to the suppression of molecular diffusion and nonradiative decay. Moreover, molecular orientation can be expected because of the well-ordered structures of MOFs. Encapsulation of emitters in individual pores of MOFs can prevent the guest emitters from aggregating with each other. Both MOFs and guest emitters can be selected from a long list of existing ones, which means that synthesis of new luminescent organic ligands is not necessary. Although the introduction of guest emitters within MOF cavities reduces the MOF's porosity, the concentration of guest emitters can be easily tuned by reducing the amount of emitter in the reaction solution used to fabricate the MOF (Table 1-1).

Table 1-2 illustrates that the history of emitters used in the pores of MOFs for guest-related emission. Encapsulation of fluorescent aromatic guests in the pores of a MOF was first demonstrated by M. J. Zaworotko et al. in 2002.[78] In this report, exciplexes were

formed between the organic linker **Bipy** (4,4'-bipyridyl) and the aromatic guest pyrene. Ten years after this report, G. Qian et al. achieved second-order nonlinear optical activity by introducing 4-(4-(diphenylamino)styryl)-1-dodecyl-pyridinium bromide (**DPASD**) in the pores of an anionic indium-based MOF named **ZJU-28**.[79] **ZJU-28** has two types of one dimensional (1D) channels along the *a* and *c* axes of about 6.1 × 6.1 and 7.1 × 8.5 Å, respectively, in which **DPASD** can be uniformly aligned. As a result, second harmonic generation was achieved when excited at 1,064 nm. They then continuously accomplished two-photon-pumped lasing in 2013.[72,80] The aligned organic emitters 4-[*p*-(dimethylamino)styryl]-1-methylpyridinium (**DMASM**) in the 1D channels of **bio-MOF-1** (**$Zn_8(Ad)_4(Bpdc)_6O\cdot 2Me_2HN_2$** (**Ad**: adeninate, **Bpdc**: 4,4'-biphenyldicarboxylic acid)) lead to the enhancement of Φ_{PL} from 1.5% (**DMASM** at solid state) to 25.9% (**DMASM@bio-MOF-1**). Two-photon-pumped red lasing was observed when excited with a 1,064 nm near-infrared pulse laser. Furthermore, three-photon-pumped lasing and whispering gallery modes were realized in **DMASM@ZJU-68** (**ZJU-68**: **$H_2[Zn_3O(C_{17}H_9NO_4)_3]$**) hexagonal prism crystals because of the highly orientation of **DMASM** as well as **DMASM@bio-MOF-1** in 2016.[75] A lasing threshold of ~224 nJ centered at 642.7 nm on excitation at 1,380 nm was achieved. Suppression of nonradiative decay processes including self-quenching and molecular orientation were accomplished owing to the well-ordered structures and isolation of emitter pores.

White luminescence is useful for lighting applications and white LEDs. However, it is difficult to acquire white luminescence because monochromatic emitters rarely emit in the entire visible region. Thus, dichromatic approaches have been mainly used because color-rendering properties can be easily tuned by changing emitter concentrations.

Luminescent MOFs are of great interest to attain efficient white emission because MOFs can encapsulate aromatic guests as an extra emitting molecule even after their synthesis. Highly efficient white-light-emitting solid-state materials were demonstrated by encapsulating a yellow phosphorescent Ir complex, $\mathbf{Ir(ppy)_2(bpy)^+}$ (**ppy**: 2-phenylpyridine, **bpy**: 2,2'-bipyridyl) into a mesoporous blue fluorescent cadmium-based MOF (Cd-MOF) with a Φ_{PL} of 20.4% and Commission International de I'Eclairage (CIE) coordinates of (0.31, 0.33).[73] In 2015, A. Douhal et al. encapsulated two different aromatic guests coumarin 153 and nile red in the pores of **Zr-NDC** (**NDC**: 2,6'-naphthalenedicarboxylic acid).[69] In this case, the highest Φ_{PL} of 33.2% with CIE coordinates of (0.32, 0.34) was achieved.

In these ways, a method of encapsulating luminescent aromatic guests into MOF pores is effective to explore a new class of luminescent materials and photophysical properties that are not successfully realized by aromatic guests or organic linker themselves.

Table 1-1. Advantages and disadvantages of metal-based emission, guest-related emission and ligand-based emission in MOFs.

	Advantages	Disadvantages
Metal-based emission	Narrow emission Long-lived emission (Ln) High surface areas	Need to manage triplet energy level of organic linkers
Ligand-based emission	Maintain high porosity Reduce nonradiative decay Molecular orientation Suppress molecular diffusion	Need to synthesize organic linkers Aggregation Excimer formation Self-quenching
Guest-related emission	Suppress self-quenching Suppress aggregation Suppress molecular diffusion No need to synthesize new emitters Reduce nonradiative decay Molecular orientation	Reduce porosity Size matching

Table 1-2. History of guest-related emission in MOFs

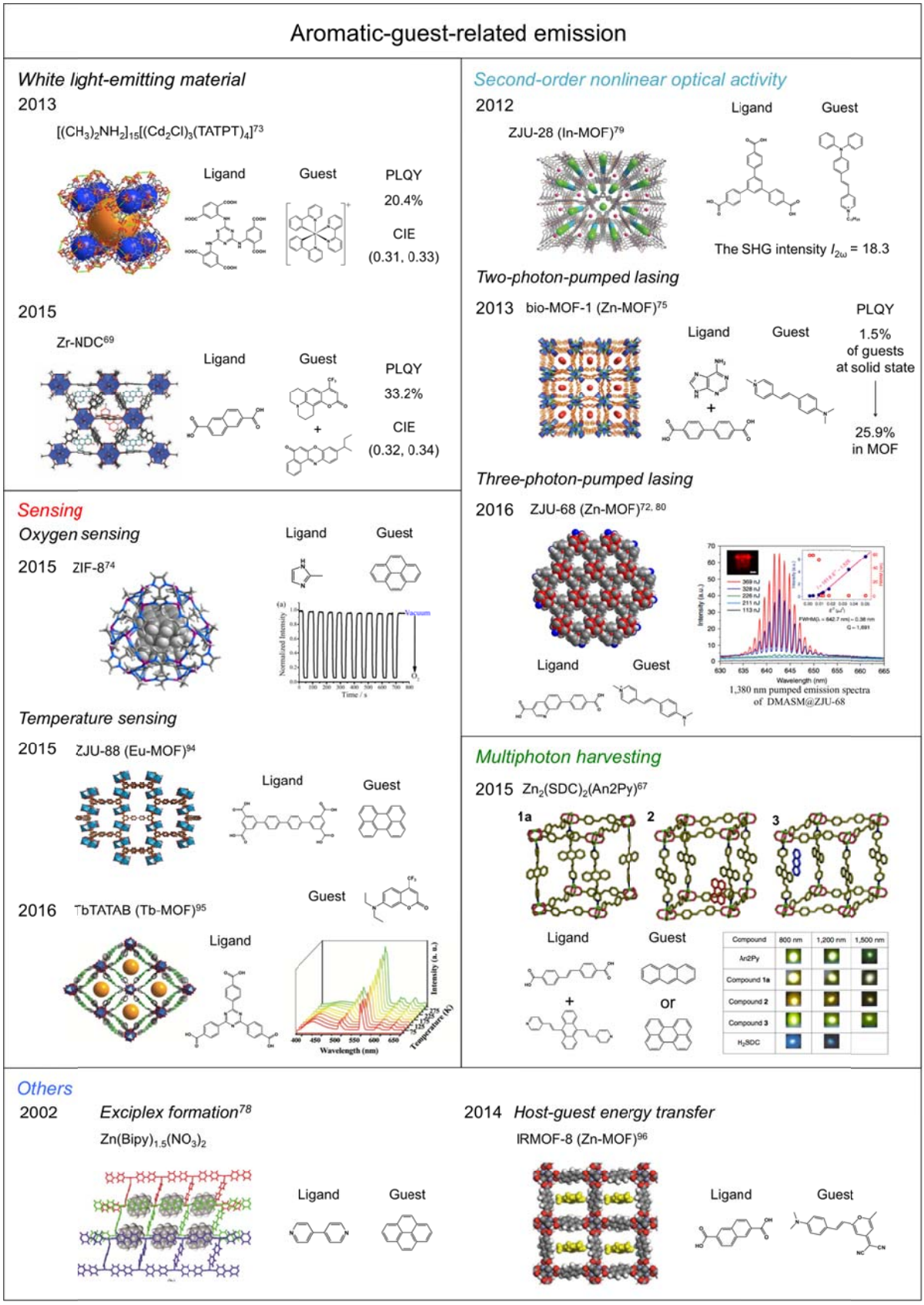

1-4-4. Triplet excitons in MOFs

Just like with organic emitters, triplets can be used for emission from MOFs. The inclusion of heavy atoms to accelerate phosphorescence can be accomplished in several ways. Rare metals such as Ru, Ir, and Re have been incorporated in MOFs as the metal cluster, or metals can be included in the chemical structure of the organic linkers or MOF-entrapped guest molecules.[56,73,81–88] However, triplet excitons in purely aromatic molecules that are used as the organic linkers or that are trapped in a MOF as guest molecules have barely been investigated despite the unique environment that a MOF provides.[67] Following the history of triplet excitons in MOFs (Table 1-3), in 2014, **$[Cd_2(TIPA)_2Cl_4]\cdot 6DMF$** was the first MOF to exhibit phosphorescence from a pure aromatic linker, tri(4-imidazolylphenyl)amine (**TIPA**).[89] However, phosphorescence cannot be observed at room temperature. X.-M. Ren et al. reported the first room temperature phosphorescence (RTP) from a Mg-based MOF consisting of 1,1′-ethynebenzene-3,3′,5,5′-tert-racarboxylic acid (**H_2EBTC**) without any heavy atoms in 2016.[90] Long-lived RTP (τ_p = 0.47 s) was demonstrated in **Zn(BDC)(DMF)·(1-DMF)** (**BDC**: 1,4-benzenedicarboxylic acid) by D. Yang et al. in the same year.[91] They also synthesized **Cd(*m*-BDC)(BIM)** (***m*-BDC**: 1,3-benzenedicarboxylic acid, **BIM**: benzimidazole) exhibiting the long lifetime of 0.75 s at room temperature.[92] Although they mentioned that this Cd-based MOF exhibited reversible pH-responsive phosphorescence for pH values from 3 to 11, X-ray diffraction pattern (XRD) showed the structural changes occurred, indicating that the MOF decomposed under a high pH value. Subsequently, they achieved reversible full color RTP of an anionic MOF (**AMOF-1**), **$CdLi(m\text{-}BDC)_2(Me_2NH_2)$** (**$Me_2NH_2$**: dimethylamine), by a cation exchange with Mn^{2+} at different concentrations.[93]

In total, less than 5 papers demonstrating RTP without heavy atoms have been

reported to date. Moreover, the dynamics of triplet excitons in MOFs have not been deeply discussed. Since I expect that the separation and rigidity offered by a MOF can potentially help suppress the nonradiative deactivation of triplets by self-quenching, thermal deactivation, and energy transfer while not affecting k_p, introduction of triplet-based emitters as organic linkers or encapsulated guest molecules is considered as an attractive option for controlling and realizing triplet exciton dynamics. This strategy could provide a new platform not only for investigating basic photophysical properties but also developing advanced applications for luminescence.

Table 1-3. History of triplet excitons in MOFs

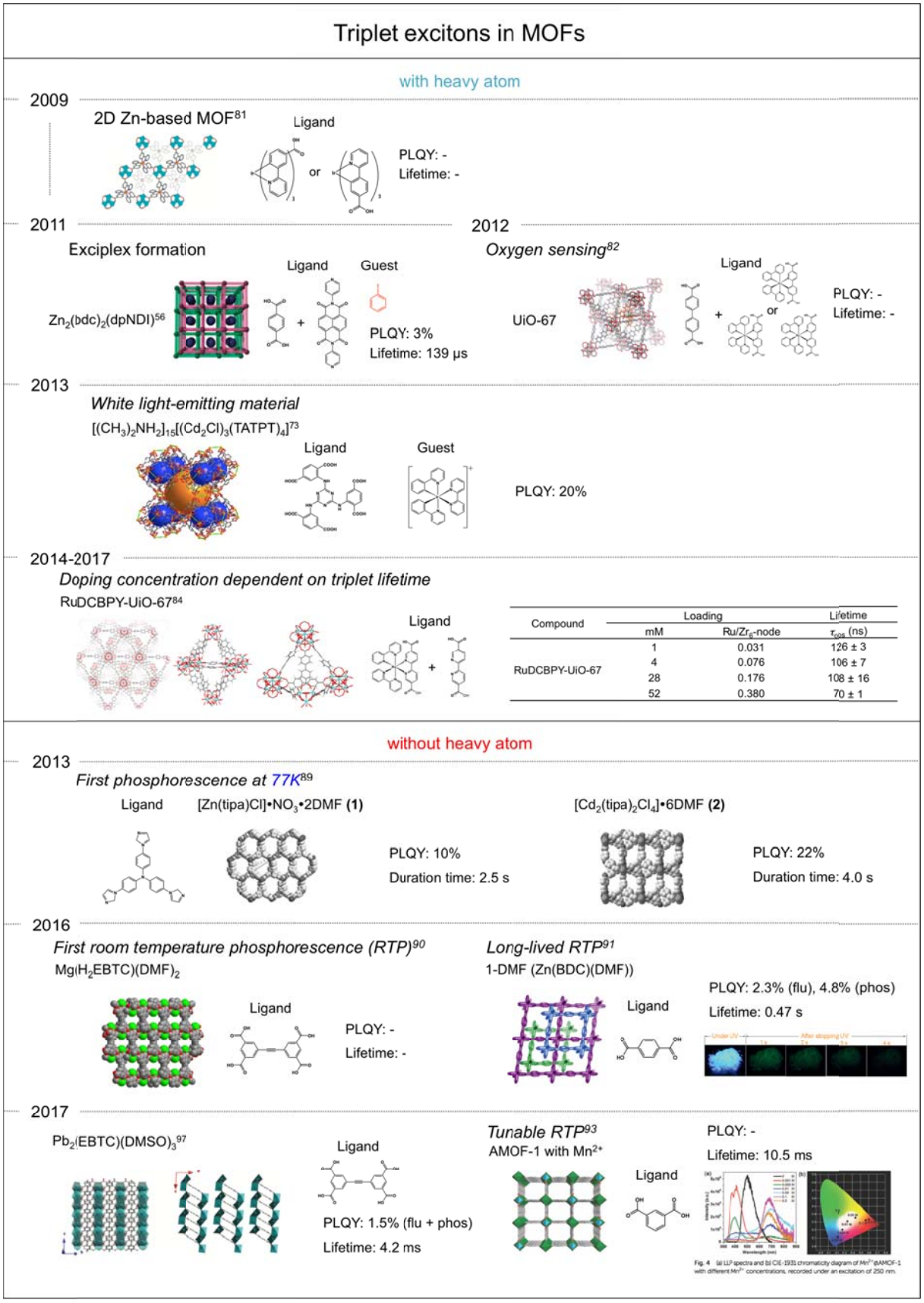

1-5. Outline of this thesis

The goal of this thesis is to develop new ways to control the harvesting of triplet excitons for luminescence by exploiting the rigid environments provided by MOFs. This thesis is organized as follows.

In Chapter 2, I utilize triplet excitons via TADF originating from ligand-based emission. A Zr-based MOF (namely **UiO-68-dpa**) is synthesized based on the newly designed organic linker with TADF properties (**H_2tpdc-dpa**). The linker consists of diphenylamine as an electron-donating moiety and carboxyl groups as both electron-accepting moieties and linkers that bond to the Zr clusters. From this new MOF, TADF characteristics are obtained at room temperature. The interactions among organic linkers, neighboring organic linkers, and metal clusters are discussed in terms of their effects on the emission spectrum, self-quenching, and Φ_{PL}.

In Chapter 3, I obtain long-lived room-temperature phosphorescence from MOFs having guest-related emission. Long-lived phosphorescence is demonstrated with an emission lifetime of 22.4 s at room temperature from coronene-d_{12} encapsulated in the zeolitic imidazolate framework ZIF-8 (**coronene-d_{12}@ZIF-8**). The guest emitter coronene-d_{12} is well isolated in the rigid framework of ZIF-8, enabling long-lived triplet excitons even at temperatures higher than 300 K. Thermally activated delayed fluorescence is also demonstrated at temperatures over 300 K.

In Chapter 4, I demonstrate a new strategy to control the dynamics of triplet excitons in organic emitters by using gases to influence emitters encapsulated in a metal organic framework. Because MOFs intrinsically have a large number of pores that can accommodate gases and aromatic molecules, the heavy-atom gas xenon (Xe) can be introduced into

coronene-d_{12}@ZIF-8 to influence the emission properties of coronene. Triplet excitons accumulated by photoexcitation of coronene-d_{12} under vacuum can be rapidly converted into emission immediately after introduction of Xe. I can easily regulate the timing and speed of extraction of the accumulated triplet excitons as emission by introducing gas mixtures with various concentrations of Xe.

In Chapter 5, the thesis is summarized, and future prospects are discussed.

References

[1] Y. Pak, K. Swamy and J. Yoon, *Sensors*, 2015, **15**, 24374–24396.

[2] M. Fernández-Suárez and A. Y. Ting, *Nat. Rev. Mol. Cell Biol.*, 2008, **9**, 929–943.

[3] T. Mutai, H. Satou and K. Araki, *Nat. Mater.*, 2005, **4**, 685–687.

[4] M. Irie, T. Fukaminato, T. Sasaki, N. Tamai and T. Kawai, *Nature*, 2002, **420**, 759–760.

[5] G. M. Farinola and R. Ragni, *Chem. Soc. Rev.*, 2011, **40**, 3467–3482.

[6] X. Yang, X. Xu and G. Zhou, *J. Mater. Chem. C*, 2015, **3**, 913–944.

[7] Y. Tao, C. Yang and J. Qin, *Chem. Soc. Rev.*, 2011, **40**, 2943–2970.

[8] P.-T. Chou and Y. Chi, *Chem. Eur. J.*, 2007, **13**, 380–395.

[9] A. Kishimura, T. Yamashita, K. Yamaguchi and T. Aida, *Nat. Mater.*, 2005, **4**, 546–549.

[10] S. Hirata, K. S. Lee and T. Watanabe, *Adv. Funct. Mater.*, 2008, **18**, 2869–2879.

[11] H. Sun, S. Liu, W. Lin, K. Y. Zhang, W. Lv, X. Huang, F. Huo, H. Yang, G. Jenkins, Q. Zhao and W. Huang, *Nat. Commun.*, 2014, **5**, 3601.

[12] Y. Liang, A. S. Dvornikov and P. M. Rentzepis, *Proc. Natl. Acad. Sci.*, 2003, **100**, 8109–8112.

[13] C. Adachi, M. A. Baldo, S. R. Forrest and M. E. Thompson, *Appl. Phys. Lett.*, 2000, **77**, 904–906.

[14] A. Endo, M. Ogasawara, A. Takahashi, D. Yokoyama, Y. Kato and C. Adachi, *Adv. Mater.*, 2009, **21**, 4802–4806.

[15] H. Uoyama, K. Goushi, K. Shizu, H. Nomura and C. Adachi, *Nature*, 2012, **492**, 234–238.

[16] Y. Yang, K. Z. Wang and D. Yan, *ACS Appl. Mater. Interfaces*, 2016, **8**, 15489–15496.

[17] C. Ye, L. Zhou, X. Wang and Z. Liang, *Phys. Chem. Chem. Phys.*, 2016, **18**, 10818–10835.

[18] Q. le Masne de Chermont, C. Chaneac, J. Seguin, F. Pelle, S. Maitrejean, J.-P. Jolivet, D. Gourier, M. Bessodes and D. Scherman, *Proc. Natl. Acad. Sci.*, 2007, **104**, 9266–9271.

[19] M. Palner, K. Pu, S. Shao and J. Rao, *Angew. Chem. Int. Ed.*, 2015, **54**, 11477–11480.

[20] S. Hirata, K. Totani, T. Yamashita, C. Adachi and M. Vacha, *Nat Mater*, 2014, **13**, 938–946.

[21] S. Hirata, K. Totani, J. Zhang, T. Yamashita, H. Kaji, S. R. Marder, T. Watanabe and C. Adachi, *Adv. Funct. Mater.*, 2013, **23**, 3386–3397.

[22] S. Hirata and M. Vacha, *Adv. Opt. Mater.*, 2017, **5**, 1600996.

[23] S. Reineke, N. Seidler, S. R. Yost, F. Prins, W. A. Tisdale and M. A. Baldo, *Appl. Phys. Lett.*, 2013, **103**, 93302.

[24] D. Lee, O. Bolton, B. C. Kim, J. H. Youk, S. Takayama and J. Kim, *J. Am. Chem. Soc.*, 2013, **135**, 6325–6329.

[25] S. Scypinski and L. J. C. Love, *Anal. Chem.*, 1984, **56**, 322–327.

[26] J. L. Kropp, W. R. Dawson and R. Dawson, *J. Phys. Chem.*, 1987, **71**, 4499–4506.

[27] P. Montes-Navajas and H. Garcia, *J. Phys. Chem. C*, 2010, **114**, 2034–2038.

[28] M. Kondo, T. Yoshitomi, H. Matsuzaka, S. Kitagawa and K. Seki, *Angew. Chem. Int. Ed.*, 1997, **36**, 1725–1727.

[29] H. Li, M. Eddaoudi, T. L. Groy and O. M. Yaghi, *J. Am. Chem. Soc.*, 1998, **120**, 8571–8572.

[30] D. Britt, H. Furukawa, B. Wang, T. G. Glover and O. M. Yaghi, *Proc. Natl. Acad. Sci.*, 2009, **106**, 20637–20640.

[31] J. A. Mason, M. Veenstra and J. R. Long, *Chem. Sci.*, 2014, **5**, 32–51.

[32] http://www.chemtube3d.com/solidstate/MOF-ZIF8.htm

[33] W. Morris, B. Volosskly, S. Demir, F. Gándara, P. L. McGrier, H. Furukawa, D. Cascio, J. F. Stoddart and O. M. Yaghi, *Inorg. Chem*., 2012, **51**, 6643-6445.

[34] P. Horcajada, T. Chalati, C. Serre, B. Gillet, C. Sebrie, T. Baati, J. F. Eubank, D. Heurtaux, P. Clayette, C. Kreuz, J.-S. Chang, Y. K. Hwang, V. Marsaud, P.-N. Bories, L. Cynober, S. Gil, G. Férey, P. Couvreur and R. Gref, *Nat. Mater*., 2010, **9**, 172-178.

[35] S. Kitagawa, *Angew. Chem. Int. Ed.*, 2015, **54**, 10686–10687.

[36] D. J. Tranchemontagne, J. L. Mendoza-Cortés, M. O'Keeffe and O. M. Yaghi, *Chem. Soc. Rev.*, 2009, **38**, 1257-1283.

[37] N. Stock and S. Biswas, *Chem. Rev.*, 2012, **112**, 933–969.

[38] H. Furukawa, K. E. Cordova, M. O'Keeffe and O. M. Yaghi, *Science*, 2013, **341**, 1230444.

[39] B. Li, H.-M. Wen, W. Zhou and B. Chen, *J. Phys. Chem. Lett.*, 2014, **5**, 3468–3479.

[40] J.-R. Li, R. J. Kuppler and H.-C. Zhou, *Chem. Soc. Rev.*, 2009, **38**, 1477–1504.

[41] L. J. Murray, M. Dincă and J. R. Long, *Chem. Soc. Rev.*, 2009, **38**, 1294–1314.

[42] L. E. Kreno, K. Leong, O. K. Farha, M. Allendorf, R. P. Van Duyne and J. T. Hupp, *Chem. Rev.*, 2012, **112**, 1105–1125.

[43] D. Y. Lee, D. V. Shinde, S. J. Yoon, K. N. Cho, W. Lee, N. K. Shrestha and S. H. Han, *J. Phys. Chem. C*, 2014, **118**, 16328–16334.

[44] R. Kaur, K.-H. Kim, A. K. Paul and A. Deep, *J. Mater. Chem. A*, 2016, **4**, 3991–4002.

[45] K. J. Erickson, F. Léonard, V. Stavila, M. E. Foster, C. D. Spataru, R. E. Jones, B. M. Foley, P. E. Hopkins, M. D. Allendorf and A. A. Talin, *Adv. Mater.*, 2015, **27**, 3453–3459.

[46] J. Lee, O. K. Farha, J. Roberts, K. A. Scheidt, S. T. Nguyen and J. T. Hupp, *Chem. Soc. Rev.*, 2009, **38**, 1450–1459.

[47] T. Zheng, Z. Yang, D. Gui, Z. Liu, X. Wang, X. Dai, S. Liu, L. Zhang, Y. Gao, L. Chen, D. Sheng, Y. Wang, J. Diwu, J. Wang, R. Zhou, Z. Chai, T. E. Albrecht-Schmitt and S. Wang, *Nat. Commun.*, 2017, **8**, 15369.

[48] A. Rabenau, *Angew. Chem. Int. Ed.*, 1985, **24**, 1026–1040.

[49] M. O'Keeffe, M. A. Peskov, S. J. Ramsden and O. M. Yaghi, *Acc. Chem. Res.*, 2008, **41**, 1782–1789.

[50] J. Klinowski, F. A. Almeida Paz, P. Silva and J. Rocha, *Dalt. Trans.*, 2011, **40**, 321–330.

[51] I. Stassen, M. Styles, T. Van Assche, N. Campagnol, J. Fransaer, J. Denayer, J. C. Tan, P. Falcaro, D. De Vos and R. Ameloot, *Chem. Mater.*, 2015, **27**, 1801–1807.

[52] T. Friščić, I. Halasz, P. J. Beldon, A. M. Belenguer, F. Adams, S. A. J. Kimber, V. Honkimäki and R. E. Dinnebier, *Nat. Chem.*, 2012, **5**, 66–73.

[53] O. Shekhah, H. Wang, S. Kowarik, F. Schreiber, M. Paulus, M. Tolan, C. Sternemann, F. Evers, D. Zacher, R. A. Fischer and C. Wöll, *J. Am. Chem. Soc.*, 2007, **129**, 15118–15119.

[54] B. Zhao, X.-Y. Chen, P. Cheng, D.-Z. Liao, S.-P. Yan and Z.-H. Jiang, *J. Am. Chem. Soc.*, 2004, **126**, 15394–15395.

[55] K. L. Wong, G. L. Law, Y. Y. Yang and W. T. Wong, *Adv. Mater.*, 2006, **18**, 1051–1054.

[56] Y. Takashima, V. M. Martínez, S. Furukawa, M. Kondo, S. Shimomura, H. Uehara, M. Nakahama, K. Sugimoto and S. Kitagawa, *Nat. Commun.*, 2011, **2**, 168.

[57] N. Yanai, K. Kitayama, Y. Hijikata, H. Sato, R. Matsuda, Y. Kubota, M. Takata, M. Mizuno, T. Uemura and S. Kitagawa, *Nat. Mater.*, 2011, **10**, 787–793.

[58] F. P. Doty, C. A. Bauer, A. J. Skulan, P. G. Grant and M. D. Allendorf, *Adv. Mater.*, 2009, **21**, 95–101.

[59] K. M. L. Taylor, W. J. Rieter and W. Lin, *J. Am. Chem. Soc.*, 2008, **130**, 14358–14359.

[60] K. M. L. Taylor, A. Jin and W. Lin, *Angew. Chem. Int. Ed.*, 2008, **47**, 7722–7725.

[61] P. Horcajada, R. Gref, T. Baati, P. K. Allan, G. Maurin, P. Couvreur, G. Férey, R. E. Morris and C. Serre, *Chem. Rev.*, 2012, **112**, 1232–1268.

[62] Y. Li, H. Xu, S. Ouyang and J. Ye, *Phys. Chem. Chem. Phys.*, 2016, **18**, 7563–7572.

[63] D. Chen, H. Xing, Z. Su and C. Wang, *Chem. Commun.*, 2016, **52**, 2019–2022.

[64] C. Pagis, M. Ferbinteanu, G. Rothenberg and S. Tanase, *ACS Catal.*, 2016, **6**, 6063–6072.

[65] Y. Cui, B. Chen and G. Qian, *Coord. Chem. Rev.*, 2014, **273–274**, 76–86.

[66] T. M. Reineke, M. Eddaoudi, M. O'Keeffe and O. M. Yaghi, *Angew. Chem. Int. Ed.*, 1999, **38**, 2590–2594.

[67] H. S. Quah, W. Chen, M. K. Schreyer, H. Yang, M. W. Wong, W. Ji and J. J. Vittal, *Nat. Commun.*, 2015, **6**, 7954.

[68] W. Cho, H. J. Lee, G. Choi, S. Choi and M. Oh, *J. Am. Chem. Soc.*, 2014, **136**, 12201–12204.

[69] M. Gutiérrez, F. Sánchez and A. Douhal, *J. Mater. Chem. C*, 2015, **3**, 11300–11310.

[70] M. Gutiérrez, F. Sánchez and A. Douhal, *Phys. Chem. Chem. Phys.*, 2016, **18**, 5112–5120.

[71] Z. Wei, Z. Gu, R. K. Arvapally, Y. Chen, R. N. McDougald, J. F. Ivy, A. A. Yakovenko, D. Feng, M. A. Omary and H. Zhou, *J. Am. Chem. Soc.*, 2014, **136**, 8269–8276.

[72] J. Yu, Y. Cui, H. Xu, Y. Yang, Z. Wang, B. Chen and G. Qian, *Nat. Commun.*, 2013, **4**, 2719.

[73] C. Sun, X. Wang, X. Zhang, C. Qin, P. Li, Z. Su, D.-X. Zhu, G.-G. Shan, K.-Z. Shao, H. Wu and

J. Li, *Nat. Commun.*, 2013, **4**, 2717.

[74] J. W. Ye, H. L. Zhou, S. Y. Liu, X. N. Cheng, R. B. Lin, X. L. Qi, J. P. Zhang and X. M. Chen, *Chem. Mater.*, 2015, **27**, 8255–8260.

[75] H. He, E. Ma, Y. Cui, J. Yu, Y. Yang, T. Song, C.-D. Wu, X. Chen, B. Chen and G. Qian, *Nat. Commun.*, 2016, **7**, 11087.

[76] V. Martínez-martínez, S. Furukawa, Y. Takashima and I. L. Arbeloa, *J. Phys. Chem. C*, 2012, **116**, 26084–26090.

[77] P. L. Feng, K. Leong and M. D. Allendorf, *Dalt. Trans.*, 2012, **41**, 8869–8877.

[78] B. D. Wagner, G. J. McManus, B. Moulton and M. J. Zaworotko, *Chem. Commun.*, 2002, **5**, 2176–2177.

[79] J. Yu, Y. Cui, C. Wu, Y. Yang, Z. Wang, M. O'Keeffe, B. Chen and G. Qian, *Angew. Chem. Int. Ed.*, 2012, **51**, 10542–10545.

[80] T. Song, J. Yu, Y. Cui, Y. Yang and G. Qian, *Dalt. Trans.*, 2016, **45**, 4218–4223.

[81] Z. Xie, L. Ma, K. E. DeKrafft, A. Jin and W. Lin, *J. Am. Chem. Soc.*, 2010, **132**, 922–923.

[82] S. M. Barrett, C. Wang and W. Lin, *J. Mater. Chem.*, 2012, **22**, 10329–10334.

[83] W. A. Maza and A. J. Morris, *J. Phys. Chem. C*, 2014, **118**, 8803–8817.

[84] W. A. Maza, R. Padilla and A. J. Morris, *J. Am. Chem. Soc.*, 2015, **137**, 8161–8168.

[85] Y. Zhao, H. Xu, Y. Fu, K. Shao, S. Yang, Z.-M. Su, X.-R. Hao, D.-X. Zhu and E.-B. Wang, *Cryst. Growth Des.*, 2008, **8**, 3566–3576.

[86] C. L. Whittington, L. Wojtas and R. W. Larsen, *Inorg. Chem.*, 2014, **53**, 160–166.

[87] X.-L. Qi, S.-Y. Liu, R.-B. Lin, P.-Q. Liao, J.-W. Ye, Z. Lai, Y. Guan, X.-N. Cheng, J.-P. Zhang and X.-M. Chen, *Chem. Commun.*, 2013, **49**, 6864–6866.

[88] S. Zhan, M. Li, W. Ng and D. Li, *Chem. Eur. J.*, 2013, **19**, 10217–10225.

[89] S. Yuan, Y. K. Deng and D. Sun, *Chem. Eur. J.*, 2014, **20**, 10093–10098.

[90] L. Zhai, W.-W. Zhang, J.-L. Zuo and X.-M. Ren, *Dalt. Trans.*, 2016, **45**, 11935–11938.

[91] X. Yang and D. Yan, *Chem. Sci.*, 2016, **7**, 4519–4526.

[92] Y. Yang, K. Z. Wang and D. Yan, *ACS Appl. Mater. Interfaces*, 2016, **8**, 15489–15496.

[93] X. Yang and D. Yan, *J. Mater. Chem. C*, 2017, **5**, 7898–7903.

[94] Y. Cui, R. Song, J. Yu, M. Liu, Z. Wang, C. Wu, Y. Yang, Z. Wang, B. Chen and G. Qian, *Adv. Mater.*, 2015, **27**, 1420–1425.

[95] T. Xia, T. Song, Y. Cui, Y. Yang and G. Qian, *Dalt. Trans.*, 2016, **45**, 18689–18695.

[96] D. Yan, Y. Tang, H. Lin and D. Wang, *Sci. Rep.*, 2015, **4**, 4337.

[97] X. Liu, L. Zhai, W.-W. Zhang, J.-L. Zuo, Z.-X. Yang and X.-M. Ren, *Dalt. Trans.*, 2017, **46**, 7953–7959.

Chapter 2

Thermally activated delayed fluorescence
of a Zr-based metal-organic framework

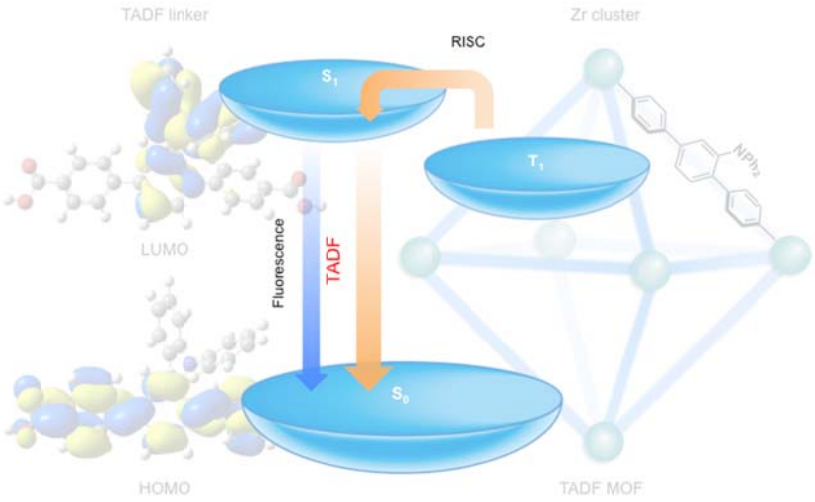

Hiroyuki Mieno, Ryota Kabe, Mark D. Allendorf, and Chihaya Adachi

Chemical Communications, in press.

2-1. Introduction

Organic molecules exhibiting TADF are being actively developed for highly efficient OLEDs.[1] Capable of harvesting 100% of excitons, TADF molecules produce delayed fluorescence when singlet excitons produced by the reverse intersystem crossing of triplet excitons radiatively decay. Delayed fluorescence is also useful for bioimaging applications because the delayed emission can be temporally separated from the excitation light.[2,3] However, most organic emitters needed to be dispersed into solvents or host molecules to avoid concentration quenching of the emission. Furthermore, the charge-transfer emission of TADF molecules is strongly affected by the polarity of solvents or host molecules and often quenched in polar solvents like water, complicating film optimization and hindering biological applications.

The high surface area, porosity, thermal stability, chemical stability, and structural tunability of MOFs possibly offer a way to modify some of these effects.[4] MOFs are hybrid porous materials composed of metal-clusters and organic linkers. Because their rigid frameworks inhibit nonradiative deactivation[5,6] and prevent aggregation of emitters,[7,8] solid-state emission can be observed by introducing luminescent organic molecules into MOFs as linkers or guests.[9] Such solid-state luminescent MOFs are useful for bioapplications, including bioimaging[10] and drug delivery[11], photocatalysts[12] and chemical sensors[13]. Although a wide variety of luminescent MOFs have been demonstrated to date and I previously showed that guest molecules within MOF pores can exhibit TADF,[7] a MOF exhibiting intrinsic TADF has never been reported. MOFs exhibiting TADF could be an avenue to achieving higher thermal and chemical stability than in conventional TADF molecules and may offer new ways to tune TADF properties, such as delayed lifetime and emission spectrum, by varying the

selection of metals and size of pores.

Here, I design a new linker with TADF properties for use in MOFs. The linker, **H_2tpdc-dpa**, has both electron-donating and electron-accepting moieties with a large dihedral angle between them. Based on this TADF linker, I developed a zirconium-based MOF that is the first to exhibit intrinsic TADF at room temperature.

2-2. Calculation and design of organic linker

Most TADF molecules consist of electron donor and acceptor units separated by a large dihedral angle to effectively separate the highest occupied molecular orbital (HOMO) and the lowest unoccupied molecular orbital (LUMO) of the molecule. The resulting small spatial overlap between the HOMO and the LUMO leads to a small energy gap between the lowest singlet excited state and the lowest triplet excited state (ΔE_{ST}).

Organic linkers used in MOFs often contain a carboxyl unit as the functional group that coordinates with the metal center. Since a carboxyl group acts as an electron acceptor, TADF emission might be obtained by adding an electron-donating unit to the linker to induce the spatial separation of the HOMO and LUMO. For example, the organic linker **H_2tpdc-NH_2**, which was used in the MOF (**UiO-68-NH_2)**, contains an electron-accepting carboxylic acid and an electron-donating amino group.[14] The ΔE_{ST} of this linker was calculated to be as high as 0.66 eV using density functional theory (B3LYP/6-31G level). This large value is the result of a small dihedral angle between the donor and acceptor moieties (Fig. 2-1a) and is too high to enable the efficient conversion of triplet excitons to singlet excitons at room temperature. To obtain a smaller ΔE_{ST}, I designed the novel linker **H_2tpdc-dpa**, which consists of carboxyl and diphenyl amino moieties. A large steric hindrance between the donor and acceptor

moieties induces a separation of HOMO and LUMO, leading to a moderately small calculated ΔE_{ST} of 0.2 eV (Fig. 2-1b).

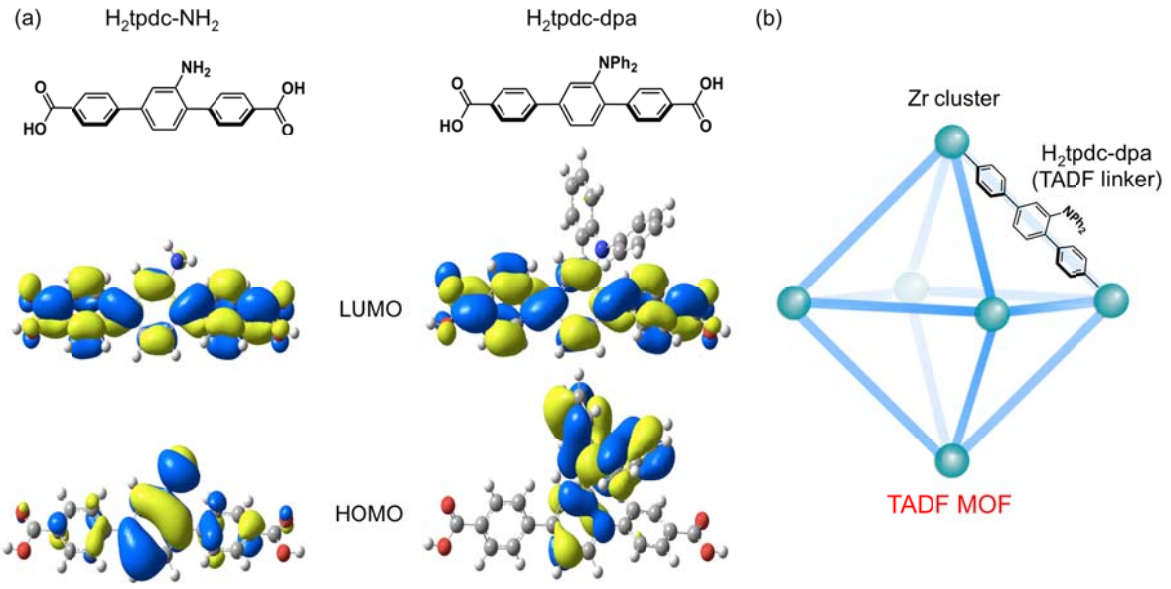

Figure 2-1. (a) HOMO and LUMO distributions of **H_2tpdc-NH_2** (left) and **H_2tpdc-dpa** (right) calculated at the B3LYP/6-31G level. (b) Schematic structure of **UiO-68-dpa**

2-3. Experimental

2-3-1. Materials

All starting materials were purchased from commercial suppliers and were used as received. 4,4”-Dimethoxycarbonyl-2’-amino-[1,1’:4’,1”]terphenyl, **H_2tpdc-NH_2**, and 2,5-dibromo-*N*,*N*-diphenylaminobenzene (**1**) were prepared as described in the literature[14,15].

2-3-2. Equipment

^{1}H and ^{13}C NMR spectra were recorded on a Bruker AVANCE III 500 MHz spectrometer. Elemental analyses (C, H, N) were carried out using a Yanaco MT-5 CHN corder. Solution and thin-film UV–vis absorption spectra were recorded on a Perkin-Elmer

Lambda 950-PKA UV–vis spectrophotometer. Photoluminescence quantum yields were obtained from an absolute photoluminescence quantum yield measurement system (Quantaurus-QY C11347-01, Hamamatsu Photonics). The photoluminescence decay characteristics of the solution samples were recorded using a fluorescence lifetime measurement system (Quantaurus-Tau, Hamamatsu Photonics). The photoluminescence decay characteristics of the film samples were recorded under vacuum using a streak camera (C4334, Hamamatsu Photonics) equipped with a N_2 gas laser (KEN-X, Usho, λ = 337 nm, pulse width ≈ 500 ps, repetition rate = 20 Hz) as the excitation source. Low-temperature measurements were conducted using a cryostat (CRT-006-2000, Iwatani Industrial Gases). X-ray diffraction patterns were obtained using a Rigaku Ultima IV diffractometer with CuKα radiation. Thermogravimetric analysis data were measured with a rate of 10 °C/min using a Bruker TG-DTA2400SA analyser.

2-3-3. Calculation

All quantum chemical calculations were performed using the Gaussian 09 program package Geometry optimization was carried out using the B3LYP functional with the 6-31G(d) basis set. Low-lying excited singlet and triplet states were computed using the optimized structures with time-dependent density functional theory (TD-DFT) at the same level.

2-3-4. Synthesis

Scheme 2-1.

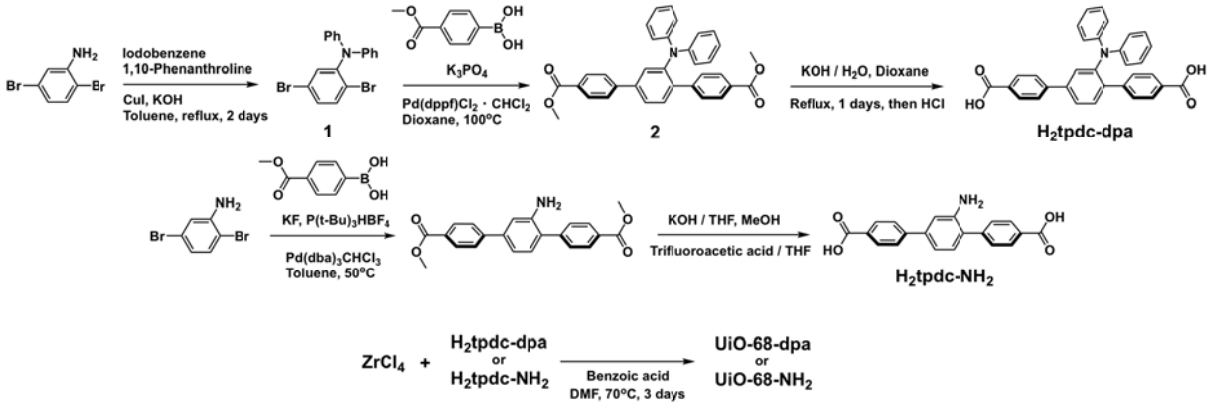

4,4”-Dimethoxycarbonyl-2’-diphenylamino-[1,1’:4’,1”]terphenyl (**2**)

To a dioxane (50 mL) solution of **1** (0.60 g, 1.5 mmol), 4-(methoxycarbonyl)-phenylboronic acid (0.6 g, 3.3 mmol), K_3PO_4 (1.27 g, 6.0 mmol) and [1,1’-bis-(diphenylphosphino)ferrocene]dichloropalladium(II) complex with dichloromethane ($Pd(dppf)Cl_2 \cdot CH_2Cl_2$) (0.12 g, 0.15 mmol) were added. The mixture was heated to 100 °C for 2 days under Ar. The resulting solution was cooled to room temperature and extracted with CH_2Cl_2. The organic layer was filtered with celite and concentrated under reduced pressure. The resulting crude product was subjected to silica gel column chromatography (hexane:CH_2Cl_2 = 4:1) to afford 0.43 g of **2** in a 56% yield as a yellowish white solid.

^{1}H NMR (500 MHz, $CDCl_3$, 25 °C): δ (ppm) = 8.08 (d, *J* = 8.2 Hz, 2H), 7.80 (d, 8.1 Hz, 2H), 7.63 (d, *J* = 8.2 Hz, 2H), 7.60 (s, 1H), 7.54 (d, *J* = 8.0 Hz, 1H), 7.41 (d, *J* = 8.0 Hz, 1H), 7.28 (d, *J* = 8.2 Hz, 2H), 7.08 (t, 4H), 6.88 (d, *J* = 7.8 Hz, 4H), 6.84 (t, 2H), 3.91 (d, *J* = 28 Hz, 6H). ^{13}C NMR: (125 MHz, $CDCl_3$, 25 °C): δ (ppm) = 167.00, 166.88, 147.21, 145.66, 144.31, 144.12, 141.25, 138.92, 132.32, 130.15, 129.27, 129.22, 128.88, 128.51, 128.47, 128.04, 126.95, 124.47, 122.21, 121.83, 52.18, 52.02. MS (MALDI-TOF-MS): m/z 512.76

$[M]^+$ Elemental analysis: calcd. for $C_{34}H_{27}NO_4$: C, 79.5; H, 5.30; N, 2.73; found: C, 79.3; H, 5.31; N, 2.70

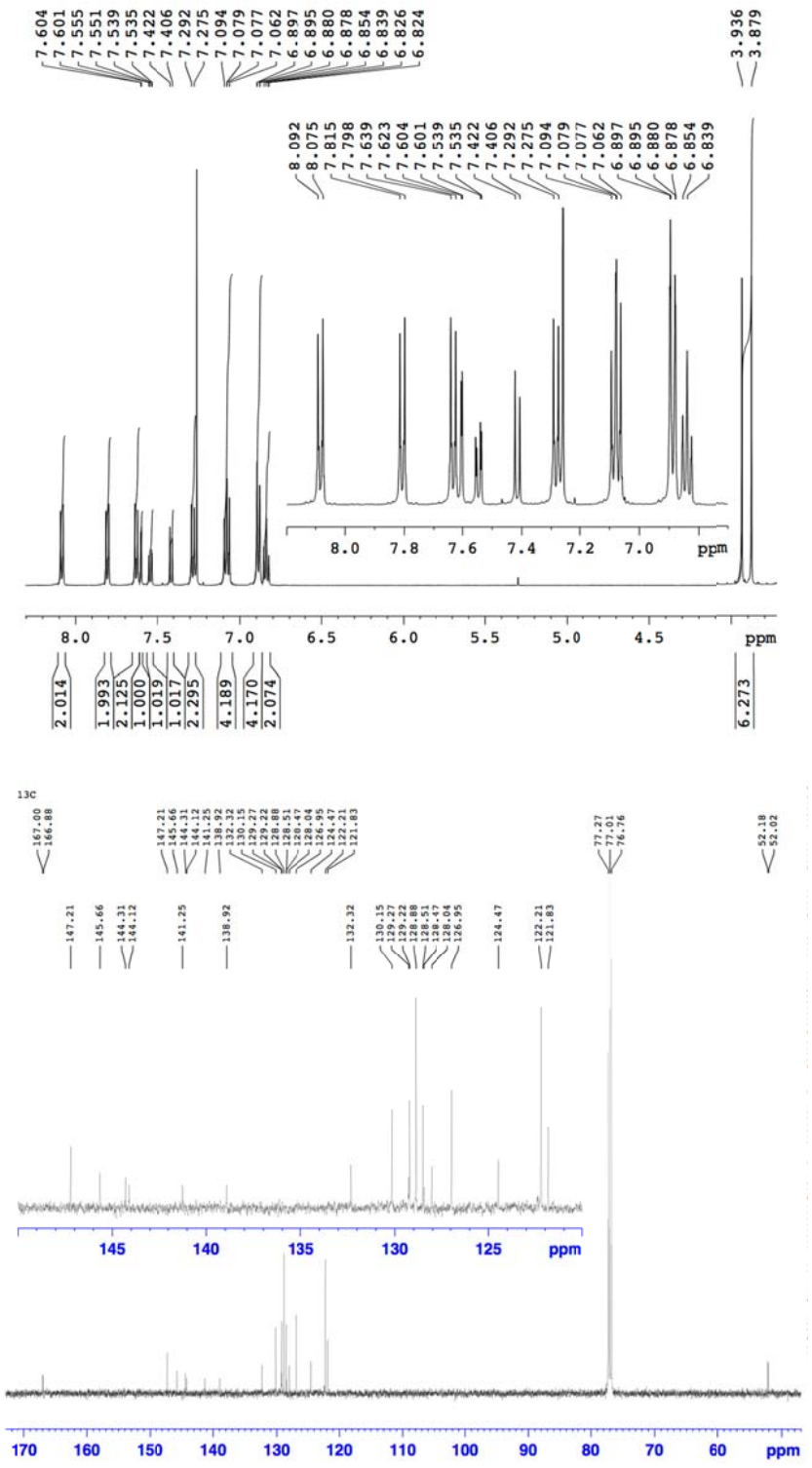

Figure 2-2. ^1H and ^{13}C NMR spectra of compound **2**.

4,4”-Dicarboxyl-2’-diphenylamino-[1,1’:4’,1”]terphenyl (**H_2tpdc-dpa**)

To a dioxane (20 mL) solution of **2** (0.20 g, 0.4 mmol), KOH (0.17 g, 3.0 mmol) in aqueous solution (10 mL) was added and refluxed overnight. The resulting clear solution was cooled to room temperature and treated with hydrochloric acid (concentrated HCl) through an addition funnel with ice bath until the solution reached a pH of 1. Then, the mixture was stirred for another 1 hour. Finally, the precipitate was filtered and dried under vacuum to give **H_2tpdc-dpa** as a yellow powder (0.18 g, 93%).

^{1}H NMR (500 MHz, DMSO, 25 °C): δ (ppm) = 12.9 (br, 2H), 8.01 (d, *J* = 8.5 Hz, 2H), 7.75 (m, 5H), 7.57 (d, *J* = 8.7 Hz, 1H), 7.53 (d, *J* = 8.0 Hz, 1H), 7.36 (d, *J* = 8.3 Hz, 2H), 7.13 (t, 4H), 6.85 (t, 6H). ^{13}C NMR: (125 MHz, CDCl3, 25 °C): δ (ppm) = 167.53, 167.50, 147.26, 145.45, 143.46, 140.97, 138.81, 133.00, 130.55, 129.65, 129.51, 129.44, 128.78, 127.98, 127.25, 122.27, 122.23. MS (MALDI-TOF-MS): m/z 484.69 $[M]^+$ Elemental analysis: calcd. for $C_{32}H_{23}NO_4$: C, 79.2; H, 4.74; N, 2.88; found: C, 79.0; H, 4.87; N, 2.87

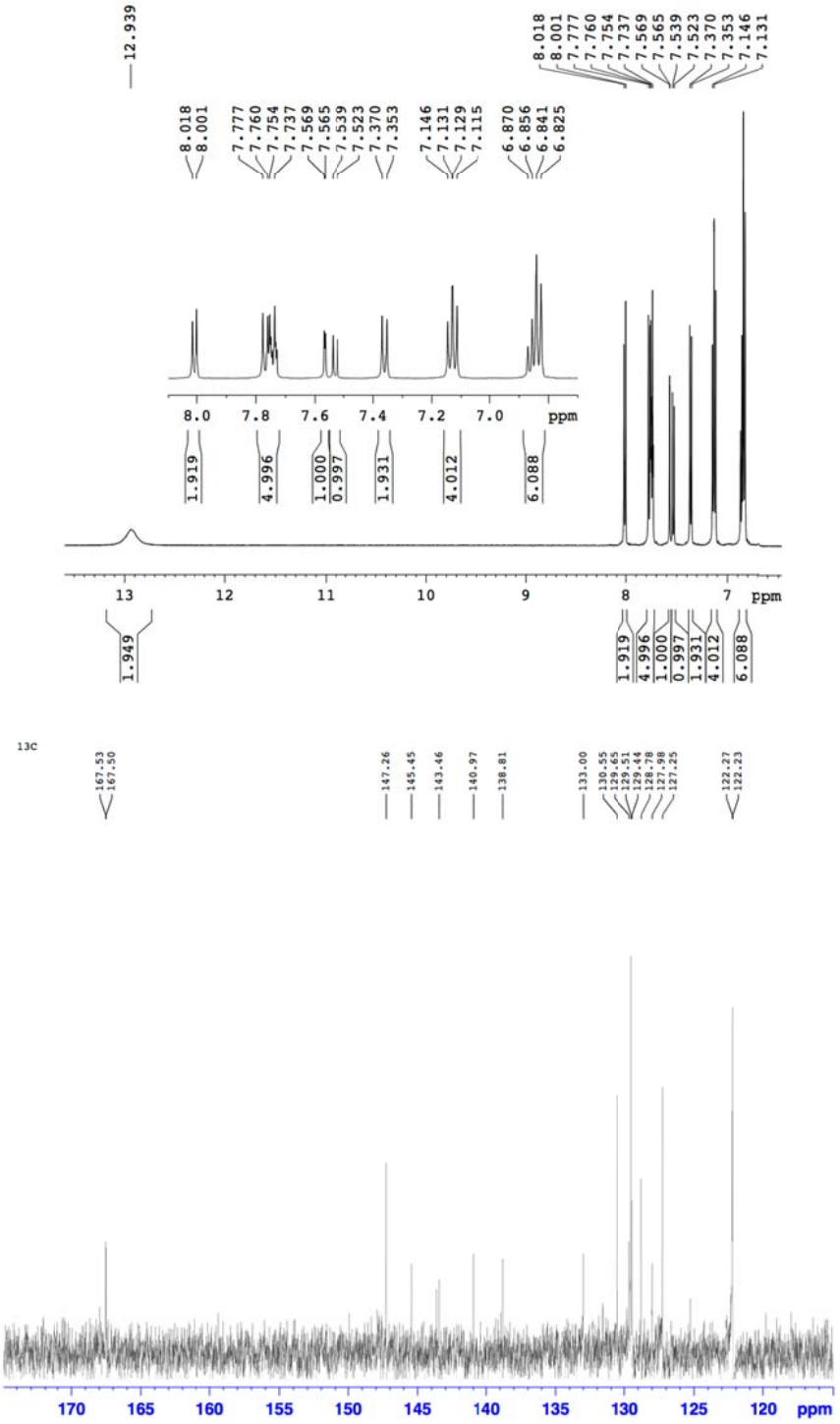

Figure 2-3. ^{1}H and ^{13}C NMR spectra of **H_2tpdc-dpa**.

Synthesis of UiO-68-NH_2 and UiO-68-dpa

In a 6-dram vial, a DMF solution (10 mL) of **H_2tpdc-NH_2** (67 mg, 0.2 mmol) or **H_2tpdc-dpa** (97 mg, 0.2 mmol), $ZrCl_4$ (57 mg, 0.2 mmol), benzoic acid (**UiO-68-NH_2**: 488 mg, 4.0 mmol; **UiO-68-dpa**: 122 mg, 1.0 mmol) and water (18 μL) was heated to 70 °C for 3 days. After cooling to room temperature, the precipitates were isolated by centrifugation. The solids were suspended in DMF (20 mL). After standing at room temperature for 1 day, the suspensions were centrifuged and the solvent was decanted off. This treatment was repeated five times to remove the unreacted organic linker. Afterwards the same procedure was performed with ethanol (20 mL × 3). The solids were dried at 120 °C for 12 h under reduced pressure.

Elemental analysis of UiO-68-dpa: calcd. for $Zr_6O_5(OH)_3(H_2tpdc\text{-}dpa)_{5.5}\cdot 11H_2O$: C, 59.8; H, 3.98; N, 2.18; found: C, 59.3; H, 3.70; N, 2.31

2-4. Characterization of UiO-68-dpa

Both **H_2tpdc-NH_2** and **H_2tpdc-dpa** linkers and their Zr-based MOFs (**UiO-68-NH_2** and **UiO-68-dpa**, respectively) were synthesized and characterized (Scheme 2-1). The powder X-ray diffraction pattern of **UiO-68-dpa** reveals the crystallinity of the MOF, and the diffraction peaks are similar to those of **UiO-68-NH_2**, which has two different-shaped cavities in the structure (Figs. 2-1 and 2-4).[14] The nitrogen isotherms of **UiO-68-dpa**, with a step at P/P_0 of 0.2, are also consistent with the presence of two types of cavities (Fig. 2-5). The BET surface area of **UiO-68-dpa** was calculated to be 1455 m^2/g, which is smaller than that of **UiO-68-2CH_3** (2470 m^2/g)[15] because the diphenylamine of **H_2tpdc-dpa** partially occupies the cavities. Scanning electron microscopy images reveal an octahedral morphology for

UiO-68-dpa with a particle size of less than 10 μm (Fig. 2-6). Thermogravimetric analysis of **UiO-68-dpa** shows no substantial weight loss up to 700 K even though **H_2tpdc-dpa** decomposes at around 650 K, indicating that **UiO-68-dpa** has good thermal stability (Fig. 2-7). The small weight loss at 400 K is due to residual DMF.

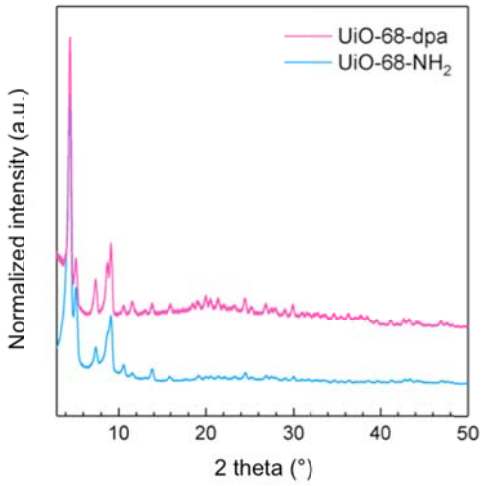

Figure 2-4. (Left) XRD patterns of **UiO-68-NH_2** (blue) and **UiO-68-dpa** (red). (Right) Thermogravimetric analysis of **H_2tpdc-dpa** (blue) and **UiO-68-dpa** (red).

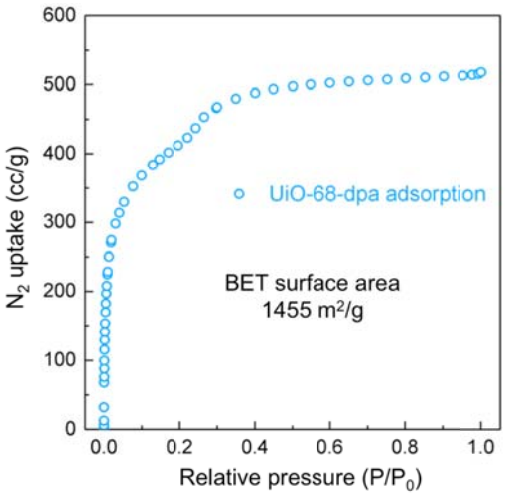

Figure 2-5. Nitrogen adsorption isotherms of **UiO-68-dpa** at 77K.

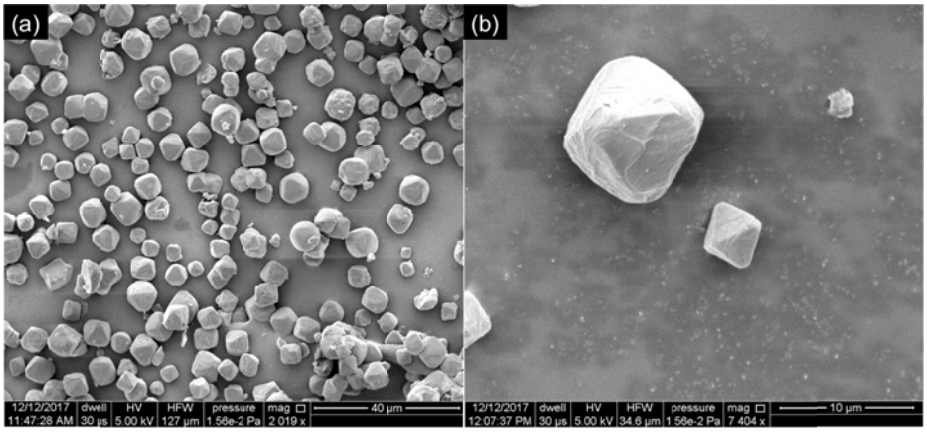

Figure 2-6. SEM images of **UiO-68-dpa** with scale bars of (a) 40 µm and (b) 10 µm.

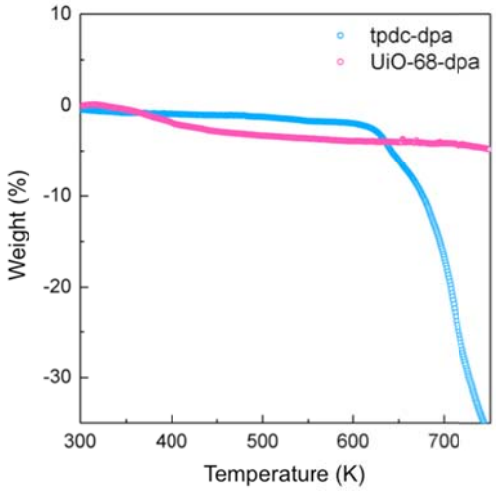

Figure 2-7. Thermogravimetric analysis of **H_2tpdc-dpa** (blue) and **UiO-68-dpa** (red).

2-5. Results and discussion

2-5-1. Photophysical properties of H_2tpdc-dpa and UiO-68-dpa

UV-vis absorption and emission spectra of **H_2tpdc-dpa** in tetrahydrofuran (THF) solution and **UiO-68-dpa** dispersed in THF are shown in Fig. 2-8a, and the photophysical properties are summarized in Table 2-1. The absorption spectrum of **H_2tpdc-dpa** shows two absorption peaks at 291 and 370 nm, which are attributable to π-π* and charge-transfer transitions, respectively. The **H_2tpdc-dpa** linker exhibits broad charge-transfer emission with a peak at 481 nm in THF solution. The phosphorescence spectrum of **H_2tpdc-dpa** in THF was observed at 77 K (Fig. 2-8b), and the ΔE_{ST} was estimated to be 0.24 eV from the offset between the fluorescence and phosphorescence spectra, which is good agreement with the calculation results.

Although **H_2tpdc-dpa** also exhibits charge-transfer emission when doped in a solid-state film of PMMA, the emission peak maximum (Fig. 2-9) was red-shifted from 461 nm to 500 nm by increasing the concentration from 2 wt% to 50 wt%, indicating that **H_2tpdc-dpa** aggregates at higher concentrations. We investigated the emission decay of **H_2tpdc-dpa** doped at different doping concentrations (2 wt%, 5 wt%, and 10 wt%) into PMMA (Fig. 2-10). All films exhibit double exponential decay corresponding to prompt fluorescence and the delayed fluorescence. These results indicate that **H_2tpdc-dpa** exhibits TADF characteristics in both the isolated and aggregated states. Although the prompt emission decay is almost constant at all concentrations, the delayed emission lifetime decreases with increasing doping concentration because of concentration quenching.

The photophysical properties of **UiO-68-dpa** were measured after activation of **UiO-68-dpa** at 400 K under vacuum. The emission spectrum of **UiO-68-dpa** obtained from a

THF dispersion is broader and red-shifted compared to that of **H_2tpdc-dpa** in THF solution (Fig. 2-8).

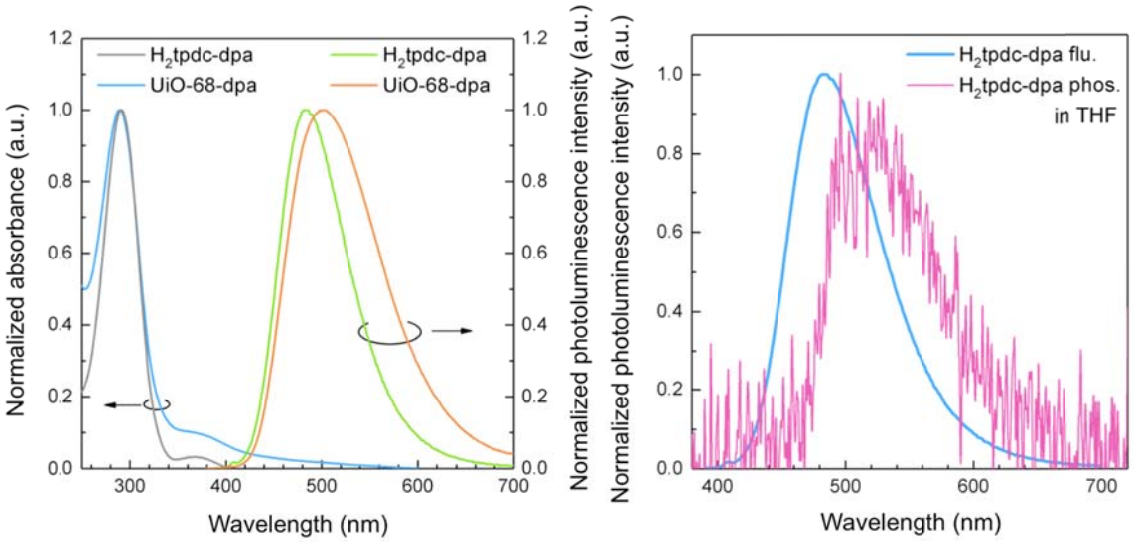

Figure 2-8. (a) UV-vis and photoluminescence spectra of **H_2tpdc-dpa** dissolved in THF and **UiO-68-dpa** dispersed in THF. (b) Fluorescence (blue line) and phosphorescence (red line) spectra of **H_2tpdc-dpa** in THF (10^{-6} M). Fluorescence was measured at room temperature and phosphorescence at 77 K.

Table 2-1. Photophysical properties of **H_2tpdc-dpa** and **UiO-68-dpa**

Compound	Condition	λ_{max} (nm)[a]	CIE	Φ_{air} (%)	Φ_{inert} (%)	τ_{prompt} (ns)	$\tau_{delayed}$ (ms)
H_2tpdc-dpa	2wt% doped PMMA film	461	(0.16, 0.18)	32	39[b]	18	199
	THF (10^{-6} M)	481	(0.18, 0.34)	23	42[b]	-	-
UiO-68-dpa	Solid state	501	(0.24, 0.44)	18	30[c]	17	0.18

[a]The maximum peak of fluorescence. [b]Measured under N_2. [c]Measured under the vacuum of a turbo molecular pump.

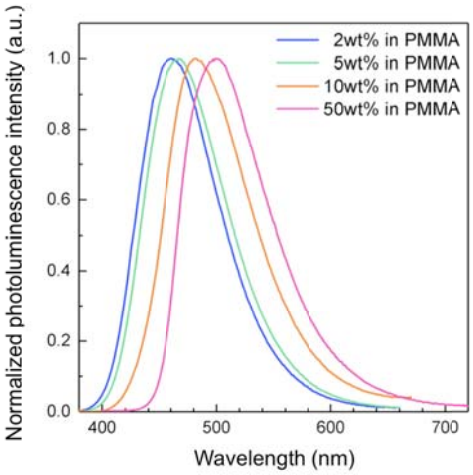

Figure 2-9. Fluorescence spectra of a PMMA doped with **H_2tpdc-dpa** in various concentrations (2 wt%; blue line, 5 wt%: green line, 10 wt%; orange line, 50 wt%; red line).

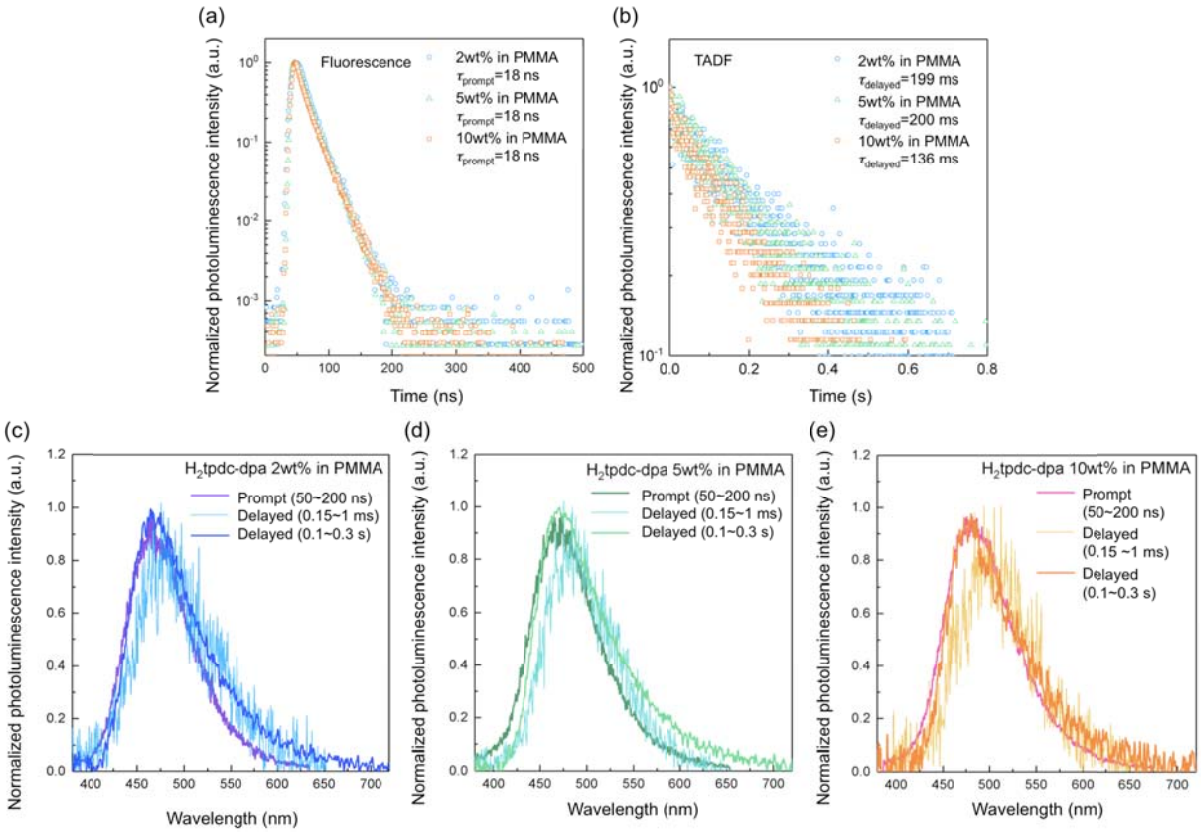

Figure 2-10. Room-temperature decay profiles of **H_2tpdc-dpa**–doped PMMA films at various doping concentrations at time scale of 500 ns (a) and 1 s (b). (c)–(e) Prompt and delayed emission spectra of the films in (a) and (b).

2-5-2. Thermally activated delayed fluorescence of UiO-68-dpa

The emission decay curves of **UiO-68-dpa** were obtained under vacuum condition at temperatures ranging from 30 K to 300 K (Fig. 2-11a). **UiO-68-dpa** clearly exhibited green emission with both the prompt and delayed components (Fig. 2-11b). The lifetime of the delayed component at room temperature is 180 μs, much lower that of a 2wt% **H_2tpdc-dpa** doped PMMA film (199 ms) (Table 1). The spectrum shift and decreased lifetime of the delayed component may be due to the coordination interaction between the carboxylic acid and the Zr ion[16] or the interaction between two adjacent organic linkers in the MOF.[5,17] The increase of delayed emission intensity from **UiO-68-dpa** with temperature is consistent with TADF. Moreover, the delayed emission intensity is proportional to the excitation intensity, so the delayed fluorescence of **UiO-68-dpa** can be attributed to TADF and not triplet-triplet annihilation (Fig. 2-12).

The delayed emission spectrum of **UiO-68-dpa** is slightly red-shifted from that of the prompt emission (Fig. 2-11b). This emission spectrum change may originate from the structural relaxation of ligands in the MOF, because the benzene ring at a center position of the terphenyl group of **H_2tpdc-dpa** can rotate even at low temperatures according to the single-crystal data of **UiO-68-NH_2**.[14] In contrast, **UiO-68-NH_2** shows no delayed fluorescence at room temperature (Fig. 2-13), which is consistent with the large calculated ΔE_{ST} of 0.60 eV for **H_2tpdc-NH_2**.

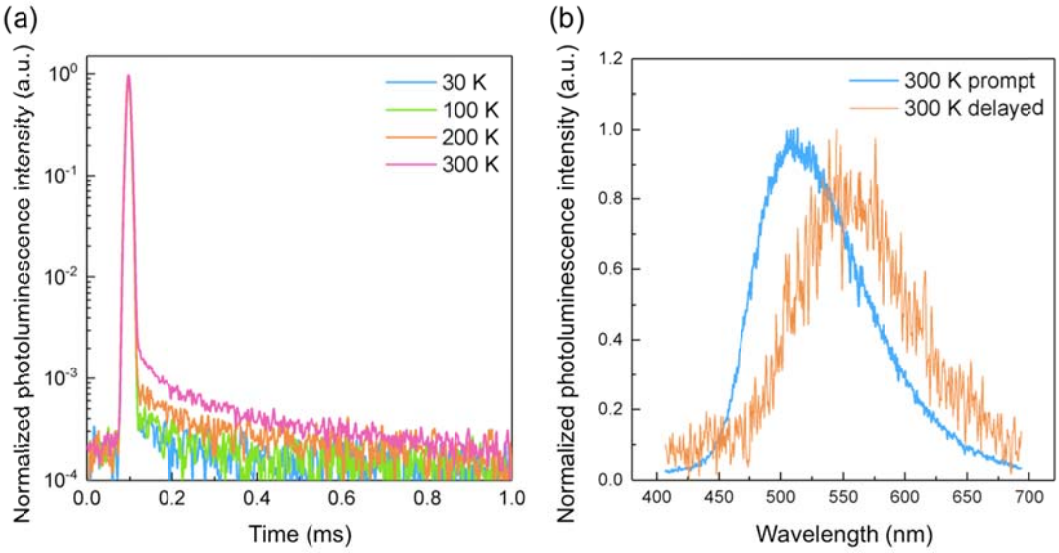

Figure 2-11. (a) Temperature-dependent transient decay profiles of **UiO-68-dpa** under vacuum. (b) Emission spectra at room temperature of **UiO-68-dpa** under vacuum (prompt component: blue line; delayed component: orange line).

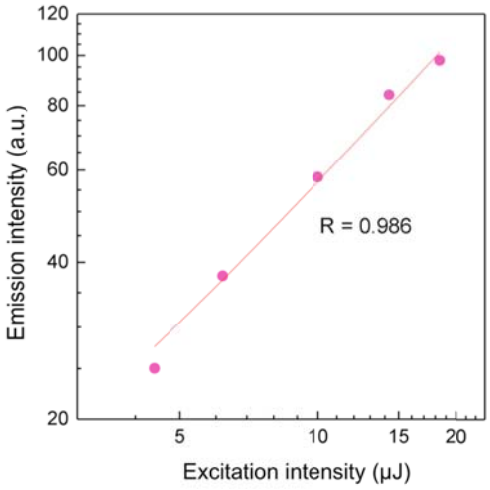

Figure 2-12. Excitation intensity dependence of the delayed emission intensity of **UiO-68-dpa**.

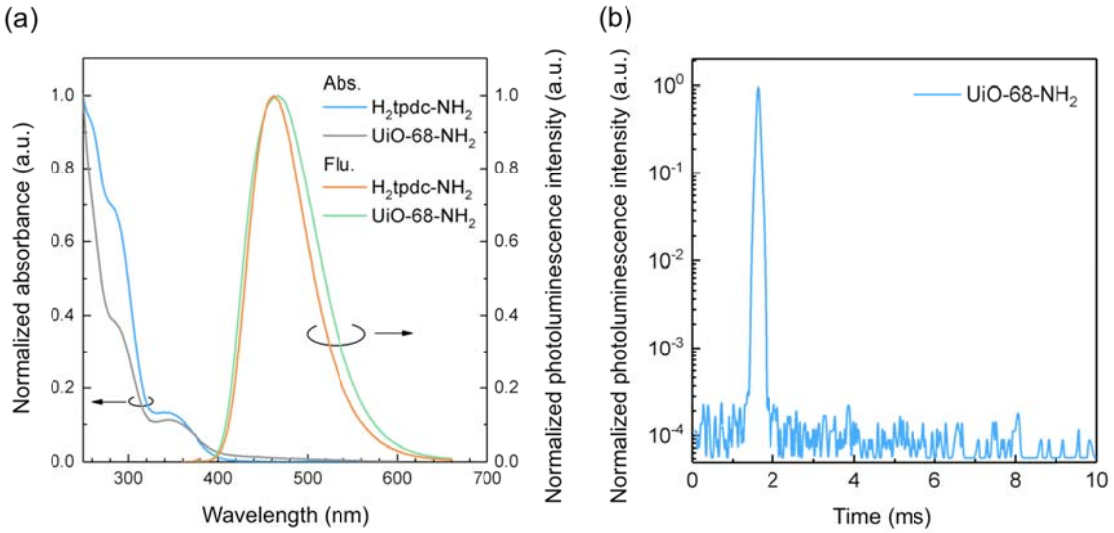

Figure 2-13. (a) UV-vis absorption spectra and fluorescence spectra of **H_2tpdc-NH_2** and **UiO-68-NH_2**. (b) Decay profiles of **UiO-68-NH_2** at 300 K under vacuum.

Because MOFs can efficiently adsorb molecules such as gases and solvents owing to their large surface areas, the TADF properties of **UiO-68-dpa** may be sensitized to the environment. Therefore, the emission spectra and decay profiles of **UiO-68-dpa** were investigated when introducing oxygen and organic solvents into the pores of **UiO-68-dpa**. The delayed emission was completely quenched in air because oxygen acts as a triplet quencher (Fig. 2-14). As a result, the photoluminescence quantum yield (Φ) decreased from 30% to 18% (Table 1). The emission spectrum of **UiO-68-dpa** is also slightly shifted depending on the solvent polarity because of the charge-transfer transition (Fig. 2-15). Although these shifts are small, they suggest a method of tuning the color of light emitted by an OLED.

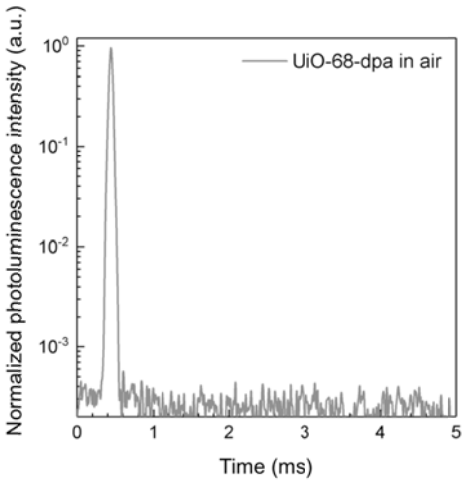

Figure 2-14. Decay profiles of **UiO-68-dpa** at 300 K in air.

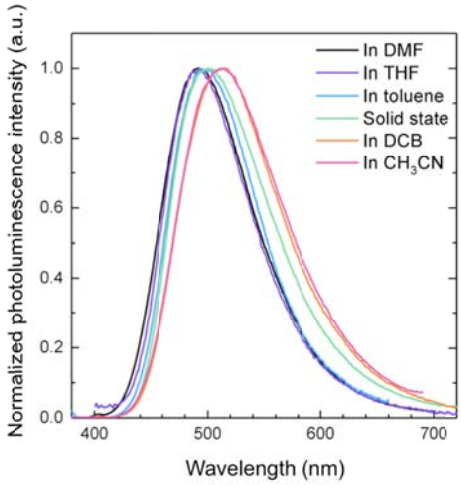

Figure 2-15. Emission spectra of **UiO-68-dpa** in DMF (black line), THF (blue line), toluene (blue line), DCB (*o*-dichlorobenzene; orange line), and CH_3CN (acetonitrile; red line) dispersion and solid state (green line).

2-6. Conclusion

I designed the new organic linker **H_2tpdc-dpa**, which shows blue thermally activated delayed fluorescence with the CIE coordinates of (0.16, 0.18) when doped in a PMMA film. Based on this linker, I developed the first MOF to exhibit TADF, the Zr-based MOF (**UiO-68-dpa**) emitting green TADF with a Φ of 30% under vacuum. Since this MOFs has good thermal stability and high responsivity to guest molecules such as gases and aromatic compounds encapsulated in the pores, this approach could open a new platform for bio-applications and photo-catalysts. Unlike conventional TADF emitters, the TADF characteristics can potentially be controlled by changing the metal ions or the three-dimensional structure of the MOF. Further development of thin-film MOFs deposited by layer-by-layer methods provides a path toward the realization of electroluminescent devices using TADF-emitting MOFs as the emitters.[18]

References

[1] H. Uoyama, K. Goushi, K. Shizu, H. Nomura and C. Adachi, *Nature*, 2012, **492**, 234–238.

[2] T. Li, D. Yang, L. Zhai, S. Wang, B. Zhao, N. Fu, L. Wang, Y. Tao and W. Huang, *Adv. Sci.*, 2017, **4**, 1600166.

[3] X. Xiong, F. Song, J. Wang, Y. Zhang, Y. Xue, L. Sun, N. Jiang, P. Gao, L. Tian and X. Peng, *J. Am. Chem. Soc.*, 2014, **136**, 9590–9597.

[4] H.-C. J. Zhou and S. Kitagawa, *Chem. Soc. Rev.*, 2014, **43**, 5415–5418.

[5] C. A. Bauer, T. V Timofeeva, T. B. Settersten, B. D. Patterson, V. H. Liu, B. A. Simmons and M. D. Allendorf, *J. Am. Chem. Soc.*, 2007, **129**, 7136–7144.

[6] Z. Wei, Z. Gu, R. K. Arvapally, Y. Chen, R. N. McDougald, J. F. Ivy, A. A. Yakovenko, D. Feng, M. A. Omary and H. Zhou, *J. Am. Chem. Soc.*, 2014, **136**, 8269–8276.

[7] H. Mieno, R. Kabe, N. Notsuka, M. D. Allendorf and C. Adachi, *Adv. Opt. Mater.*, 2016, **4**, 1015–1021.

[8] J. Yu, Y. Cui, H. Xu, Y. Yang, Z. Wang, B. Chen and G. Qian, *Nat. Commun.*, 2013, **4**, 2719.

[9] M. D. Allendorf, C. A. Bauer, R. K. Bhakta and R. J. T. Houk, *Chem. Soc. Rev.*, 2009, **38**, 1330–1352.

[10] P. Horcajada, R. Gref, T. Baati, P. K. Allan, G. Maurin, P. Couvreur, G. Férey, R. E. Morris and C. Serre, *Chem. Rev.*, 2012, **112**, 1232–1268.

[11] J. Della Rocca, D. Liu and W. Lin, *Acc. Chem. Res.*, 2011, **44**, 957–968.

[12] Y. Li, H. Xu, S. Ouyang and J. Ye, *Phys. Chem. Chem. Phys.*, 2016, **18**, 7563–7572.

[13] L. E. Kreno, K. Leong, O. K. Farha, M. Allendorf, R. P. Van Duyne and J. T. Hupp, *Chem. Rev.*, 2012, **112**, 1105–1125.

[14] A. Schaate, P. Roy, A. Godt, J. Lippke, F. Waltz, M. Wiebcke and P. Behrens, *Chem. Eur. J.*, 2011, **17**, 6643–6651.

[15] C.-H. Zhao, Y.-H. Zhao, H. Pan and G.-L. Fu, *Chem. Commun.*, 2011, **47**, 5518-5520.

[16] M. Gutiérrez Tovar, B. Cohen, F. Sánchez and A. Douhal, *Phys. Chem. Chem. Phys.*, 2016, **18**, 27761–27774.

[17] M. Gutiérrez, F. Sánchez and A. Douhal, *Phys. Chem. Chem. Phys.*, 2016, **18**, 5112–5120.

[18] O. Shekhah, H. Wang, D. Zacher, R. A. Fischer and C. Wöll, *Angew. Chem. Int. Ed.*, 2009, **48**, 5038.

Chapter 3

Long-lived room temperature phosphorescence of coronene in zeolitic imidazolate framework ZIF-8

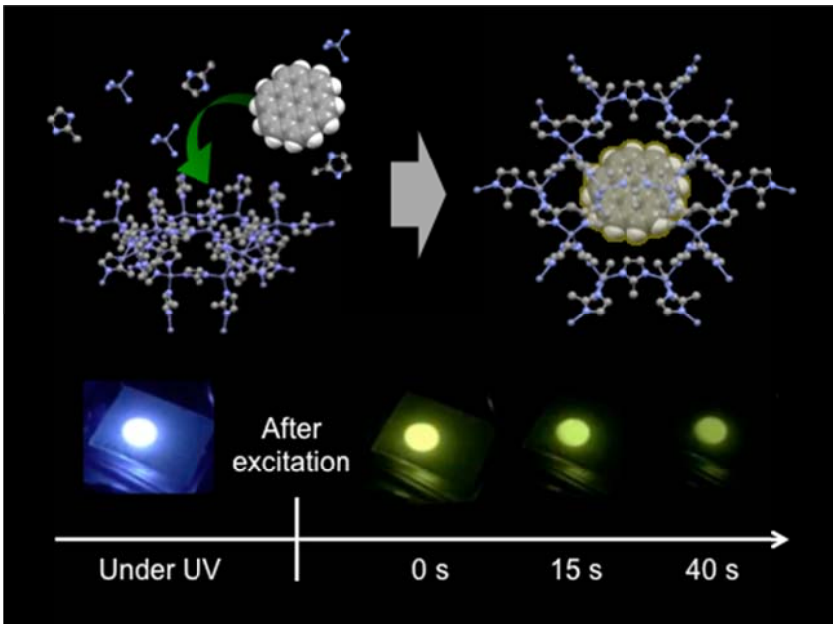

Hiroyuki Mieno, Ryota Kabe, Naoto Notsuka, Mark D. Allendorf, and Chihaya Adachi

Advanced Optical Materials, **2016**, *4*, 1015-1021.

3-1. Introduction

An ability to create long-lived triplet excitons in organic molecules could create new applications in optoelectronics such as photovoltaics,[1] OLEDs,[2] persistent luminescence,[3] reverse saturable absorption,[4] and high-resolution bioimaging.[5] Triplet excitons are generated indirectly by conversion from a short-lived singlet exciton via intersystem crossing or directly by recombination of electrically injected charge carriers.[6] However, triplet excitons are easily deactivated by nonradiative decay processes or phosphorescence. To realize long-lived triplet excitons (> 1 s), both the $k_{nr}(T)$ and k_p must be very small (< 1 s^{-1}). Consequently, long-lived excitons are typically found only in pure organic aromatic compounds that have small k_p. Nonradiative decay is highly accelerated by temperature; as a result, long-lived triplet excitons and related long-lived phosphorescence can normally be observed only at very low temperature such as 77 K. To realize long-lived phosphorescence at room temperature, the nonradiative decay processes derived from vibration and rotation of emitters and host molecules, energy transfer to other molecules (host matrices and oxygen), and TTA of emitters need to be suppressed by host matrices. For this purpose, a host matrix requires a higher triplet energy level than that of the guest emitter, along with a rigid structure and the ability to isolate guest emitter molecules. Several host matrices that can suppress nonradiative decay processes have been reported, such as cyclodextrin,[7] transparent and rigid plastic of PMMA,[8–10] and hydroxyl-steroid derivatives.[11] However, serious unsolved problems remain, particularly regarding thermal instability caused by phase transitions and thermal decomposition, which is an issue for all existing host matrices. Limited pore size is a problem for cyclodextrins, low solubility and dispersibility of guest emitters limits PMMA and hydroxyl-steroids, and aggregation of guest emitters over time is common.

Here, I propose MOFs as host materials to suppress nonradiative decay processes because of their rigid porous structure and pore structures that can trap and stabilize emitter molecules. MOFs are crystalline materials composed of metal ions and organic ligands and are attracting considerable interest because of their thermal and chemical stability and ability to encapsulate a wide variety of guest species in their cavities, including gases,[12–14] nanoparticles,[15–17] enzymes,[18,19] and organic molecules.[20–22] The individual pores of MOFs can isolate guest emitters and restrict molecular motion by their rigid frameworks. There are a few reports describing the suppression of molecular motion or concentration quenching in MOFs, such as the inhibition of *cis-trans* isomerization of stilbene,[23] amplification of fluorescence quantum yield,[24] and demonstration of a two-photon pumped laser.[25] However, these are not realizing long-lived organic triplet excitons and related phosphorescence of guest molecules. Although a number of phosphorescent MOFs are known, most of these emit only at low temperatures (77 K), indicating that nonradiative deactivation is dominant at room temperature.[26,27] In contrast, in all of the MOFs that exhibit room-temperature phosphorescence the well-known heavy-atom effect is used. Heavy atoms such as I, Br, Pb and Ir[28–33] incorporated in the structure of the framework itself or encapsulated within the pores enhance the rate of radiative decay from the triplet state k_p, rather than reducing the rate of nonradiative deactivation $k_{nr}(T)$. As a result, the phosphorescence lifetime of these MOFs is quite short (10^{-3} s ~ 10^{-6} s), significantly less than the lifetime desired for many applications. Moreover, since the origin of the photoluminescence is not a pure guest emitter but a metal-coordinated ligand or an exciplex between ligand and guest molecule, careful design of both the linker and MOF is necessary to achieve efficient room-temperature phosphorescence.

In this work, I demonstrate that long-lived emission from triplet excitons can be

achieved even at high temperature by encapsulating organic emitter in MOFs. In addition, I show that TADF[34] can be achieved from MOF-encapsulated emitters at temperatures >300 K. TADF is an efficient process to harvest triplet excitons for light emission especially in OLEDs; however, it requires careful molecular design of the emitter to enable thermal up-conversion from triplet exciton to singlet exciton. Our method realizes TADF from common aromatic molecules without any chemical modification. As proof of concept I used the well-known long-lived phosphorescent emitters coronene ($k_p \sim 0.1\ s^{-1}$)[8] and its deuterated analog (coronene-d_{12}; $k_p \sim 0.05\ s^{-1}$) as guests because their triplet emission is highly sensitive to the competitive nonradiative decay constant $k_{nr}(T)$. As a result, these molecules emit phosphoresce only in frozen solution at low temperatures. Moreover, coronene has a planar structure that easily aggregates in other common host matrices, leading to a broad excimer emission at longer wavelength that is unfavourable to light-emitting applications. The thermally and chemically stable zeolitic imidazolate framework ZIF-8[35] was selected as the host. This MOF, which consists of Zn ions linked by imidazole ligands, was selected as the host matrix because its pore diameter (1.16 nm) corresponds to the molecular size of coronene (1.17 nm) taking into account its van der Walls radius. I also expected that the small pore windows of ZIF-8 (0.34 nm) would securely hold guest coronene molecules within its cavities (Fig. 3-1). The encapsulation of guest molecules into ZIF-8 pores has been reported on the several size of guests such as caffeine,[36] fluorescein[37] and porphyrin.[38] In the case of fluorescein and porphyrin, the guest molecules were not released because their molecular sizes are much larger than the pore window size.

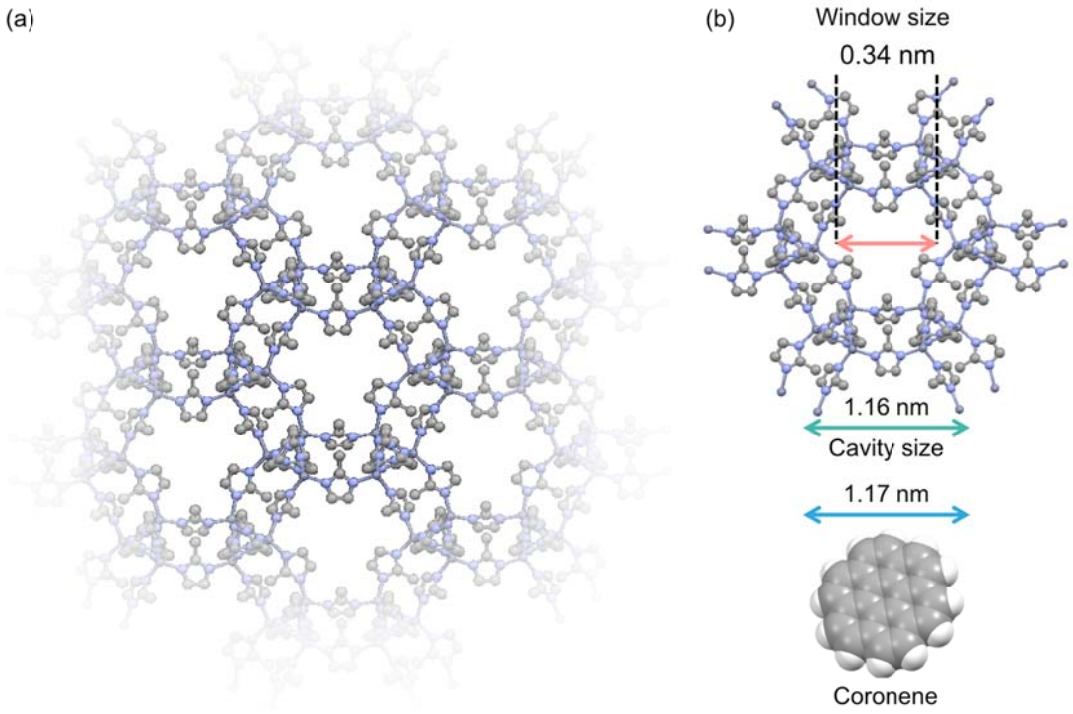

Figure 3-1. (a) Single crystal structure of ZIF-8. (b) The window and cavity size of ZIF-8 and the molecular size of coronene taking into account its van der Walls radius.

3-2. Experimental

3-2-1. Synthesis

Coronene-h_{12} and coronene-d_{12} were obtained from Wako Chemicals Inc. (Tokyo, Japan) and Cambridge Isotope Laboratories Inc. (Tewksbury, USA), respectively, and purified by sublimation before use. ZIF-8 was synthesized following a literature procedure.[32] A DMF of 45 mL solution of coronene-h_{12} (19 mg, 6.28×10^{-5} mol) or coronene-d_{12} (15 mg, 6.28×10^{-5} mol), $Zn(NO_3)_2 \cdot 6H_2O$ (597 mg, 2.01×10^{-3} mol) and 2-methylimidazole (**HMeIM**) (150 mg, 1.83×10^{-3} mol) was heated at a rate of 5 °C/min to 140 °C in a programmable oven, held at 140 °C for 24 h and then cooled to room temperature at a rate of 0.4 °C/min. The resulting polyhedral crystals were filtrated, washed with chloroform and DMF, and soaked in methanol for 2 days. Then **coronene-h_{12}@ZIF-8** and **coronene-d_{12}@ZIF-8** were washed with PVP in methanol (14 wt%) to remove coronene adsorbed on the surface of the crystals. Even after these washing processes, coronene molecules still remained in ZIF-8, indicating coronene molecules were encapsulated within the ZIF-8 pores and were not able to be released because the aperture size of ZIF-8 (0.34 nm) is much smaller than coronene size (11.7 nm). The loading efficiency of coronene was adjustable by controlling the initial amount of coronene; however, loading efficiency was low because of the aggregation of coronene at high concentrations. The products were characterized by XRD, FT-IR spectroscopy, BET surface area analysis and elemental analysis.

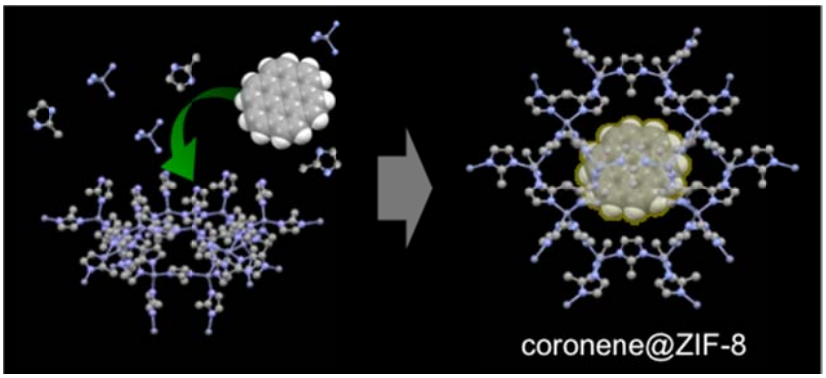

Figure 3-2. Schematic structure of **coronene@ZIF-8** synthesis

Elemental analysis:

ZIF-8 (H; 4.36, C; 42.12, N; 24.49)

coronene@ZIF-8 (H; 4.31, C; 42.93, N; 24.12)

FT-IR: ZIF-8 (KBr 4000–400 cm^{-1}): 3449(w), 3133(w), 3009(w), 2928(m), 2857(w), 2765(w), 2486(w), 2453(w), 1686(s), 1584(w), 1458(s), 1424(s), 1383(m), 1310(s), 1258(w), 1180(m), 1146(s), 1089(m), 996(w), 953(w), 756(s), 693(m), 665(m), 422(s).

Coronene-h_{12} (KBr 4000–400 cm^{-1}): 3449(w), 3047(v), 3018(v), 2919(w), 2850(w), 1313(s), 1134(w), 957(w), 848(s), 810(w), 768(w), 543(s).

Coronene-d_{12} (KBr 4000–400 cm^{-1}): 2270(w), 2251(w), 1269(s), 1088(w), 949(w), 736(s), 624(w), 482(s).

Coronene-h_{12}@ZIF-8 (KBr 4000–400 cm^{-1}): 3449(w), 3132(w), 3058(w), 3010 (w), 2928(m), 2857(w), 2765(w), 2486(w), 2453(w), 1684(s), 1585(w), 1458(s), 1424(s), 1382(m), 1310(s), 1257(w), 1180(m), 1146(s), 1090(m), 996(w), 953(w), 855(w), 828(w), 756(s), 693(m), 666(m), 422(s).

Coronene-d_{12}@ZIF-8 (KBr 4000–400 cm^{-1}): 3447(w), 3132(w), 2928(m), 2856(w), 2765(w), 2485(w), 2452(w), 1684(s), 1589(w), 1457(s), 1424(s), 1385(m), 1309(s), 1257(w), 1179(m), 1145(s), 1089(m), 996(w), 953(w), 864(w), 760(s), 693(m), 657(m), 421(s).

3-2-2. Film preparation

Coronene-h_{12}@ZIF-8 and **coronene-d_{12}@ZIF-8** films were fabricated for the optical measurements. Films were formed on indium tin oxide (ITO)-coated glass substrates functionalized with 3-aminopropyltrimethoxysilane (**3-APTMS**) by immersing the substrate in the reaction solution. A PMMA film containing coronene was fabricated on an ITO substrate by spin coating a solution of DMF containing coronene-h_{12} (0.6%) and PMMA (10%) at 1000 rpm for 60 s at room temperature.

3-2-3. Equipment

XRD patterns were obtained using a Rigaku Ultima IV diffractometer with CuKα radiation. TGA data were measured with a rate 10 °C/min using a Bruker TG-DTA2400SA analyzer. ^{1}H NMR spectra were recorded on a Bruker AVANCE III 500 MHz spectrometer. **Coronene-h_{12}@ZIF-8** (10 mg) was dissolved in DMSO-d_6 (5 mL) containing HCl (100 □L) to form a clear solution. Elemental analyses (C, H, N) were carried out using a Yanaco MT-5 CHN corder. IR spectra were recorded on a JASCO FT/IR-6100 spectrometer.

3-2-4. Diffuse reflectance UV-*vis* measurements

Diffuse reflectance UV-vis spectra of ZIF-8 and **coronene-h_{12}@ZIF-8** were recorded on a Cary 5000 spectrophotometer equipped with a reflectance sphere. The Kubelka-Munk conversion, F(R) *vs.* wavenumber, of the raw diffuse reflectance spectrum (R *vs.* wavenumber) was obtained by applying the formula:

$$F(R) = (1-R)^2 / 2R$$

3-2-5. Photoluminescence measurements of coronene-h_{12}@ZIF-8 and d_{12}@ZIF-8 and PMMA-doped films

The Φ_{total} (RT) of **coronene-h_{12}@ZIF-8** and **coronene-d_{12}@ZIF-8** were measured with a Hamamatsu Photonics absolute photoluminescence quantum yield spectrometer C11347 (Quantaurus-QY) at room temperature under a vacuum (10^{-3} Pa) generated by an Edwards T-station turbo molecular pump. The temperature dependence of time-resolved photoluminescence spectra were recorded on a Hamamatsu Photonics multichannel analyzer (PMA-12) under a vacuum (>10^{-3} Pa) generated by an Edwards T-station turbo molecular pump. Sample temperatures were controlled using a cryostat (Oxford Ltd. Optistat DN-2 and Sumitomo Heavy Industries, Ltd. Opticool). Samples were excited at 380 nm by a Xe lamp coupled with a monochromator (Fig. 3-3). Here, the Φ_{flu} (RT) and Φ_{delay} (RT) were calculated from the emission intensity at all wavelength obtained by the PMA-12. [8] The total emission intensity {I_{total} (RT)} of fluorescence {I_{flu} (RT)} and delayed emission {I_{delay} (RT)} at RT were measured by integrating the emission intensity for 40 ms under continuous photo excitation. The delayed emission intensity {I_{delay} (RT)} was measured from the accumulation of emission intensity for 40 ms after stopping the photo excitation since the I_{delay} does not change in the first 40 ms because of very long delayed emission.

$$\Phi_{total}\,(\mathrm{RT}) = \Phi_{flu}\,(\mathrm{RT}) + \Phi_{delay}\,(\mathrm{RT}) \quad (1)$$

$$\Phi_{delay}\,(\mathrm{RT}) = \{(I_{delay}\,(\mathrm{RT}) / I_{total}\,(\mathrm{RT}))\ \Phi_{total}\,(\mathrm{RT}) \quad (2)$$

The Φ_{delay} (RT) consists of Φ_{phos} (RT) and Φ_{TADF} (RT); however, it was difficult to separate them. Therefore, I presume the integrated emission intensity between 400-510 nm is TADF and 510-700 nm is phosphorescence, respectively. The Φ_{delay} (T) at each temperature was calculated from the integrated emission intensity obtained by the PMA-12.

$$\Phi_{delay}\,(RT) = \Phi_{phos}\,(RT) + \Phi_{TADF}\,(RT) \quad (3)$$

$$\Phi_{delay}\,(T) = \{I_{delay}\,(T) / I_{delay}\,(RT)\}\ \Phi_{delay}\,(RT) \quad (4)$$

$$\Phi_{total}\,(T) = \Phi_{flu}\,(T) + \Phi_{phos}\,(T) + \Phi_{TADF}\,(T) \quad (5)$$

The τ_{flu} of samples were measured with a Hamamatsu Photonics compact fluorescence lifetime spectrometer C11367 (Quantaurus-Tau) under air to omit the TADF process. The τ_{phos} of samples were measured with a Hamamatsu Photonics multichannel analyzer (PMA-12) under vacuum (>10^{-3} Pa).

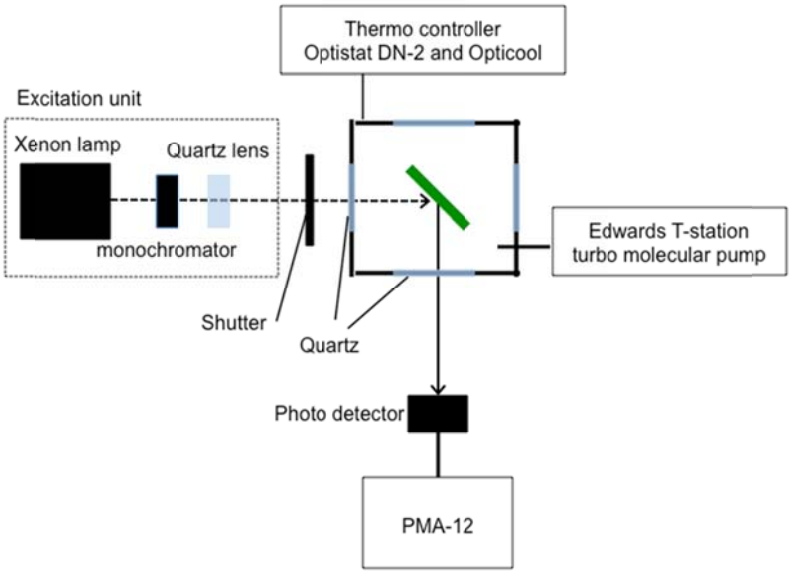

Figure 3-3. Schematic image of photoluminescence measurement system.

3-2-6. Determination of k_p and k_{nr}(T)

The total values of $k_{nr}(T)$ at each temperature was calculated using $k_{nr}(T) = 1/\tau\,(T) - k_p$. Because the nonradiative decay of guest molecules at 5 K is presumed to be 0 (k_{nr}(5 K) = 0), k_p was calculated using $k_p = 1/\tau$ (5 K).

3-2-7. Doping content of coronene in ZIF-8

The luminescent intensities of different concentrations of coronene in DMF solution

were measured to determine the relationship between the intensity of luminescence and concentration of coronene in DMF solution. **Coronene-h_{12}@ZIF-8** or **coronene-d_{12}@ZIF-8** (25 mg) was dissolved in DMF (5 mL) containing HCl (30–50 □L, 12 mol/L) to form a clear solution, which was then diluted 100-fold with DMF. The luminescent intensity of each solution was measured, and the concentrations of coronene-h_{12} and coronene-d_{12} were calculated using Equation 3-6 and 3-7, respectively.

$$y_1 = 2.18823 \times 10^6 x_1 + 192542 \quad (3\text{-}6)$$

$$y_2 = 2.49285 \times 10^6 x_2 + 419232 \quad (3\text{-}7)$$

Here, y is the luminescent intensity, and x is concentration. The contents of coronene-h_{12} and coronene-d_{12} in ZIF-8 were calculated to be 1.46 wt% and 1.03 wt%, respectively.

3-2-8. BET surface are analysis

50 mg of ZIF-8 or **coronene@ZIF-8** were loaded into a pre-weighed glass sample cells and degassed at ambient temperature for 5 h, then, evacuated at 300 °C for 2 h on the Quantachrome MasterPrep degasser at the specified temperature and time. Typical ending pressure after degassing is around 0.004 Torr. Once degassed the samples are purged with nitrogen and weighed again. The difference between this weight and the empty cell weight gives us the degassed sample weight. The cell is the placed on the Quantachrome Quadrasorb SI micropore porosimeter for surface area analysis. The weight of the sample is input into the starting program and used by the program when determining the surface area. BET surface area (m^2/g) measurements were collected at 77 K by N_2 (67 adsorption points from 0.005 to 0.99 P/Po and 46 desorption points from 0.99 to 0.005 P/Po)

3-3. Characterization

As coronene is too large to pass through the ZIF-8 pore windows, I incorporated the coronene-h_{12} and coronene-d_{12} emitters into the cavities of ZIF-8 during the synthesis of the framework according to the fabrication method of fluorescein encapsulated ZIF-8.

To confirm the encapsulation of coronene inside ZIF-8 pores, **coronene@ZIF-8** samples were analyzed by several methods. Powder XRD reveals that the ZIF-8 structure is unaffected by the incorporation of coronene (Fig. 3-4a). Thermogravimetric analysis indicates that these molecules are securely contained by the MOF; a comparison between **coronene@ZIF-8** and ZIF-8 itself indicates no substantial weight loss originated from coronene at temperatures above 180 °C, even though coronene sublimes at 180 °C (Fig. 3-4b). The FT-IR spectrum of **coronene-h_{12}@ZIF-8** exhibits peaks at 3058 and 855 cm^{-1} corresponding to vibrations of coronene-h_{12} (Figs. 3-4c and d). Furthermore, I quantified the amount of **coronene@ZIF-8** adsorbed within the crystals by dissolving them in acidic DMF solution and measuring their photoluminescence intensity. The concentration of coronene determined from the fluorescence intensity–concentration relationship (Fig. 3-5) of was 1.46 wt%, from which I obtain a loading efficiency of coronene-h_{12} into ZIF-8 pores of 0.067 coronene molecules per pore. The concentration of coronene is adjustable by varying the amount of coronene used in the solvothermal synthesis. However, the excimer of coronene was partially formed when the solution concentration exceeded 6.25 mol% because the phosphorescence spectrum became broader and red-shifted (Fig. 3-6). The presence of encapsulated coronene-h_{12} was also confirmed by ^{1}H NMR (Fig. 3-7). Finally, the BET surface area decreases to 1182 m^2/g in **coronene-h_{12}@ZIF-8** from 1954 m^2/g for ZIF-8 itself (Fig. 3-8). Together, these results indicate that coronene is encapsulated in the pores and not

simply adsorbed on the surface of the ZIF-8 crystals.

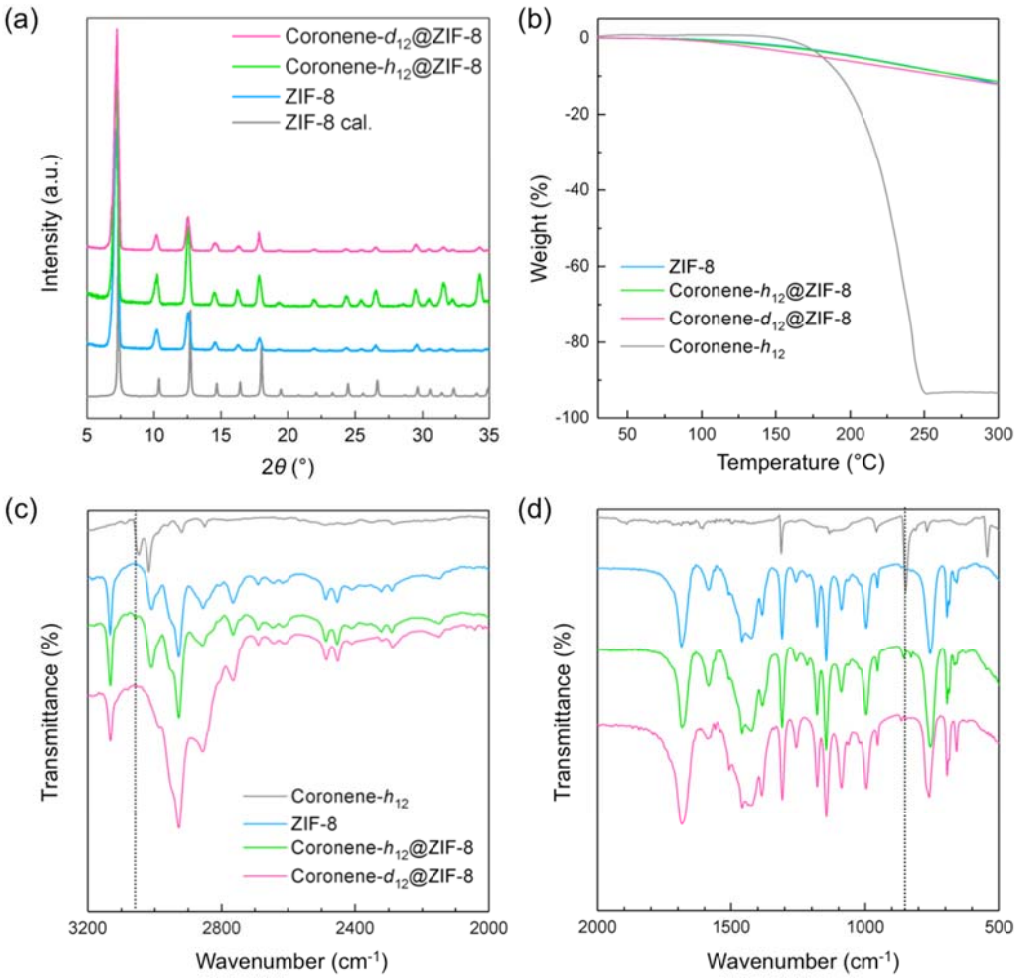

Figure 3-4. (a) XRD patterns of ZIF-8 calculation, ZIF-8, **coronene-h_{12}@ZIF-8**, and **coronene-d_{12}@ZIF-8**. (b) TGA data (The data for coronene-h_{12} measured under 1 Pa indicates that coronene-h_{12} is sublimed over 350 K (180 °C). Other data were measured under 1 atm.), (c) FT-IR (3200–2000 cm^{-1}) spectra, and (d) FT-IR (2000–500 cm^{-1}) spectra of coronene-h_{12}, ZIF-8, **coronene-h_{12}@ZIF-8**, and **coronene-d_{12}@ZIF-8**.

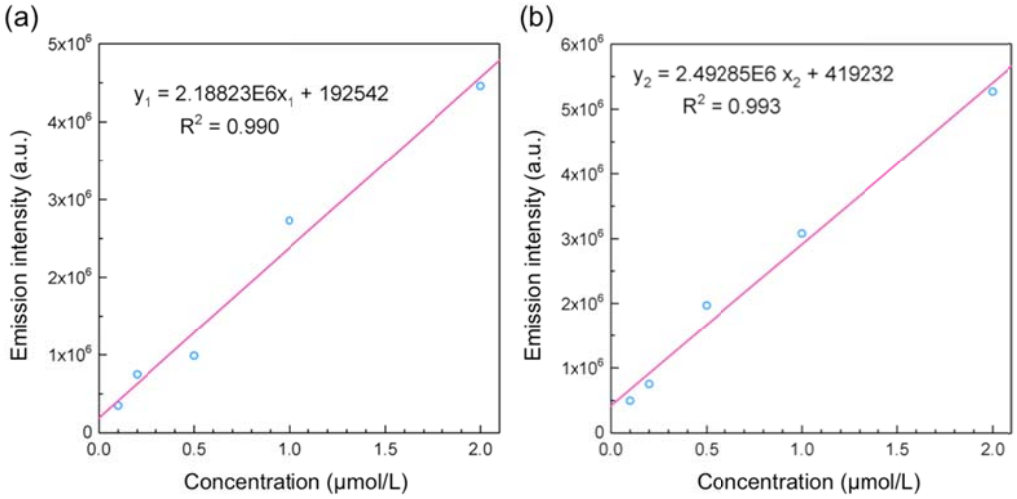

Figure 3-5. Intensity-concentration diagrams and the fitted curves for DMF solutions of (a) coronene-h_{12} and (b) coronene-d_{12}.

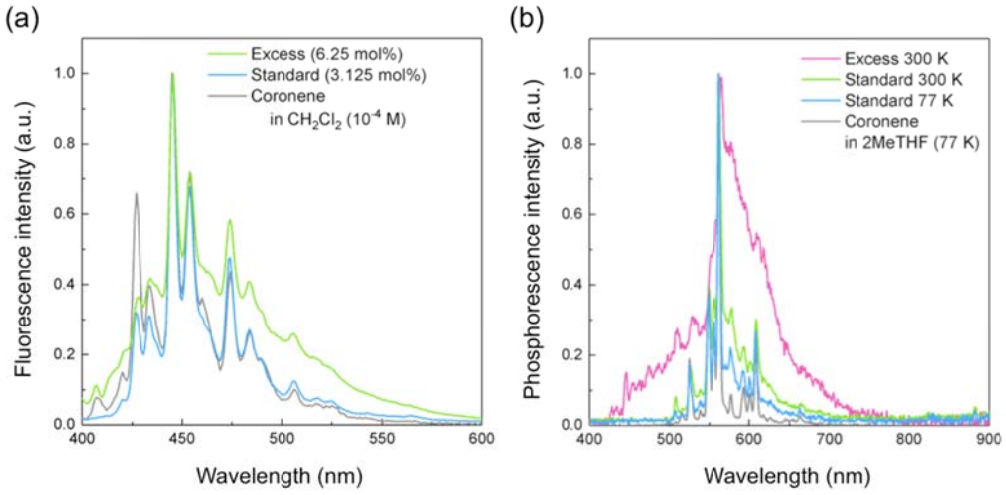

Figure 3-6. (a) Fluorescence and (b) phosphorescence spectra of **coronene-h_{12}@ZIF-8** at different amount of coronene-h_{12} used in the solvothermal synthesis (6.25 or 3.125 mol%) and coronene-h_{12} in CH_2Cl_2 (fluorescence) and **2MeTHF** (phosphorescence at 77 K).

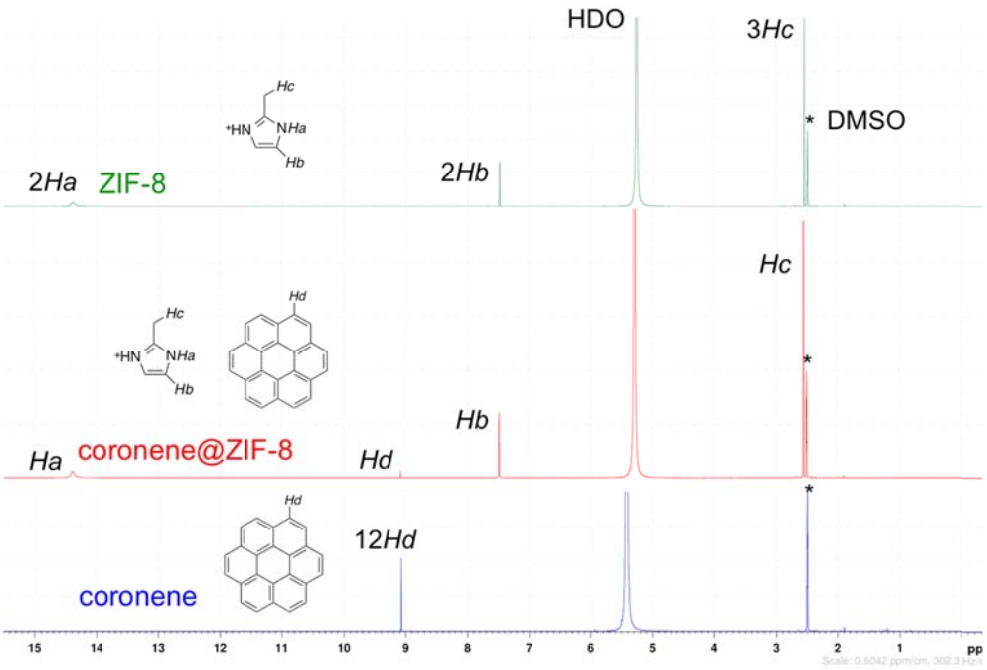

Figure 3-7. ^{1}H NMR spectra of ZIF-8, coronene-h_{12}, and **coronene-h_{12}@ZIF-8** in HCl contained DMSO-d_6.

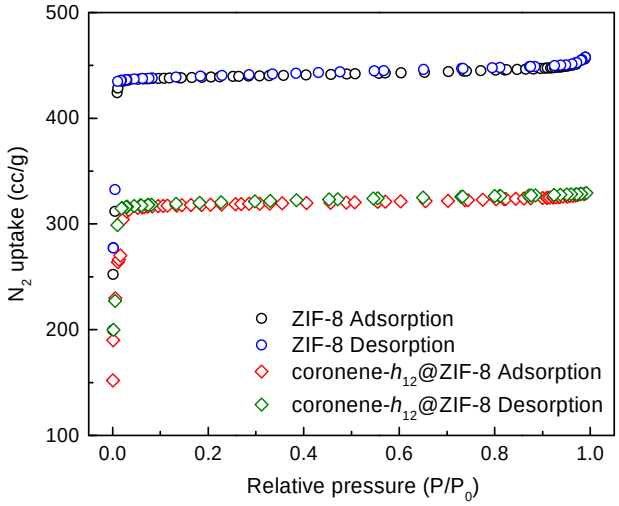

Figure 3-8. Nitrogen adsorption isotherms at 77K of ZIF-8 (black and blue circles) and **coronene-h_{12}@ZIF-8** (red and green circles).

3-4. Results and discussion

3-4-1. Photophysical properties of coronene@ZIF-8

Coronene@ZIF-8 exhibits both fluorescence and long-lived phosphorescence at room temperature. The phosphorescence lifetime (τ_{phos}) of **coronene-*h*$_{12}$@ZIF-8** at 300 K (7.4 s) is similar to that at 5 K (8.8 s). **Coronene-*d*$_{12}$@ZIF-8** exhibits an even longer τ_{phos} (22.4 s) at 300 K because the vibrational energy of the C-D stretching mode is lower than that of the C-H stretching mode.[39] This long-lived phosphorescence results from the reduced nonradiative decay rate of the guest emitter, without any charge-transfer interaction with host which causes absorption and emission shifting.[40–42] To determine whether there is a charge-transfer interaction between ZIF-8 and guest molecule coronene-h_{12}, the optical properties of ZIF-8 and **coronene-*h*$_{12}$@ZIF-8** were characterized by diffuse reflectance UV-vis, excitation and emission spectroscopy (Fig. 3-9). **Coronene-*h*$_{12}$@ZIF-8** crystal exhibits blue fluorescence that originates from coronene-h_{12} under ultraviolet (UV) light irradiation and green long-lived emission after UV irradiation was turned off. The UV-vis spectrum of **coronene-*h*$_{12}$@ZIF-8** shows absorption up to 450 nm with four peaks at 300, 335, 379 and 403 nm attributable to the □-band (302 nm), *p*-band (339 nm), and □-band (384 and 409 nm) absorption from coronene-h_{12} (Fig. 3-9a).[43] Vibronic peaks of the *p*-band (341 nm) and □-band (375 - 410 nm) clearly observed in the excitation spectrum of **coronene-*h*$_{12}$@ZIF-8** confirm that absorption of coronene-h_{12} is unchanged within ZIF-8 pores. These absorption and excitation spectra indicate that there is no strong interaction between coronene-h_{12} and Zn ions or 2-methyl imidazole in the ground state. The fluorescent decay profiles (τ_{flu}) of **coronene-*h*$_{12}$@ZIF-8**, ZIF-8 and coronene-h_{12} dissolved in $CHCl_3$ also indicate the lack of charge transfer interactions. To avoid the effect of delayed emission, τ_{flu}

were obtained under air (Fig. 3-10). **Coronene-h_{12}@ZIF-8** exhibits second exponential decay with prompt (25 ns) and delayed (188 ns) components. The prompt component is in good agreement with coronene-h_{12} dissolved in $CHCl_3$ (25 ns). Moreover, the delayed component is comparable to the ZIF-8 (103 ns). These results indicate the host matrix ZIF-8 absorbs the excitation light, and then Förster energy transfer to guest coronene occurs like common host-guest systems without charge transfer interactions.

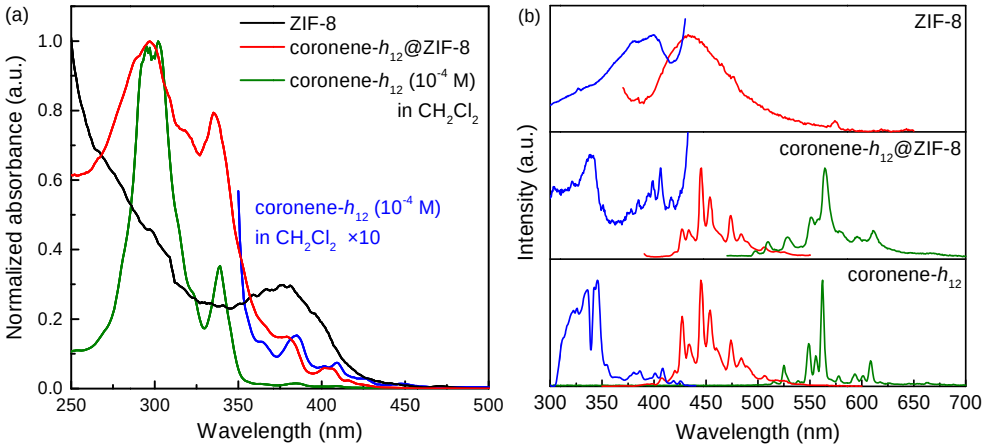

Figure 3-9. (a) Diffuse reflectance UV-*vis* spectra (ZIF-8: black line, **coronene-h_{12}@ZIF-8**: red line) and UV-*vis* absorption spectrum (coronene-h_{12} in CH_2Cl_2: green and blue line) (b) Excitation (443 nm, blue line), fluorescence (350 nm, red line) and phosphorescence (green line) spectra of ZIF-8 (top), **coronene-h_{12}@ZIF-8** (middle) and coronene-h_{12} in CH_2Cl_2 (bottom).

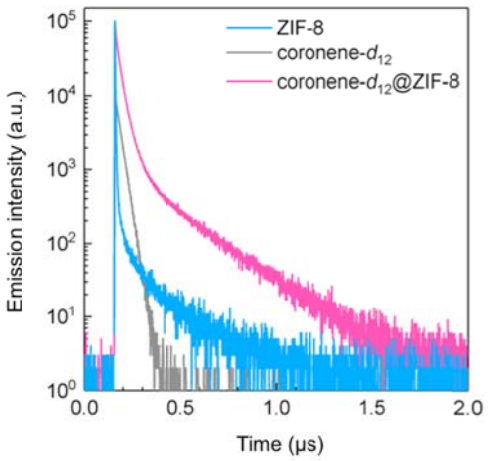

Figure 3-10. Fluorescence decay profiles of **coronene-h_{12}@ZIF-8** (red), ZIF-8 (green), and coronene-h_{12} in $CHCl_3$.

Not only are the coronene molecules isolated from one another by the MOF pore geometry, their motion is restricted by the close similarity of the pore diameter and size of coronene. This complete isolation and restriction of coronene without charge transfer interaction dramatically decreases the molecular vibration of coronene, enabling the room-temperature phosphorescence. The fluorescence and phosphorescence spectra of **coronene-h_{12}@ZIF-8** and **coronene-d_{12}@ZIF-8** were obtained under vacuum (>10^{-3} Pa) because ZIF-8 has a high affinity for oxygen,[44] which acts as a triplet quencher. The fluorescence peaks of the **coronene-h_{12}@ZIF-8** are located at 427, 433, 445, 453, 474, 483 and 506 nm, and the phosphorescence peaks are located at 509, 529, 551, 558, 564, 577, 595 and 610 nm (Fig. 3-9b). The fluorescence spectrum was consistent with the π-π* transitions of coronene-h_{12}.[45] Although solid-state coronene readily forms an excimer that exhibits a broad emission centered at 498 nm,[46] the fluorescence spectrum of **coronene-h_{12}@ZIF-8** is identical to that of coronene-h_{12} in dilute CH_2Cl_2 solution (10^{-4} M), confirming that the coronene-h_{12} molecules are isolated in ZIF-8. In contrast, the phosphorescence spectrum is broader than that of coronene-h_{12} dispersed in a frozen 2-methyltetrahydrofuran (**2MeTHF**) matrix at 77 K because of the presence of delayed fluorescence as well as lower signal/noise ratio and higher measurement temperature. The intensity of the delayed emission between 500 nm and 550 nm is increased by the contribution of delayed fluorescence of coronene-h_{12} at 300 K. The phosphorescence / fluorescence intensity ratio of **coronene-h_{12}@ZIF-8** at 300 K is ~10 times weaker than that of CH_2Cl_2 solution of coronene-h_{12} at 77 K. A sharp phosphorescence spectrum for **coronene-h_{12}@ZIF-8** could be obtained at 77 K (Fig. 3-11).

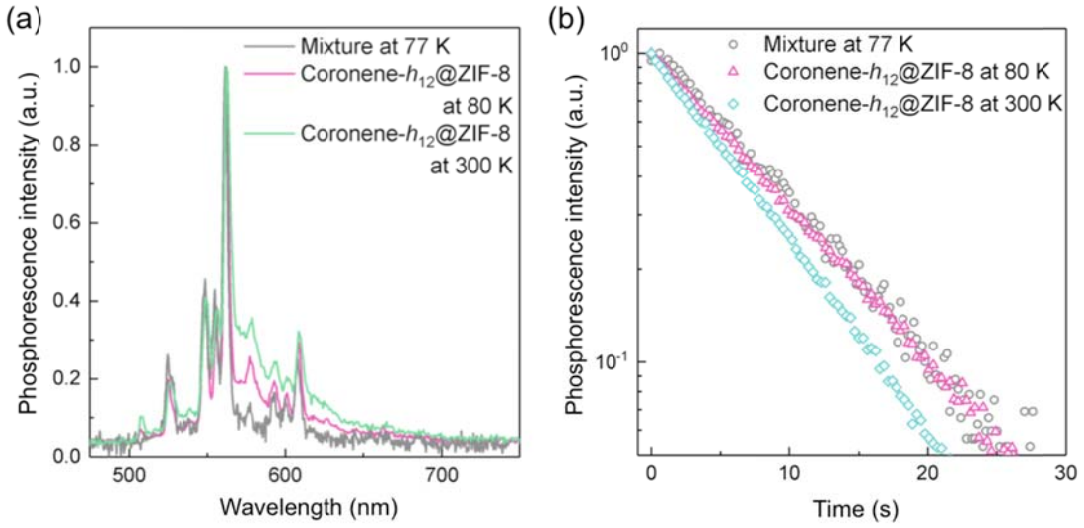

Figure 3-11. Phosphorescence spectra (a) and emission decay profiles (b) of mixture of **HMeIm** and coronene-h_{12} in DMF solution at 77 K (black line), **coronene-h_{12}@ZIF-8** at 300 K (green line) and 80 K (red line).

3-4-2. Long-lived triplet excitons of coronene@ZIF-8

I confirmed the suppression of nonradiative deactivation of coronene in the ZIF-8 framework by measuring τ_{phos} of a **coronene@ZIF-8** film and a PMMA film doped with 0.6 wt% coronene at 5–460 K. PMMA was used as a reference host because this material is known to allow room-temperature phosphorescence from aromatic guest emitters when used as a host.[8] These data, along with the photoluminescence quantum yield (Φ_{total}), calculated fluorescence and delayed emission quantum yields (Φ_{flu} and Φ_{delay}, respectively), k_p, and the nonradiative decay constant (k_{nr}(T)) obtained for the films, are summarized in Table 3-1. **Coronene-h_{12}@ZIF-8** and PMMA-doped films exhibit almost the same τ_{phos} at 5 K (8.83 s and 8.30 s, respectively), consistent with the lack of nonradiative deactivation. In contrast, τ_{phos} at 300 K of **coronene-h_{12}@ZIF-8** (7.42 ± 0.01 s) is longer than that of the PMMA-doped film (5.58 ± 0.23 s) (Fig. 3-12a). Moreover, phosphorescence from the PMMA-doped film

was not observed above 320 K. It is known that when PMMA is used as the matrix, the β-relaxation of the side chain increases above 240 K and the α'-relaxation of the main CH_2 chain is dominant above 300 K,[47,48] which cause $k_{nr}(T)$ to increase to 0.058 s^{-1} (Figs. 3-12b, 3-13, and Table 3-2). Although τ_{phos} of **coronene-*h*$_{12}$@ZIF-8** gradually decreased above 300 K, because of the thermal activation from long-lived triplet excitons to short-lived singlet excitons, it still exhibits long-lived emission (τ_{phos} = 0.4 s) even at 460 K. This result is in good agreement with the TGA data indicating that the coronene molecules are encapsulated in the pores of ZIF-8.

In addition to these favourable luminescence properties of **coronene@ZIF-8**, I identified several other advantages of using this MOF as a host material. Notably, high loadings of guest molecules can be achieved without aggregation. Coronene loadings as high as 1.46 wt% were achieved in **coronene@ZIF-8**, without excimer emission, indicating that the encapsulated coronene molecules are not able to aggregate in the individual pores of ZIF-8. In contrast, because coronene tends to aggregate during spin coating, I could not obtain a coronene loading in a PMMA film higher than 0.6 wt% without forming aggregates. A second advantage of ZIF-8 over other host matrices such as PMMA is its high stability in air; **coronene@ZIF-8** exhibits no change in its photophysical properties after one month of air exposure.

At temperatures exceeding 300 K, the colour of the **coronene@ZIF-8** long-lived emission changes from yellow to blue, which occurs because the long-lived triplet excitons are thermally activated to singlet excitons that exhibit delayed fluorescence (Fig. 3-14). The delayed fluorescent lifetime ($\tau_{delayed}$) is almost equivalent to τ_{phos} (Fig. 3-15a) and its emission intensity increases linearly with increasing excitation power (Fig. 3-15b). These results

clearly indicate that the origin of this delayed fluorescence is not a triplet-triplet annihilation process, but TADF. Moreover, the total delayed emission quantum yield (Φ_{delay}) of TADF (Φ_{TADF}) and phosphorescence (Φ_{Phos}) increases with increasing temperature up to 420 K because of the efficient up-conversion of long-lived triplet to short-lived singlet excited state. Although TADF molecules can be designed to minimize the singlet and triplet energy gap, our approach in which nonradiative decay from the triplet state is suppressed, realizes TADF from a common aromatic molecule coronene, avoiding potentially complex synthesis.

Table 3-1. Photophysical properties of **coronene-h_{12}@ZIF-8**, **coronene-d_{12}@ZIF-8**, and coronene-h_{12} doped into PMMA at room temperature.

Sample	Φ_{total} (%)	Φ_{flu} (%)	Φ_{delay} (%)	τ_{phos} (s)	k_p (s^{-1})	k_{nr} (s^{-1})
Coronene-h_{12}@ZIF-8	10.5 ± 0.1	8.7 ± 0.1	1.8 ± 0.1	7.42 ± 0.01	0.11	0.022 ± 0.001
Coronene-d_{12}@ZIF-8	13.8 ± 0.1	10.1 ± 0.1	3.7 ± 0.1	22.4 ± 0.05	0.040	0.0095 ± 0.0001
Coronene-h_{12} in PMMA	12.3 ± 0.1	10.6 ± 0.1	1.7 ± 0.1	5.58 ± 0.23	0.12	0.058 ± 0.007

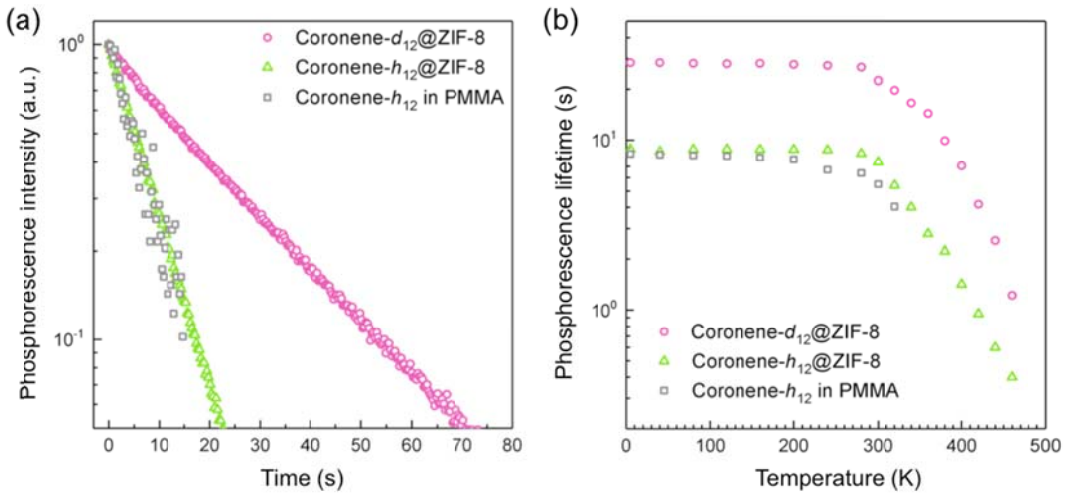

Figure 3-12. (a) Phosphorescence decay profiles of coronene-h_{12} doped into PMMA (black circles), **coronene-h_{12}@ZIF-8** (red circles), and **coronene-d_{12}@ZIF-8** (green circles) at room temperature. (b) Temperature dependence of τ_{phos} of coronene-h_{12} doped into PMMA (black circles), **coronene-h_{12}@ZIF-8** (red circles), and **coronene-d_{12}@ZIF-8** (green circles). Complete disappearance of phosphorescence from coronene-h_{12} in the PMMA host matrix was observed at temperatures higher than 320 K.

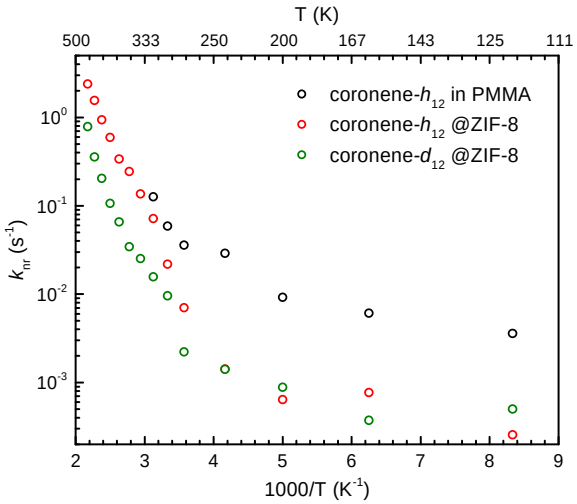

Figure 3-13. Temperature dependence of k_{nr}(T) of coronene-h_{12} in PMMA (black), **coronene-h_{12}@ZIF-8** (red), and **coronene-d_{12}@ZIF-8** (green).

Table 3-2. Temperature dependence of Φ_{delay}, Φ_{phos}, and Φ_{TADF} of **coronene-d_{12}@ZIF-8.**

	300 K	320 K	340 K	360 K	380 K	400 K	420 K	440 K	460 K
Φ_{delay} (%)	3.70	4.29	4.95	5.30	5.74	5.94	6.45	5.17	4.55
Φ_{TADF} (%)	0.42	0.63	1.04	1.62	2.57	3.25	4.09	3.77	3.60
Φ_{phos} (%)	3.28	3.66	3.91	3.68	3.17	2.69	2.36	1.40	0.95

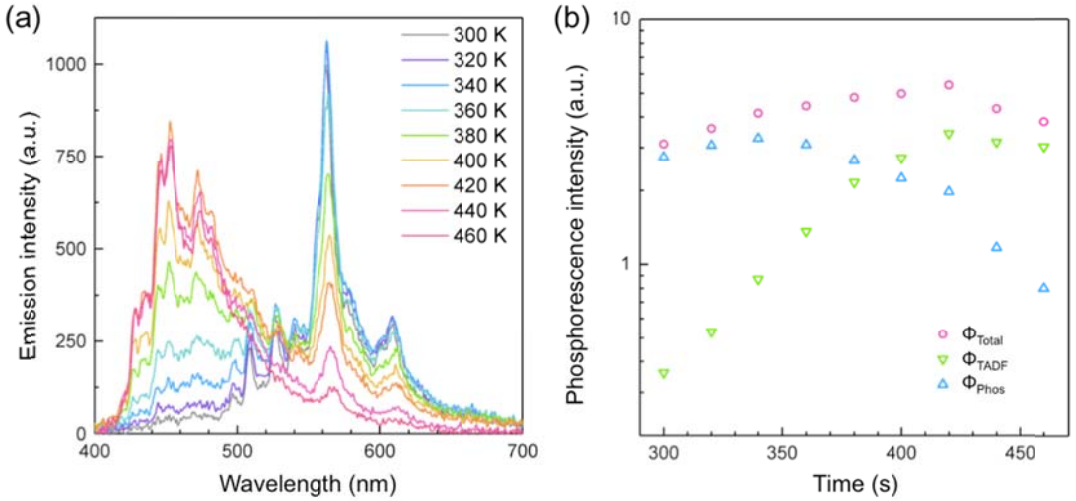

Figure 3-14. (a) Temperature dependence of photoluminescence spectra of **coronene-d_{12}@ZIF-8**. (b) Temperature dependence of emission quantum yields (Φ_{delay}, Φ_{TADF}, and Φ_{phos}) of **coronene-d_{12}@ZIF-8**.

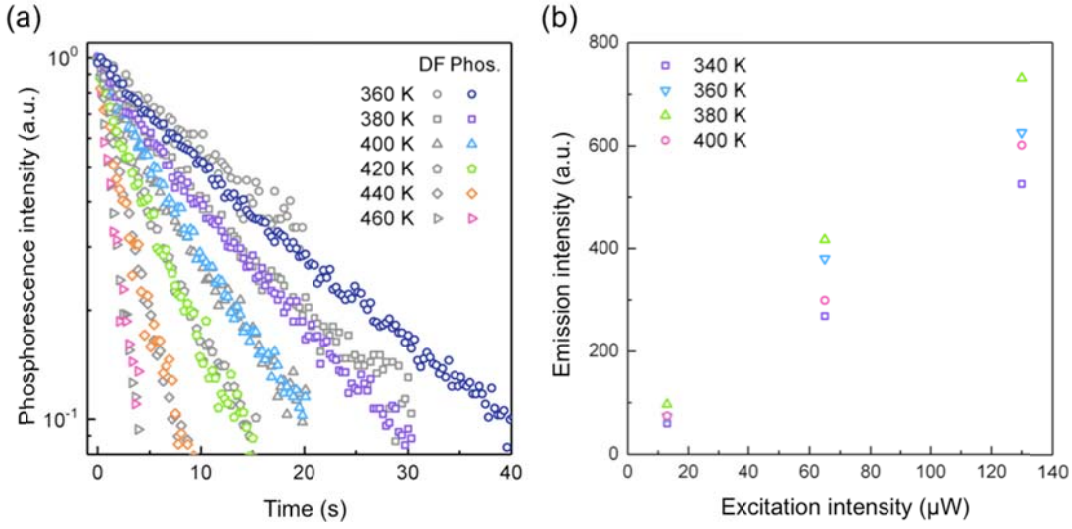

Figure 3-15. (a) Transient decay profiles of phosphorescence (colored symbols) and TADF (black symbols) of **coronene-d_{12}@ZIF-8** at temperatures above 360 K. (b) Dependence of the emission intensity of **coronene-d_{12}@ZIF-8** on excitation power intensity at 340 K (blue), 360 K (red), 380 K (green), and 400 K (orange).

3-5. Conclusion

I demonstrated that the nonradiative deactivation of a guest emitter can be dramatically reduced by encapsulation within a MOF, allowing long-lived phosphorescence (up to 22.4 s lifetime) to be observed even at temperatures as high as 460 K. This is accomplished without emitter aggregation and yields materials that are air-stable, two problems that inhibit the use of other host materials. Moreover, the small pore windows of ZIF-8 trap the emitting molecule, eliminating the possibility of thermal diffusion or leaching. Spectroscopy shows that coronene is completely isolated within the pores of the MOF and the rigidity of the MOF suppresses the molecular motion of the guest emitters. Finally, I also determined that the long-lived triplet excitons produced in **coronene@ZIF-8** allow TADF to be observed, an unexpected but important result that allows the colour of the long-lived emission to be controlled by increasing temperature. Because MOFs can be tailored with a wide variety of organic linkers and metal ions to optimize photophysical properties of guest emitter, this concept opens a promising new path to obtaining long-lived triplet excitons at high temperature.

References

[1] D. N. Congreve, J. Lee, N. J. Thompson, E. Hontz, S. R. Vost, P. D. Reusswig, M. E. Bahike, S. Reineke, T. Van Voorhis and M. A. Baldo, *Science*, 2013, **342**, 334–337.

[2] R. Kabe, N. Notsuka, K. Yoshida and C. Adachi, *Adv. Mater.*, 2016, **28**, 655–660.

[3] Z. An, C. Zheng, Y. Tao, R. Chen, H. Shi, T. Chen, Z. Wang, H. Li, R. Deng, X. Liu and W. Huang, *Nat. Mater.*, 2015, **14**, 685–690.

[4] S. Hirata, K. Totani, T. Yamashita, C. Adachi and M. Vacha, *Nat. Mater.*, 2014, **13**, 938–946.

[5] Q. le Masne de Chermont, C. Chaneac, J. Seguin, F. Pelle, S. Maitrejean, J.-P. Jolivet, D. Gourier, M. Bessodes and D. Scherman, *Proc. Natl. Acad. Sci.*, 2007, **104**, 9266–9271.

[6] M. Pope, H. P. Kallmann and P. Magnante, *J. Chem. Phys.*, 1963, **38**, 2042–2043.

[7] S. Scypinski and L. J. C. Love, *Anal. Chem.*, 1984, **56**, 322–327.

[8] J. L. Kropp, W. R. Dawson and R. Dawson, *J. Phys. Chem.*, 1987, **71**, 4499–4506.

[9] S. Reineke, N. Seidler, S. R. Yost, F. Prins, W. A. Tisdale and M. A. Baldo, *Appl. Phys. Lett.*, 2013, **103**, 93302.

[10] D. Lee, O. Bolton, B. C. Kim, J. H. Youk, S. Takayama and J. Kim, *J. Am. Chem. Soc.*, 2013, **135**, 6325–6329.

[11] S. Hirata, K. Totani, J. Zhang, T. Yamashita, H. Kaji, S. R. Marder, T. Watanabe and C. Adachi, *Adv. Funct. Mater.*, 2013, **23**, 3386–3397.

[12] R. E. Morris and P. S. Wheatley, *Angew. Chem. Int. Ed.*, 2008, **47**, 4966–4981.

[13] J.-R. Li, R. J. Kuppler and H.-C. Zhou, *Chem. Soc. Rev.*, 2009, **38**, 1477–1504.

[14] T. M. McDonald, J. A. Mason, X. Kong, E. D. Bloch, D. Gygi, A. Dani, V. Crocellà, F. Giordanino, S. O. Odoh, W. S. Drisdell, B. Vlaisavljevich, A. L. Dzubak, R. Poloni, S. K. Schnell, N. Planas, K. Lee, T. Pascal, L. F. Wan, D. Prendergast, J. B. Neaton, B. Smit, J. B. Kortright, L. Gagliardi, S. Bordiga, J. A. Reimer and J. R. Long, *Nature*, 2015, **519**, 303–308.

[15] G. Lu, S. Li, Z. Guo, O. K. Farha, B. G. Hauser, X. Qi, Y. Wang, X. Wang, S. Han, X. Liu, J. S. DuChene, H. Zhang, Q. Zhang, X. Chen, J. Ma, S. C. J. Loo, W. D. Wei, Y. Yang, J. T. Hupp and F. Huo, *Nat. Chem.*, 2012, **4**, 310–316.

[16] V. Agostoni, P. Horcajada, M. Noiray, M. Malanga, A. Aykaç, L. Jicsinszky, A. Vargas-Berenguel, N. Semiramoth, S. Daoud-Mahammed, V. Nicolas, C. Martineau, F. Taulelle, J. Vigneron, A. Etcheberry, C. Serre and R. Gref, *Sci. Rep.*, 2015, **5**, 7925.

[17] S. Wuttke, S. Braig, T. Preiß, A. Zimpel, J. Sicklinger, C. Bellomo, J. O. Rädler, A. M. Vollmar and T. Bein, *Chem. Commun.*, 2015, **51**, 15752–15755.

[18] F.-K. Shieh, S.-C. Wang, C.-I. Yen, C.-C. Wu, S. Dutta, L.-Y. Chou, J. V Morabito, P. Hu, M.-H. Hsu, K. C.-W. Wu and C.-K. Tsung, *J. Am. Chem. Soc.*, 2015, **137**, 4276–4279.

[19] D. Feng, T.-F. Liu, J. Su, M. Bosch, Z. Wei, W. Wan, D. Yuan, Y.-P. Chen, X. Wang, K. Wang, X. Lian, Z.-Y. Gu, J. Park, X. Zou and H.-C. Zhou, *Nat. Commun.*, 2015, **6**, 5979.

[20] N. Yanai, K. Kitayama, Y. Hijikata, H. Sato, R. Matsuda, Y. Kubota, M. Takata, M. Mizuno, T. Uemura and S. Kitagawa, *Nat. Mater.*, 2011, **10**, 787–793.

[21] Y. Inokuma, T. Arai and M. Fujita, *Nat. Chem.*, 2010, **2**, 780–783.

[22] Y. Inokuma, S. Yoshioka, J. Ariyoshi, T. Arai, Y. Hitora, K. Takada, S. Matsunaga, K. Rissanen and M. Fujita, *Nature*, 2013, **495**, 461–466.

[23] C. A. Bauer, T. V Timofeeva, T. B. Settersten, B. D. Patterson, V. H. Liu, B. A. Simmons and M. D. Allendorf, *J. Am. Chem. Soc.*, 2007, **129**, 7136–7144.

[24] Z. Wei, Z. Gu, R. K. Arvapally, Y. Chen, R. N. McDougald, J. F. Ivy, A. A. Yakovenko, D. Feng, M. A. Omary and H. Zhou, *J. Am. Chem. Soc.*, 2014, **136**, 8269–8276.

[25] J. Yu, Y. Cui, H. Xu, Y. Yang, Z. Wang, B. Chen and G. Qian, *Nat. Commun.*, 2013, **4**, 2719.

[26] S. Yuan, Y. K. Deng and D. Sun, *Chem. Eur. J.*, 2014, **20**, 10093–10098.

[27] D. Bose, J. Banerjee, S. H. Rahaman, G. Mostafa, H. K. Fun, R. D. Bailey Walsh, M. J. Zaworotko and B. K. Ghosh, *Polyhedron*, 2004, **23**, 2045–2053.

[28] Y. Takashima, V. M. Martínez, S. Furukawa, M. Kondo, S. Shimomura, H. Uehara, M. Nakahama, K. Sugimoto and S. Kitagawa, *Nat. Commun.*, 2011, **2**, 168.

[29] V. Martínez-martínez, S. Furukawa, Y. Takashima and I. L. Arbeloa, *J. Phys. Chem. C*, 2012, **116**, 26084–26090.

[30] Z. Xie, L. Ma, E. Kathryn, A. Jin and W. Lin, *J. Am. Chem. Soc.*, 2010, **132**, 922–923.

[31] Y. H. Zhao, Z. M. Su, Y. M. Fu, K. Z. Shao, P. Li, Y. Wang, X. R. Hao, D. X. Zhu and S. D. Liu, *Polyhedron*, 2008, **27**, 583–592.

[32] Y. Zhao, H. Xu, Y. Fu, K. Shao, S. Yang, Z.-M. Su, X.-R. Hao, D.-X. Zhu and E.-B. Wang, *Cryst. Growth Des.*, 2008, **8**, 3566–3576.

[33] C. Sun, X. Wang, X. Zhang, C. Qin, P. Li, Z. Su, D.-X. Zhu, G.-G. Shan, K.-Z. Shao, H. Wu and J. Li, *Nat. Commun.*, 2013, **4**, 2717.

[34] H. Uoyama, K. Goushi, K. Shizu, H. Nomura and C. Adachi, *Nature*, 2012, **492**, 234–238.

[35] K. S. Park, Z. Ni, A. P. Cote, J. Y. Choi, R. Huang, F. J. Uribe-Romo, H. K. Chae, M. O'Keeffe and O. M. Yaghi, *Proc. Natl. Acad. Sci.*, 2006, **103**, 10186–10191.

[36] N. Liédana, A. Galve, C. Rubio, C. Téllez and J. Coronas, *ACS Appl. Mater. Interfaces*, 2012, **4**, 5016–5021.

[37] J. Zhuang, C. H. Kuo, L. Y. Chou, D. Y. Liu, E. Weerapana and C. K. Tsung, *ACS Nano*, 2014, **8**, 2812–2819.

[38] M. H. Alkordi, Y. Liu, R. W. Larsen, J. F. Eubank and M. Eddaoudi, *J. Am. Chem. Soc.*, 2008, **130**, 12639–12641.

[39] V. Tabacik and S. Sportouch, *J. Raman Spectrosc.*, 1978, **7**, 61–66.

[40] Y. Yamauchi, M. Yoshizawa, M. Akita and M. Fujita, *J. Am. Chem. Soc.*, 2010, **132**, 960–966.

[41] Y. R. Zheng, W. J. Lan, M. Wang, T. R. Cook and P. J. Stang, *J. Am. Chem. Soc.*, 2011, **133**, 17045–17055.

[42] Y. Yang, J. S. Chen, J. Y. Liu, G. J. Zhao, L. Liu, K. L. Han, T. R. Cook and P. J. Stang, *J. Phys. Chem. Lett.*, 2015, **6**, 1942–1947.

[43] K. Ohno, T. Kajiwara and H. Inokuchi, *Bull. Chem. Soc. Jpn.*, 1972, **45**, 996–1004.

[44] M. C. McCarthy, V. Varela-Guerrero, G. V. Barnett and H. K. Jeong, *Langmuir*, 2010, **26**, 14636–14641.

[45] T. Itoh, *Chem. Rev.*, 2012, **112**, 4541–4568.

[46] T. Seko, K. Ogura, Y. Kawakami, H. Sugino, H. Toyotama and J. Tanaka, *Chem. Phys. Lett.*, 1998, **291**, 438–444.

[47] K. Horie and I. Mita, *Chem. Phys. Lett.*, 1982, **93**, 61–65.

[48] K. Horie, K. Morishita and I. Mita, *Macromolecules*, 1984, **17**, 1746–1750.

Chapter 4

Reversible control of triplet dynamics in metal-organic-framework-entrapped organic emitters via external gases

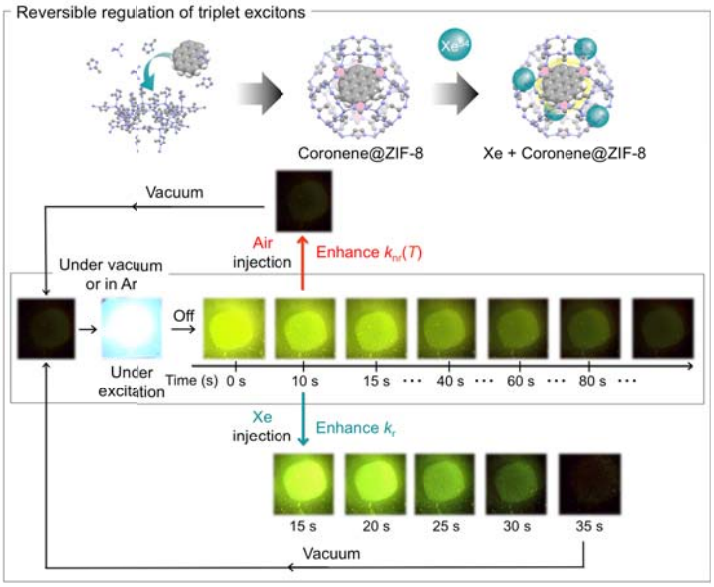

Hiroyuki Mieno, Ryota Kabe, and Chihaya Adachi

Submitted

4-1. Introduction

Triplet excitons of organic molecules used as phosphors[1,2] and photo-absorbers[3,4] play an important role in the physics of optoelectronic devices such as OLEDs[5–7] and photovoltaics.[8] Devising new ways to control triplet excitons will help advance the development of a wide variety of emitters,[7] photo reactions,[9,10] and organic semiconductor devices.[11–13] In a simple system undergoing photoluminescence, the key processes affecting triplet excitons are the generation process of ISC from a singlet excited state to a triplet excited state and the deactivation processes of radiative (phosphorescence) and non-radiative transition from a triplet excited state to the singlet ground state. The k_{isc} and k_p are strongly influenced by the chemical structure of the emitting molecules and can be tuned from 10^{-2} to 10^6 s^{-1} by exploiting spin-orbit coupling through the inclusion of heavy atoms like bromine,[14] iridium,[15–17] and platinum.[18,19] The $k_{nr}(T)$ is affected by factors related to the environment surrounding the emitters such as the host matrix,[20,21] emitter concentration,[22] and temperature (T) through processes such as energy transfer to other molecules[23] and thermal deactivation.[24] Minimization of $k_{nr}(T)$ by using rigid host matrices like steroids,[21] polymers,[25] clathrate compounds,[20,26] mixed crystals,[14] and MOFs[27–29] has been reported.

Because of the competing radiative and non-radiative recombination processes, precisely designed molecules and optimized molecular environments are required to obtain efficient RTP from organic molecules. RTP can easily be reduced by increasing temperature,[24] introducing triplet quenchers,[23] or enhancing molecular motion to increasing $k_{nr}(T)$. However, no effective way exists to enhance RTP by increasing k_p *via* simple external triggers. Although several approaches, such as the use of photochromic emitters[30] and pH-sensitive molecules[31] and the introduction of potassium iodine[32] or xenon (Xe)[33] to induce an external heavy-atom

effect, have been reported, these systems exhibit very slow responsivity and poor reversibility.

Here, I report a rapid and reversible enhancement of k_p in emitters encapsulated in MOFs by introducing heavy-atom gases as an external trigger (Fig. 1a). Recently, I demonstrated long-lived RTP with an observed τ_{phos} of 22 s under vacuum by embedding coronene-d_{12} into the zeolitic imidazolate framework ZIF-8.[27] The large surface area of ZIF-8 and low doping concentration of coronene-d_{12} in ZIF-8 allow for gas adsorption and desorption. In this study, I exposed **coronene-d_{12}@ZIF-8** to the gas argon (Ar) mixed with various concentrations of Xe, which has a large spin-orbit coupling constant, at room temperature, and investigated the dependence of the emission spectra, Φ_{phos}, and τ_{phos} on the concentration of Xe and the timing of the gas exposure. Both k_p and $k_{nr}(T)$ could be tuned by introducing Xe and air, allowing for the full control of long-lived triplet excitons.

4-2. Experimental

4-2-1. Film preparation of coronene-d_{12}@ZIF-8

A **coronene-d_{12}@ZIF-8** film was prepared by using ship-in-a-bottle synthesis following the procedure in Chapter 3.[27]

4-2-2. Measurement system

The long-lived photoluminescence spectra and decay profiles under various conditions were obtained using a measurement system with the configuration shown in Fig. 4-1. A **coronene-d_{12}@ZIF-8** film was first activated by the turbo molecular pump (HiPace80, Pfeiffer vacuum), then a gas mixture, the concentration of which was controlled by a gas mixer (Kofloc, PMG-1A), was introduced into the sample chamber. Notably, this system

contains several manual gas valves used for the introduction of the external gases. The **coronene-d_{12}@ZIF-8 film** was placed in a sample chamber with a quartz window and excited by a UV light source (MORITEX MUV-202U) with a bandpass filter (340 ± 5 nm). The emission spectra and emission decay profiles were recorded using a multichannel spectrometer (PMA-12, Hamamatsu Photonics) with a longpass filter (370 nm).

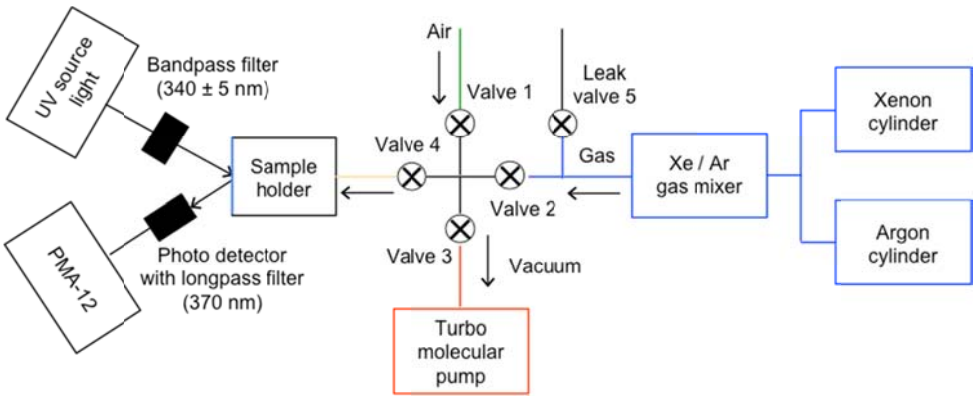

Figure 4-1. Schematic image of the measurement system

4-2-3. Methods

The Φ_{total} of **coronene-d_{12}@ZIF-8** in various environments were measured with an absolute photoluminescence quantum yield spectrometer (Quantaurus-QY, Hamamatsu Photonics) at room temperature under a vacuum (10^{-3} Pa).[27] Here, Φ_{flu} (photoluminescence quantum yield of the fluorescence) and Φ_{phos} were calculated from the emission intensity at all wavelengths obtained using the PMA-12. The PMA-12 was used to measure the emission integrated over 100-ms intervals. The total emission intensity (I_{total}) for 100-ms-long photo-excitation was measured by integrating all of the measurements from the PMA-12 with the first measurement starting at the same time as the photo-excitation. The fluorescence intensity (I_{flu}) was estimated by subtracting the intensity from the second 100-ms measurement interval, which roughly corresponds to the phosphorescence during the first

100-ms interval because of the slow phosphorescence decay, from the intensity during the first 100-ms measurement interval, which includes the photo-excitation period. The phosphorescence intensity (I_{phos}) was measured from the integrated intensity for all of the measurements from the second 100-ms measurement interval on with the intensity of the second 100-ms measurement interval counted twice to roughly account for the phosphorescence during excitation.

4-3. Results

The concentration of coronene-d_{12} in ZIF-8 is 1.03 wt%, which means that **coronene-d_{12}@ZIF-8** still has enough space to accommodate extra molecules.[27] The emission spectra under steady-state excitation and the emission decay profiles of the film were obtained in ambient air, Ar, and Xe and under vacuum at room temperature (Scheme. 4-1). Because phosphorescence is quenched by the oxygen in air,[23] only fluorescence was observed in air under steady-state excitation. On the other hand, dual steady-state emission from fluorescence and phosphorescence was observed under vacuum and in Ar and Xe (Fig. 4-2), and a slowly decaying phosphorescence was observed after stopping the excitation.

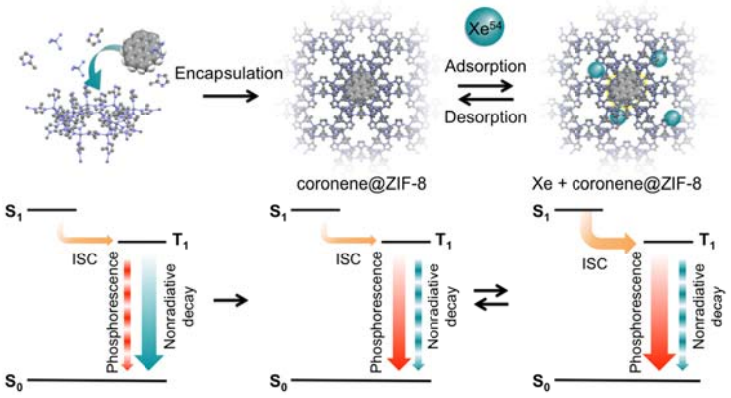

Scheme 4-1. Schematic image of **coronene-d_{12}@ZIF-8** adsorbing xenon.

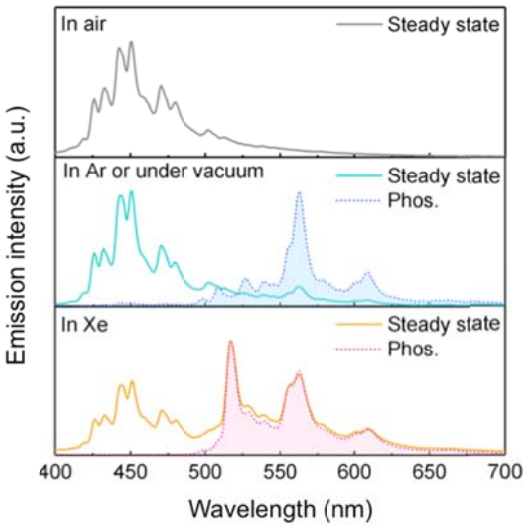

Figure 4-2. Steady-state photoluminescence spectra (solid lines) and delayed decay spectra (dashed lines), which correspond to phosphorescence, of **coronene-d_{12}@ZIF-8** in air (top), Ar or vacuum (middle), and Xe (bottom).

The large surface area originating from the porous structure of ZIF-8 leads to a good affinity for the gases,[34,35] so the external gas molecules can easily interact with the solid-state coronene-d_{12} in ZIF-8.[27] While air easily quenched the phosphorescence, the inert gas Ar does not affect the emission spectra or the observed τ_{phos}, which were nearly identical to those under vacuum (Fig. 4-3a). On the other hand, both the phosphorescence spectra and τ_{phos} were drastically different in Xe even though it is also an inert gas (Figs. 4-3a and 4-3b).

Because the ZIF-8 pores can adsorb Xe molecules,[36] this result can be attributed to an external heavy-atom effect induced by Xe. The yellow phosphorescence with peaks of 487, 509, 527, 539, 563, and 608 nm in Ar changes into green phosphorescence with peaks of 517, 525, 529, 563, 594, and 609 nm in Xe. Interestingly, the phosphorescence peak maximum under Xe is at 517 nm, which corresponds to the 0-0 transition of coronene-d_{12}.[32] Thus, the symmetry forbidden 0-0 transition of coronene-d_{12} becomes partially allowed because of spin-orbit coupling with Xe. A similar phenomenon was reported by combining coronene with

potassium iodide in ethanol[32] or with benzene in liquid Xe.[33] Moreover, the delayed fluorescence observed in Ar at 300 K disappeared in Xe because of the faster k_p.[27]

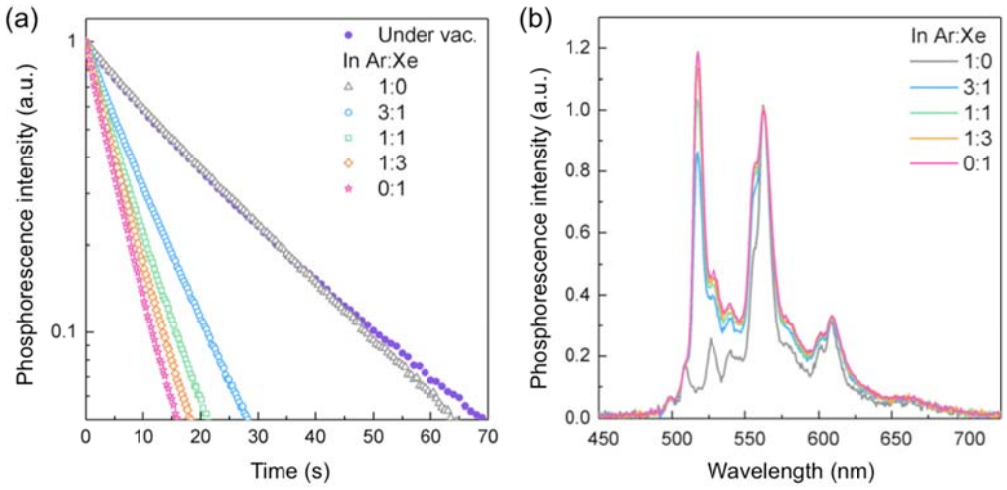

Figure 4-3. (a) Phosphorescence decay curves under vacuum and in various gas mixtures. (b) Phosphorescence spectra under vacuum and in various gas mixtures.

In addition to accelerating k_p, the heavy-atom effect also increases k_{isc}. Thus, the phosphorescence component in the steady-state emission increases compared to that in Ar, and the ratio of phosphorescence to the total emission (I_{phos}/I_{total}) for 100-ms-long photoexcitation (see the Methods for measurement details) increases from 0.26 in Ar to 0.70 in Xe (Table 4-1). The τ_{phos} of **coronene-d_{12}@ZIF-8** in Xe was 4.7 s, which is one-fifth of that in Ar (20.2 s). Although an acceleration of $k_{nr}(T)$ is often the origin of a reduction in τ_{phos}, the Φ_{phos} calculated from the total photoluminescence quantum yield (Φ_{total}) and I_{phos}/I_{total} was found to be 6.2%, which is much larger than that in Ar (3.7%) (Table 4-1 and Fig. 4-4). Therefore, the shorter τ_{phos} originates from an enhanced k_p.

Table 4-1. Photophysical properties of **coronene-d_{12}@ZIF-8** under various conditions.

Ar:Xe gas ratio	λ_{max} (nm)	I_{phos}/I_{total}	τ_{phos} (s)	Φ_{total} (%)	Φ_{flu} (%)	Φ_{phos} (%)
1:0	563	0.26	20.2	13.8	10.1	3.7
3:1	563	0.54	8.4	9.1	4.2	4.9
1:1	517	0.62	6.4	8.7	3.3	5.4
1:3	517	0.66	5.5	8.9	3.0	5.9
0:1	517	0.70	4.7	8.9	2.7	6.2

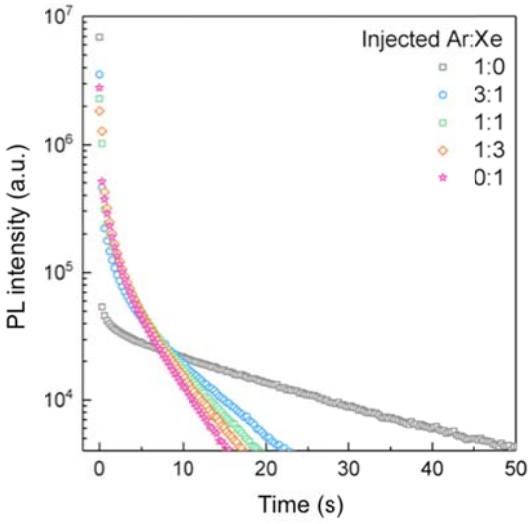

Figure 4-4. Photoluminescence decay curves under various mix gases after excitation for 100 ms.

Altering the concentration of Xe provides a simple method to control τ_{phos}. I measured the film in mixtures of Ar and Xe with Xe concentrations of 25%, 50%, and 75% (Figs. 4-3a and 4-3b). Phosphorescence intensity shows a linear relationship with the concentration of Xe (Fig. 4-5). Increasing the concentration of Xe increased Φ_{phos} because of the accelerated k_p, but Φ_{total} decreased since k_{isc} also accelerated, leading to a reduced fluorescence contribution (Table 4-1). These results clearly indicate that the strength of the external heavy-atom effect can be tuned with the concentration of the external gas. Even though the atomic size (4.4 Å) of Xe is slightly larger than the window size of ZIF-8 (3.4 Å), Xe atoms can pass through the

windows of ZIF-8 and interact with the coronene-d_{12} because the window size can be expanded by the rotation of the imidazole linkers.[36] Since there is no strong encapsulation effect between the Xe atoms and the pores of ZIF-8, Xe atoms can be removed by exposing the film to a different gas or placing the film under vacuum. Therefore, the effects of the external gases on **coronene-d_{12}@ZIF-8** are highly reversible.

To demonstrate this reversibility, the steady-state phosphorescence intensity of the **coronene-d_{12}@ZIF-8** film was observed over multiple cycles of sequential exposure to vacuum, Xe, and air (Fig. 4-6). Each environment had a distinct phosphorescence intensity that was nearly constant over the multiple cycles. Moreover, the phosphorescence intensity did not change even after I stored the film in air for several months. These results indicate that the modification of the triplet dynamics is fully reversible.

The response of the emission to the external gases is rapid and reversible, enabling the direct control of accumulated triplet excitons via the external heavy-atom effect. The emission of the film under vacuum exhibited a clear response within 1 s of introducing Xe after stopping the photo-excitation, and the response time was largely determined by the time it takes to manually open and close the gas valves of the measurement system and not the migration speed of the gas (Figs. 4-7 and 4-1). The response of the emission decay of **coronene-d_{12}@ZIF-8** film to the introduction of Xe after stopping the excitation along with the decay in Xe and under vacuum are shown in Figure 4-8.

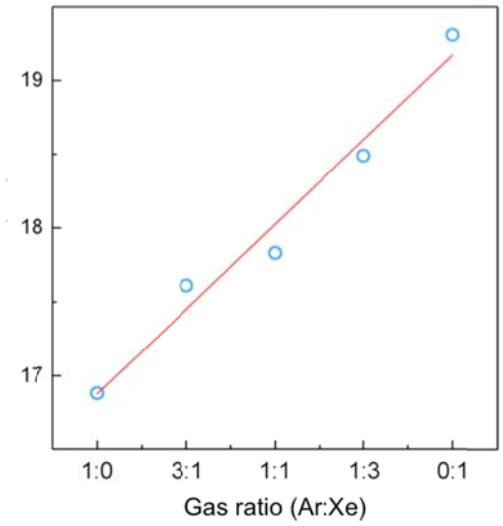

Figure 4-5. Integrated phosphorescence intensity under various concentrations Ar:Xe gas ratios.

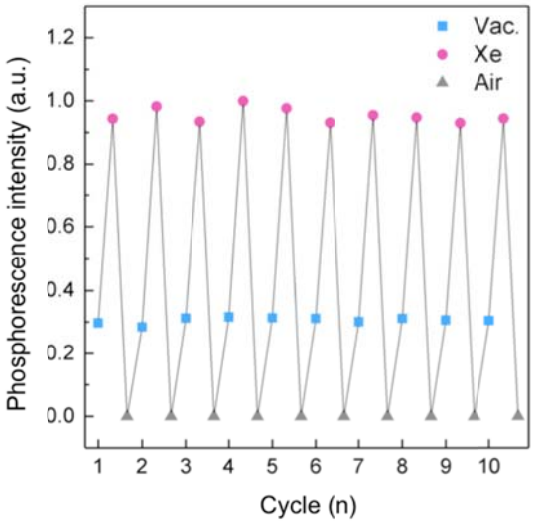

Figure 4-6. Steady-state phosphorescence intensity at 563 nm of **coronene-d_{12}@ZIF-8** exposed to multiple cycles of vacuum, Xe, and air.

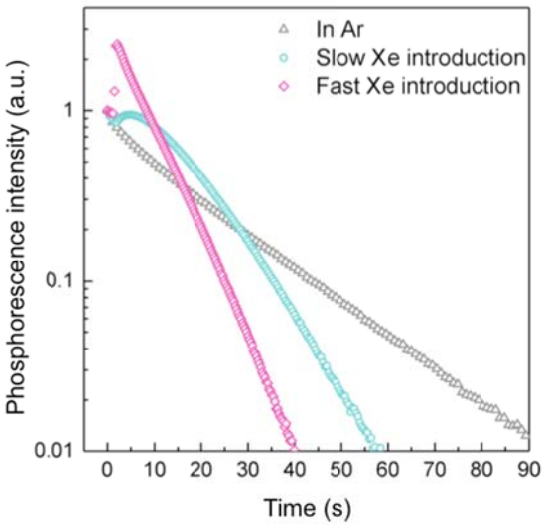

Figure 4-7. Phosphorescence decay curves under fast and slow regulation of gas valves. Measurements with Xe introduction were under vacuum before introducing the gas.

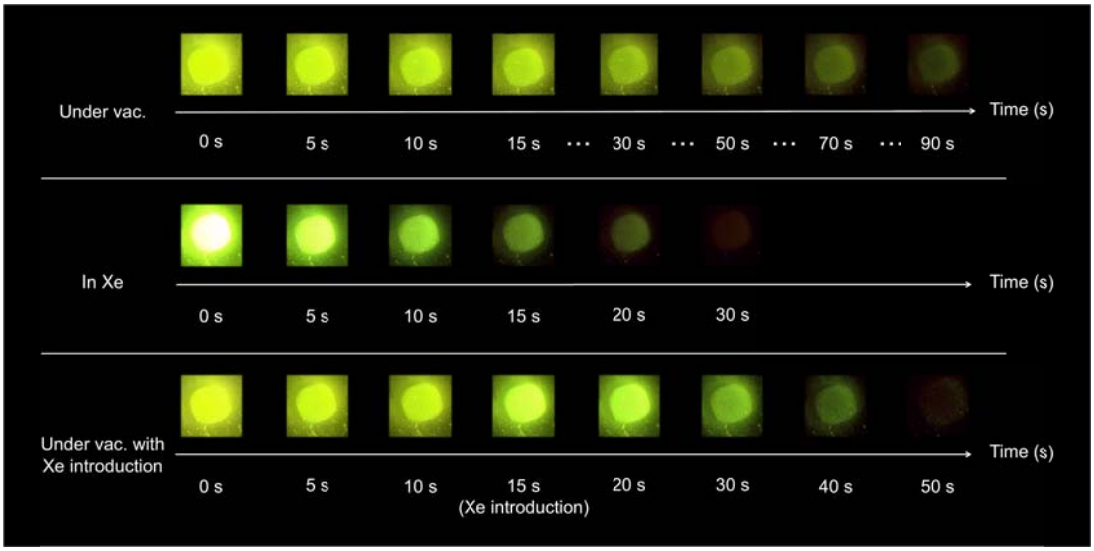

Figure 4-8. Photographs of time-dependent phosphorescence of **coronene-d_{12}@ZIF-8** (a) under vacuum, (b) in Xe, and (c) excited under vacuum followed by introduction of Xe 15 s after stopping excitation.

Long-lived phosphorescence from **coronene-d_{12}@ZIF-8** under vacuum is clearly visible more than one minute after stopping the excitation light (Fig. 4-8a). Because the Xe gas accelerates both k_{isc} and k_p, an initially more intense phosphorescence with a faster decay was observed in Xe (Fig. 4-8b). When I introduced Xe after stopping the excitation under vacuum, the phosphorescence intensity rapidly increased and the emission color became greener. (Figs. 4-8c, 4-9a, and 4-9b).

Introduction of Xe accelerates k_p, so the accumulated triplet excitons are more rapidly converted into phosphorescence, leading to a phosphorescence intensity that quickly increases before beginning to decay at a faster rate than under vacuum (Fig. 4-9b). Because introducing Xe increases k_p without affecting $k_{nr}(T)$, the integrated phosphorescence decay when exposed to Xe after being under vacuum was slightly larger than that in a constant Ar atmosphere (Fig. 4-10). By contrast, the long-lived phosphorescence was completely quenched when I introduced air (Fig. 4-9b). The enhanced emission intensity and shorter τ_{phos} indicate that I can regulate the phosphorescence by the introduction of Xe at arbitrary times (Figs. 4-9c and 4-11). The τ_{phos} can also be easily controlled by varying the concentration of Xe gas (Figs. 4-9d and 4-11). All of these results indicate that both the phosphorescence intensity and τ_{phos} can be easily and rapidly regulated through the introduction of a controlled amount of heavy atoms.

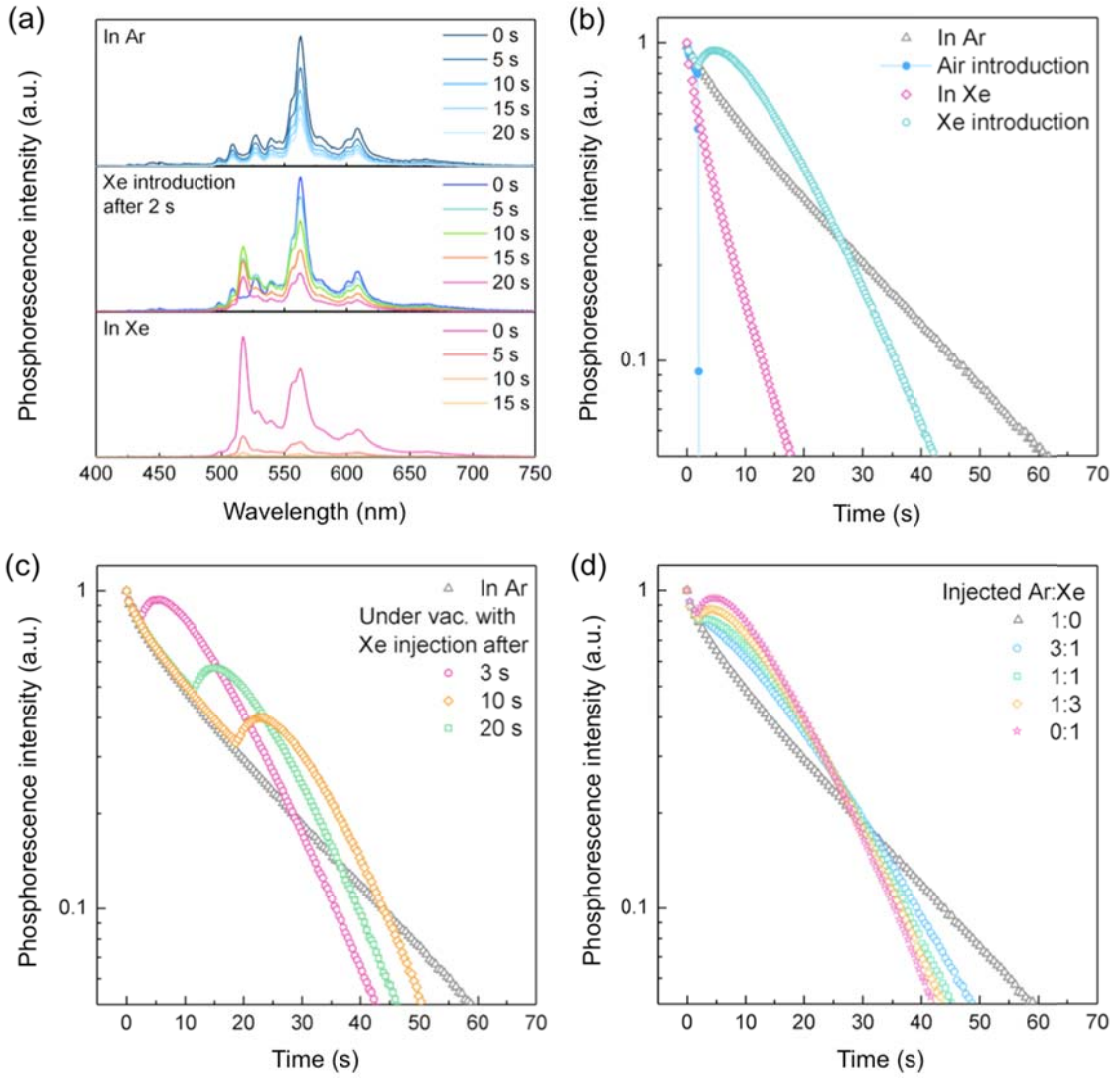

Figure 4-9. (a) Phosphorescence spectra for various times after stopping excitation (top) in Ar, (middle) under vacuum with Xe injection starting at 2 s, and (bottom) in Xe. (b) Phosphorescence decay profiles in Ar, under vacuum with air injection starting from 2 s, in Xe, and under vacuum with Xe injection starting from 2 s. (c) Phosphorescence decay curves in Ar without Xe introduction and with Xe introduction starting at 3, 10, and 20 s. (d) Phosphorescence decay curves under vacuum with the introduction of a various gas mixtures of Xe and Ar starting at 2 s.

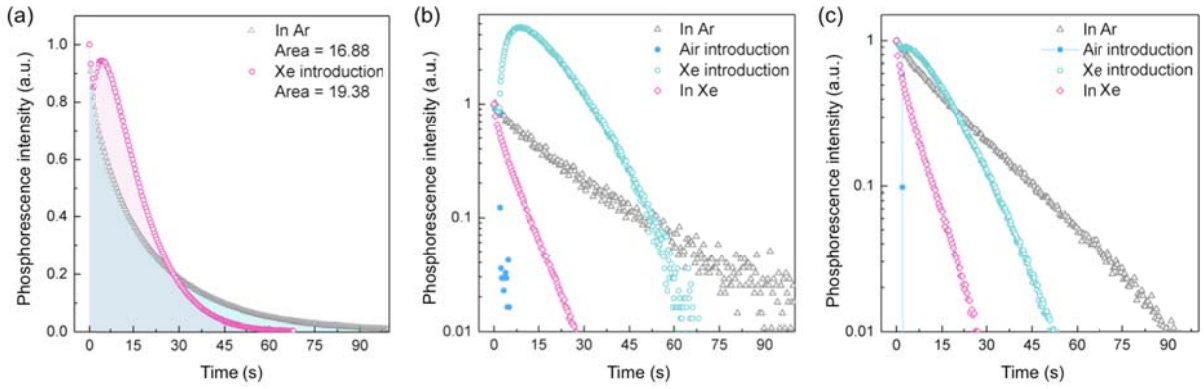

Figure 4-10. (a) Integrated phosphorescence intensity under Ar (gray triangles) and Xe (red circles). Time-dependent emission peak intensity at (b) 517 nm and (c) 563 nm under various conditions. Measurements with gas introduction were under vacuum before introducing the gas.

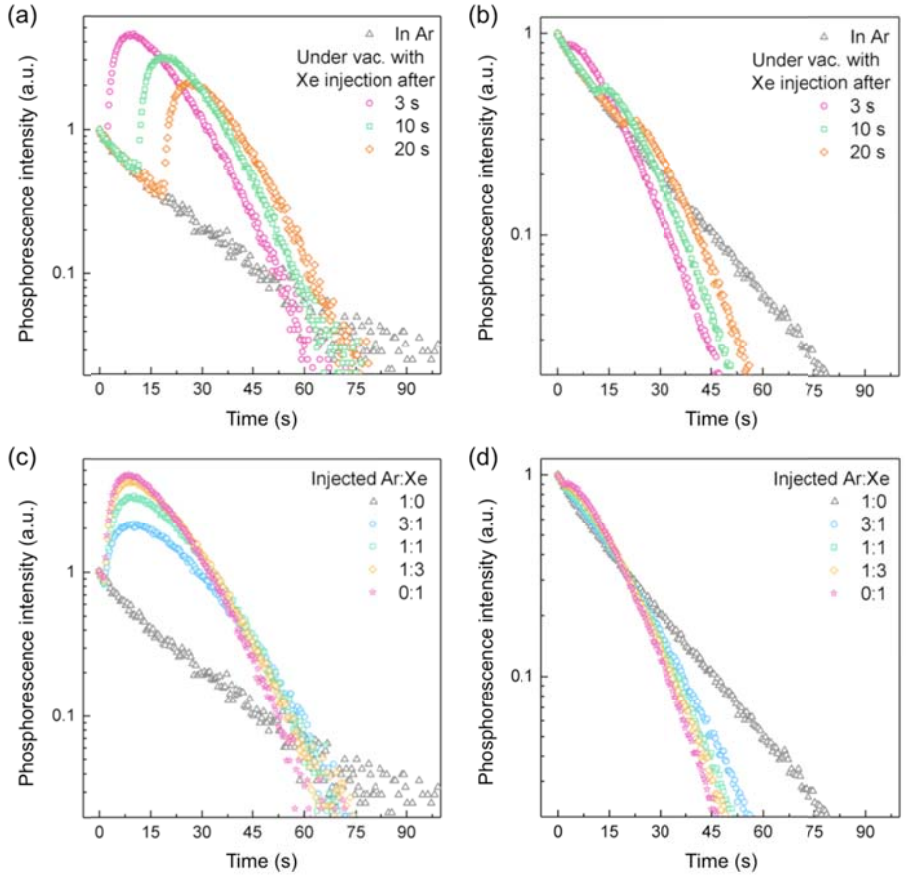

Figure 4-11. Time-dependent emission peak intensity at (a) 517 nm and (b) 563 nm in Ar without Xe injection and in Ar with Xe injection beginning after 5, 15, and 20 s after stopping the photo-excitation. Time-dependent emission peak intensity at (c) 517 nm and (d) 563 nm under vacuum with various mixtures of Xe and Ar injected 2 s after stopping the photo-excitation.

4-4. Conclusion

I demonstrated the use of the external heavy-atom effect to achieve fast, rapid, and reversible control of triplet excitons in organic semiconductors. A host matrix of ZIF-8 provides not only a rigid environment for the guest emitter but also a high affinity for external gases. According to the combination of these functions, I can easily regulate the conversion of the accumulated triplet excitons into emission. The timing and speed of extraction of accumulated excitons as emission can be controlled by introducing gas mixtures with various concentrations of Xe. Alternatively, the accumulated excitons can be completely extinguished through non-radiative processes by introducing air. This fast and reversible control of triplet excitons in a MOF matrix could open a new platform for fast-response photo-switches, reversible optical storage, and molecular computers.

References

[1] S. Hirata, *Adv. Opt. Mater.*, 2017, 1700116.

[2] S. Mukherjee and P. Thilagar, *Chem. Commun.*, 2015, **51**, 10988–11003.

[3] S. Hirata, K. Totani, T. Yamashita, C. Adachi and M. Vacha, *Nat. Mater.*, 2014, **13**, 938–946.

[4] W. Su, T. M. Cooper and M. C. Brant, *Chem. Mater.*, 1998, **4756**, 1212–1213.

[5] R. Kabe, N. Notsuka, K. Yoshida and C. Adachi, *Adv. Mater.*, 2016, **28**, 655–660.

[6] C. Adachi, M. a. Baldo, M. E. Thompson and S. R. Forrest, *J. Appl. Phys.*, 2001, **90**, 5048.

[7] H. Uoyama, K. Goushi, K. Shizu, H. Nomura and C. Adachi, *Nature*, 2012, **492**, 234–238.

[8] M. Righini, R. Quidant, S. R. Emory, J. A. Dionne, H. A. Atwater, Y. Kadoya, H. F. Hofmann, Q. Wang, F. Capasso, V. M. Shalaev, A. Polman, A. Archambault, T. V Teperik, F. Marquier, J. J. Greffet and P. Yeh, *Science*, 2013, **340**, 334–338.

[9] C. Leveque, L. Chenneberg, V. Corce, C. Ollivier and L. Fensterbank, *Chem. Commun.*, 2016, **52**, 9877–9880.

[10] K. Horie, H. Ando and I. Mita, *Macromolecules*, 1987, **20**, 54–58.

[11] S. Hoshino and H. Suzuki, *Appl. Phys. Lett.*, 1996, **69**, 224–226.

[12] H. Nakanotani, T. Higuchi, T. Furukawa, K. Masui, K. Morimoto, M. Numata, H. Tanaka, Y. Sagara, T. Yasuda and C. Adachi, *Nat. Commun.*, 2014, **5**, 4016.

[13] J. Kido and Y. Iizumi, *Appl. Phys. Lett.*, 1998, **73**, 2721–2723.

[14] O. Bolton, K. Lee, H.-J. Kim, K. Y. Lin and J. Kim, *Nat. Chem.*, 2011, **3**, 205–210.

[15] Y. You and S. Y. Park, *Dalt. Trans.*, 2009, **9226**, 1267–1282.

[16] Z. Xie, L. Ma, E. Kathryn, A. Jin and W. Lin, *J. Am. Chem. Soc.*, 2010, **132**, 922–923.

[17] L. Li, S. Zhang, Y. Xu, S. Zhao, Z. Sun and J. Luo, *Inorg. Chem.*, 2015, **54**, 8872–8874.

[18] K. Li, G. S. Ming Tong, Q. Wan, G. Cheng, W.-Y. Tong, W.-H. Ang, W.-L. Kwong and C.-M. Che, *Chem. Sci.*, 2016, **7**, 1653–1673.

[19] B. G. Zhou, W. Wong, S. Poon, C. Ye and Z. Lin, *Adv. Funct. Mater.*, 2009, **19**, 531–544.

[20] S. Scypinski and L. J. C. Love, *Anal. Chem.*, 1984, **56**, 322–327.

[21] S. Hirata, K. Totani, J. Zhang, T. Yamashita, H. Kaji, S. R. Marder, T. Watanabe and C. Adachi, 2013, **23**, 3386–3397.

[22] Y. Kawamura, J. Brooks, J. J. Brown, H. Sasabe and C. Adachi, *Phys. Rev. Lett.*, 2006, **96**, 017404.

[23] C. Grewer and H.-D. Brauer, *J. Phys. Chem.*, 1994, **98**, 4230–4235.

[24] S. Hirata, K. Totani, H. Kaji, M. Vacha, T. Watanabe and C. Adachi, 2013, **1**, 438–442.

[25] S. Reineke, N. Seidler, S. R. Yost, F. Prins, W. A. Tisdale and M. A. Baldo, *Appl. Phys. Lett.*, 2013, **103**, 93302.

[26] P. Montes-Navajas and H. Garcia, *J. Phys. Chem. C*, 2010, **114**, 2034–2038.

[27] H. Mieno, R. Kabe, N. Notsuka, M. D. Allendorf and C. Adachi, *Adv. Opt. Mater.*, 2016, **4**, 1015–1021.

[28] X. Yang and D. Yan, *Chem. Sci.*, 2016, **7**, 4519–4526.

[29] X. Yang and D. Yan, *Adv. Opt. Mater.*, 2016, **4**, 897–905.

[30] Y. Katsurada, S. Hirata, K. Totani, T. Watanabe and M. Vacha, 2015, **3**, 1726–1737.

[31] Y. Yang, K. Z. Wang and D. Yan, *ACS Appl. Mater. Interfaces*, 2016, **8**, 15489–15496.

[32] J. Najbar, J. Rodakiewicz-nowak and A. Chodkowska, *J. Lumin.*, 1978, **17**, 449–465.

[33] Y. Hsu and P. M. Johnson, *J. Chem. Phys.*, 1973, **59**, 136–142.

[34] M. C. McCarthy, V. Varela-Guerrero, G. V Barnett and H.-K. Jeong, *Langmuir*, 2010, **26**, 14636–14641.

[35] J. Q. Jiang, C. X. Yang and X. P. Yan, *ACS Appl. Mater. Interfaces*, 2013, **5**, 9837–9842.

[36] D. H. Gallaba, A. G. Albesa and A. D. Migone, *J. Phys. Chem. C*, 2016, **120**, 16649–16657.

Chapter 5

Summary of this thesis

5-1. Summary of this thesis

In this thesis, suppression of nonradiative decay processes from T_1 or S_1 was investigated through both a general strategy of introducing emitter molecules into MOFs as organic linkers and a novel way of encapsulating guest emitters within the cavities of MOFs to realize high PLQY and long-lived triplet excitons.

In Chapter 2, a MOF showing TADF characteristics was firstly demonstrated by designing a new organic linker that consists of both electron-donating and -accepting moiety. The MOF under vacuum exhibits relatively lower PLQY and broad and red-shifted emission than the linker itself in solution. This is caused by the interaction between organic linkers each other and organic linkers and metal clusters, indicating that an introducing strategy as organic linkers is ineffective to suppress nonradiative decay process of emitters.

In Chapter 3, we proposed a novel concept of embedding emitters in the isolated cavities of MOFs to suppress self-quenching, nonradiative decay process, and molecular diffusion. The emitters trapped in MOFs have longest triplet exciton lifetime of 22.4 s at room temperature. Phosphorescence can be realized even at high temperatures up to 460 K because of thermal stability MOFs intrinsically have. Moreover, even though emitters have a large energy gap between S_1 and T_1 (0.42 eV), such long triplet exciton allowed us to achieve TADF.

In Chapter 4, a host matrix of ZIF-8 provides not only a rigid environment for the guest emitter but also a high affinity for external gases. The accumulated triplet excitons by excitation light were rapidly extracted as emission by introducing heavy atom Xe. A new strategy to efficiently control triplet exciton dynamics was achieved by adsorbing external gases in MOFs encapsulating organic emitters in their cavities.

5-2. Future perspective

When designing new luminescent MOFs, many type of charge-transfer interactions such as metal-to-linker, linker-to-metal, excimer formation, and aggregation of organic linkers need to be considered. According to the result in Chapter 2, a MOF having TADF-emitting organic linkers exhibited the red-shifted of emission than that of organic linker itself because the adjacent organic linker is closed distance less than 1 nm in the framework. This crowd condition of the linker-based luminescent MOF is not favorable for the conventional emitters. In contrast, this highly condensed condition could help to develop AIE and photon up-conversion based on TTA because the close packing of organic linkers reduces nonradiative decay processes and increases the collision frequency of triplet excitons.

To develop highly efficient TADF-MOFs, I propose two strategies based on the guest-related luminescent MOFs (Figure 5-1). One is an encapsulation of existing TADF organic compounds within the cavity of MOFs. In this strategy, while it is required that MOFs have large enough pores and windows to encapsulate TADF compounds, concentration quenching and nonradiative decay of triplet excitons can be suppressed as demonstrated in Chapter 3. The other strategy is exciplex emission between an encapsulated donor (or acceptor) and a linker molecule having acceptor (or donor) property (Figure 5-2). In this strategy, large cavities or windows of MOF are not required because size of electron-donating or -accepting moieties is smaller than conventional TADF compounds. This advantage makes it easy to tune photophysical properties by altering guest aromatic compounds but most of organic linkers have low T_1 level, causing the deactivation of triplet excitons through energy transfer from the triplets of the exciplex to the triplets of organic linkers. So that, selection or design of organic linkers that have high T_1 level is required. Furthermore, if it is desirable to

prevent external molecules including oxygen and solvents from adsorbing into MOFs, post-synthetic surface modification can be a versatile methodology for introducing functionality into MOFs. Post-synthetic surface modification is well known as a chemical functionalization on the surface of previously synthesized MOFs.[1] Therefore, if using polymers that barrier oxygen as a surface modification reagent, quenching of triplet excitons by oxygen can be suppressed.

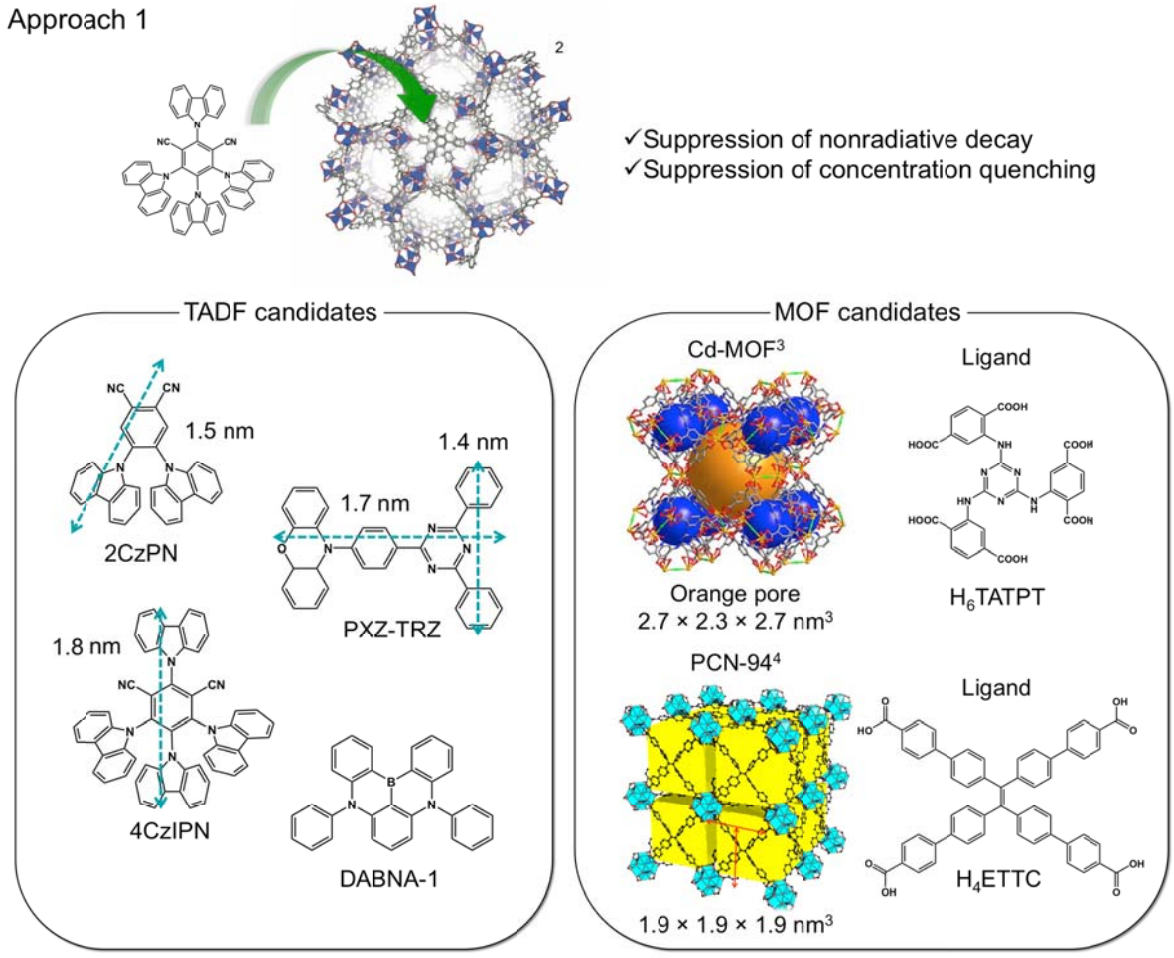

Figure 5-1. Approach 1 to obtain TADF with high PLQY.

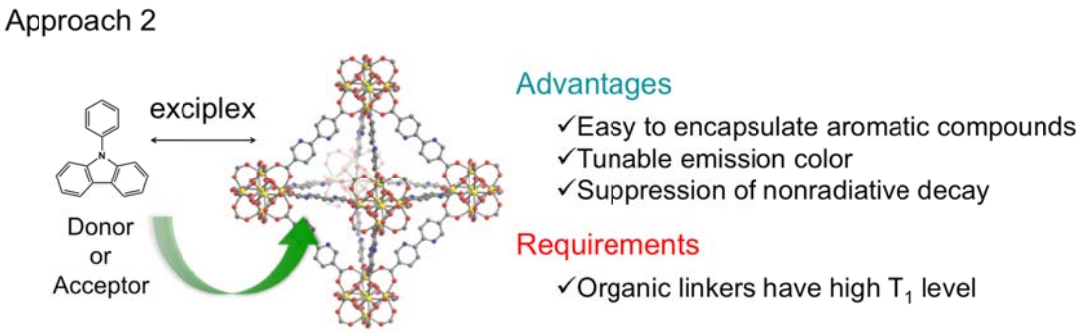

Figure 5-2. Approach 2 to obtain TADF with high PLQY.

Compounds showing TADF have been adapted to bioimaging and photocatalyst to date. Long-lived luminescence that originates from TADF can be used in time-resolved fluorescence imaging for eliminating the background fluorescence. A MOF exhibiting TADF is also promising because MOFs have high thermal and chemical stability, and large surface area that can contribute to higher sensitivity for oxygen. Since the contribution of TADF emission was small in Chapter 2, a new TADF-MOF having small ΔE_{ST} less than 0.2 eV needs to be developed. To increase cellular uptake, particle size of MOFs (less than 100 nm) should be controlled by changing reaction conditions such as temperature, additive, reaction time, metal source, and reaction solvent.

Harvesting triplet excitons is also quite important for EL devices because recombination of injected electrons and holes generates excitons in a ratio of 25% singlets to 75% triplets as mentioned in Chapter 1. Although MOF is a suitable host matrix for photoluminescence, EL from MOF is still challenging. Only two reports present to date. One is the first report demonstrated by the encapsulation of quantum dots within the cavities of MOF-5. However, no electroluminescence spectrum and external quantum efficiency were provided. The other report is white light emission from an intrinsic MOF by electrical excitation. The external quantum efficiency of 1.2 % was achieved.

EL from MOFs is expected to be highly durable light-emitting electrochemical cells (LECs) and also chemical sensors as a future application because MOFs have cavities to encapsulate analyte. One of the practical ideas is that emitters are encapsulated within the cavities of MOFs that have shallower LUMO and deeper HOMO level compared with those of guest emitters in order to directly inject hole and electron into guest emitters. For example, Zn-MOF-74, which consists of Zn ions and 2,5-dihydroxyterephthalic acid as organic linkers, is an ideal candidate because it has shallow LUMO (-2.7 eV) and deep HOMO (-5.9 eV) with high chemical and thermal stability according to the calculation results (Figure 5-3). Moreover, Zn-MOF-74 accommodates both emitters and ionic liquids because of the large 1D channels (1.4 × 1.4 nm) if using coumarin 545T (HOMO: -5.3 eV, LUMO: -2.9 eV) as emitters and 1-alkyl-3-methylimidazoliumhexafluorophosphate as ionic liquids. Since it is considered that ionic liquids can move freely in the 1D channels when applying voltage, electric double layer should be formed, leading to the injection of hole and electron into encapsulated emitters.

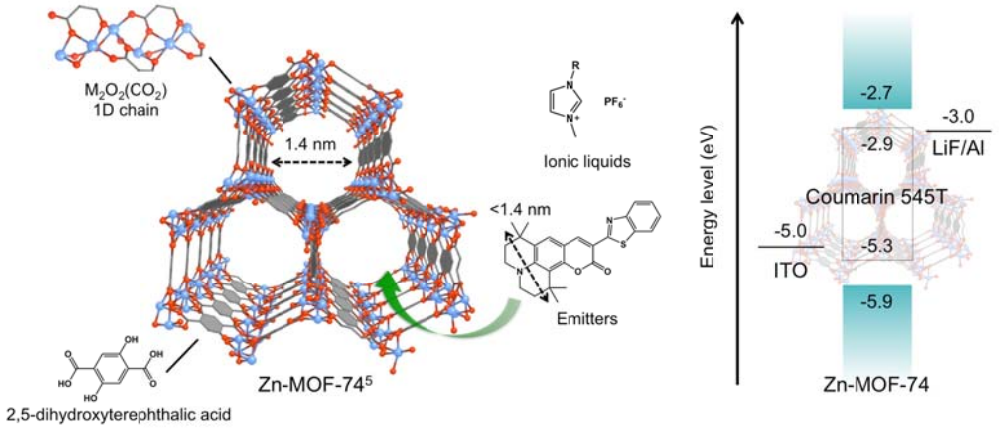

Figure 5-3. A method for EL from MOFs with high efficiency.

In Chapters 3 and 4, nonradiative decay of encapsulated emitters is dramatically suppressed by using MOFs as a host matrix. Because the resulting ultralong phosphorescence

can be detected by low cost CCDs, this approach would be suitable for imaging applications. In addition, since MOFs still have enough space to accommodate extra molecules such as gases and solvents, transition processes related to triplet excitons including TADF, phosphorescence, and nonradiative decay can be controlled by external stimuli. Based on this unique feature, optical applications can be developed such as photo-switches and optical storage because the on/off ratio of phosphorescence is quite high and response time is fast less than 0.1 s. The temperature dependence of triplet exciton dynamics and the recognition of extra adsorbents can give us the opportunity to detect temperature and analytes simultaneously by observing changes of phosphorescence intensity, spectrum, and lifetime. As of now, analytes that allows detection in the host-guest system are limited to oxygen, Xe, and halogen compounds. To spread a variety of analytes, encapsulation of multiple emitters into MOFs and functionalization of analyte-responsible group into organic linkers or encapsulated emitters are required. Because ZIF-8 used in Chapters 3 and 4 has quite small windows (0.34 nm) for analytes to go through, the strategy of using MOFs have larger windows and cavities is more desirable for multiple sensors.

References

[1] C. V. McGuire and R. S. Forgan, *Chem. Commun.*, 2015, **51**, 5199–5217.

[2] D. Saha and S. Deng, *Tsinghua Sci. Technol.*, 2010, **15**, 363–376.

[3] C. Sun, X. Wang, X. Zhang, C. Qin, P. Li, Z. Su, D.-X. Zhu, G.-G. Shan, K.-Z. Shao, H. Wu and J. Li, *Nat. Commun.*, 2013, **4**, 2717.

[4] Z. Wei, Z. Gu, R. K. Arvapally, Y. Chen, R. N. McDougald, J. F. Ivy, A. A. Yakovenko, D. Feng, M. A. Omary and H. Zhou, *J. Am. Chem. Soc.*, 2014, **136**, 8269–8276.

[5] D. Britt, H. Furukawa, B. Wang, T. G. Glover and O. M. Yaghi, *Proc. Natl. Acad. Sci.*, 2009, **106**, 20637–20640.

Abbreviation list

Keywords

Aggregation-induced emission (**AIE**)

Brunauer-Emmett-Teller (**BET**)

Charge-coupled devices (**CCDs**)

Commission International de I'Eclairage (**CIE**)

Dimethylformamide (**DMF**)

Electroluminescence (**EL**)

Energy gap between the lowest singlet excited state and the lowest triplet excited state (ΔE_{ST})

Fourier transform infrared spectrometer (**FT-IR**)

Highest occupied molecular orbital (**HOMO**)

Intersystem crossing (**ISC**)

Ligand-to-metal charge transfer (**LMCT**)

Lowest singlet excited state (S_1)

Lowest triplet excited state (T_1)

Lowest unoccupied molecular orbital (**LUMO**)

Metal-organic frameworks (**MOFs**)

Metal-to-ligand charge transfer (**MLCT**)

Organic light-emitting diodes (**OLEDs**)

Porous coordination polymers (**PCPs**)

Reverse intersystem crossing (**RISC**)

Room temperature phosphorescence (RTP)

Secondary building units (**SBUs**)

Singlet excited state (S_0)

Thermally activated delayed fluorescence (**TADF**)

Thermo gravimetric analysis (**TGA**)

Time-dependent density functional theory (**TD-DFT**)

Triplet excited state (T_0)

Triplet-triplet annihilation (**TTA**)

Up-conversion (**UC**)

X-ray diffraction (**XRD**)

Materials

Adeninate (**Ad**)

3-aminopropyltrimethoxysilane (**3-APTMS**)

1,3-benzenedicarboxylic acid (***m*-BDC**)

1,4-benzenedicarboxylic acid (**BDC**)

Benzimidazole (**BIM**)

4,4'-bipyridyl (**Bipy**)

4,4'-biphenyldicarboxylic acid (**Bpdc**)

Acetonitrile (**CH_3CN**)

o-dichlorobenzene (**DCB**)

4-[*p*-(dimethylamino)styryl]-1-methylpyridinium (**DMASM**)

4-(4-(diphenylamino)styryl)-1-dodecyl-pyridinium bromide (**DPASD**)

4′,4‴,4‴ ″,4‴ ‴ ″-(ethene-1,1,2,2-tetrayl)tetrakis(([1,1′-biphenyl] -3-carboxylic acid)) (**H_4ETTC**)

1,1′-ethynebenzene-3,3′,5,5′-tert-racarboxylic acid (**H_2EBTC**)

4,4"-Dicarboxyl-2'-diphenylamino-[1,1':4',1"]terphenyl (**H_2tpdc-dpa**)□

Tris(2-phenylpyridinato)iridium(III) (**$Ir(ppy)_3$**)

Bis(2-phenylpyridinato-)(2,2'-bipyridine)iridium(III) ion (**$Ir(ppy)_2(bpy)^+$**)

Dimethylamine (**Me_2NH_2**)

2,6'-naphthalenedicarboxylic acid (**NDC**)

Polymethylmethacrylate (**PMMA**)

Tri(4-imidazolylphenyl)amine (**TIPA**)

Physical symbols

External quantum efficiency (η_{EQE})

Fluorescence intensity (I_{flu})

Fluorescence lifetime (τ_{flu})

Fluorescence quantum yield (Φ_{flu})

Internal quantum efficiency (η_{IQE})

Maximum peak of fluorescence (λ_{max})

Phosphorescence intensity (I_{phos})

Phosphorescence lifetime (τ_{phos})

Phosphorescence quantum yield (Φ_{phos})

Photoluminescence lifetime of prompt component ($\tau_{delayed}$)

Photoluminescence lifetime of prompt component ($\boldsymbol{\tau_{prompt}}$)

Photoluminescence quantum yield ($\boldsymbol{\Phi_{PL}}$)

Photoluminescence quantum yield in air ($\boldsymbol{\Phi_{air}}$)

Photoluminescence quantum yield in inert gas ($\boldsymbol{\Phi_{inert}}$)

Photoluminescence quantum yield of delayed component ($\boldsymbol{\Phi_{delay}}$)

Photoluminescence quantum yield of TADF ($\boldsymbol{\Phi_{TADF}}$)

Rate constant of ISC from singlets to triplets ($\boldsymbol{k_{isc}}$)

Rate constant of nonradiative decay from T_1 to S_0 ($\boldsymbol{k_{nr}(T)}$)

Rate constant of radiative decay from T_1 to S_0 ($\boldsymbol{k_p}$)

Total emission intensity ($\boldsymbol{I_{total}}$)

Acknowledgements

The studies in this thesis were carried out at Adachi laboratory, Department of Chemistry and Biochemistry, Graduate School of Kyushu University from 2013-2018.

I am deeply grateful to Professor Chihaya Adachi for supervising this thesis, excellent experimental environment, helpful discussion, and exact comments and advice for all of my works. I am also deeply grateful to Professor Sunao Yamada and Professor Hiroyuki Furuta for co-supervising of this thesis. I would also like to thank Associate Professor Hajime Nakanotani, Assistant Professor Ryota Kabe, and Dr. William Potscavage. They also gave me useful advice and helped in preparing of this thesis and my papers. Especially, Assistant Professor Ryota Kabe helped in preparing this thesis and my papers, in many discussions, and in experiments. I also would like to acknowledge Dr. Mark D. Allendorf for helping my research, especially in Chapter 3, during my stay in Sandia National Laboratories in Livermore in U.S.A. from May 2015 to March 2016. Prof. Takuma Yasuda, Associate Prof. Toshinori Matsushima, Associate Prof. Youichi Tsuchiya, Assistant Prof. Kenichi Goushi, Assistant Prof. Takeshi Komino, Assistant Prof. Masashi Mamada, Dr. Toshihiro Oda, Dr. Shuho Tanimoto, Dr. Takehiro Takahashi, Dr. Masaya Hirade, Dr. Jun Yun Kim, Dr. Sae Youn Lee, Dr. Yu Seok Yang, Dr. Munetomo Inoue, Dr. Kou Yoshida, Dr. Hwang Sun Bin, Mr. Kou Inada, Mr. Naoyuki Takada, Mr. Takuro Nishimoto, Mr. Yutaka Hisamune, Mr. Kentaro Yamamoto, Ms. Keiko Kusuhara, Ms. Nozomi Nakamura, Ms. Mayumi Kudo, Ms. Sachiko Higashikawa, Ms. Rei Sasagawa, Ms. Hiromi Aizaki, Ms. Nao Onishi, Ms. Hiroko Kuratomi, Ms. Mihoko Matsuo, Ms. Makiko Kogo, Ms. Keiko Ohara, and Ms. Chihiro Nakanotani also helped me in experiments and daily life. During Kyushu University Program for Leading Graduate Schools on Molecular Systems for Devices, Associate Prof. Daisuke Kawaguchi,

Associate Prof. Kentaro Ishizuka, Assistant Prof. Joseph Hui, Assistant Prof. Pangpang Wang, Assistant Prof. Takeshi Komino, Assistant Prof. Yuta Tsuji, Mr. Masayuki Kurokawa, Mr, Shigeyuki Naito, Ms. Sayoko Otomo, Ms. Makiko Ishida, Ms. Mika Ura, Ms. Eri Ando, Ms. Ai Matsunobu, Ms. Fumi Takahashi, Ms. Satoko Serizawa, Ms. Tomoko Noda, Ms. Tomoko Takebe, Ms. Tomomi Takada, and Ms. Yukie Tahata helped me in discussions and daily life. I also acknowledge all the members of Adachi laboratory and Leading program and all persons who I met through my works for their supports not only for my work but also my daily life. I would like to thank the Japan Society for the Promotion of Science for a grant and a fellowship that made it possible to complete this study. Finally, I would also like to express my gratitude to my families for their moral support and warm encouragements.

January, 2017 *Hiroyuki Mieno*